Title
Non-local fractional diffusion and transport in magnetized plasmas

Permalink
https://escholarship.org/uc/item/7c04b8kd

Author
Kullberg, Adam Bryce

Publication Date
2014

Peer reviewed|Thesis/dissertation

University of California
Los Angeles

Non-local fractional diffusion and transport in magnetized plasmas

A dissertation submitted in partial satisfaction
of the requirements for the degree
Doctor of Philosophy in Physics

by

Adam Bryce Kullberg

2014

ABSTRACT OF THE DISSERTATION

Non-local fractional diffusion and transport in magnetized plasmas

by

Adam Bryce Kullberg

Doctor of Philosophy in Physics

University of California, Los Angeles, 2014

Professor George Morales, Chair

This thesis addresses several limitations in the current state of the art fractional models, and applies fractional transport concepts to transport in confined plasmas. One limitation that is addressed is the discrepancy between the strict mathematical properties of the Lévy distributions that underlie fractional diffusion models and the distributions observed in experiment and numerical simulation. Specifically, the second and higher moments of the Lévy distribution are infinite, while the moments of observed distributions are finite. This issue is dealt with using tempered, or truncated Lévy statistics in which the moments of the Lévy distributions are regularized by including exponential damping, with damping constant λ, into the tails of the distribution. In this thesis these tempered Lévy processes are studied in the context of a spatially tempered fractional Fokker-Planck (TFFP) equation and in the context of fluctuation driven transport.

Other limitations that this thesis addresses are related to the dimensionality of the fractional derivatives commonly used to model transport, and the application of fractional derivatives to transport in bounded finite-sized domains. Many fractional models of radial transport in a cylindrical system are based on one-dimensional Cartesian fractional operators. In this thesis a fully two-dimensional fractional Laplacian operator is developed from a generalized random walk model.

This 2D operator can be azimuthally averaged to produce a radial fractional operator that correctly incorporates, near the origin, all the geometric effects of a 2D circular system. There are also subtleties in applying fractional derivative operators, which are often formulated on an unbounded domain, to a finite domain. In this this thesis a bounded domain model of radial fractional transport is formed using mask functions that modify the kernels of the fractional operators and that go to zero in a boundary layer to remove mathematical singularities associated with limiting the range of integration.

This thesis also presents an analytic solution to the one-dimensional fractional thermal wave equation for the unbounded domain. To the author's knowledge, no such thermal wave solution is present in the literature.

Finally this thesis also compares the results from the radial fractional model to experimental results taken from several different tokamak fusion devices. The devices considered include the General Atomic's machine DIII-D and the major European devices: the Joint European Torus (JET), the Axially Symmetric Divertor Experiment (ASDEX-Upgrade), and the Rijnhuizen Tokamak Project (RTP). The survey focuses on two types of experiment: steady off-axis ECH experiments from RTP and power modulation experiments from JET, ASDEX-Upgrade, and DIII-D. In the steady heating experiments from RTP, hollow temperature profiles, or profiles that peak away from the center, are observed. Hollow profiles are an intrinsic feature of the radial fractional model, and it is found that the radial model is robust in describing the observed RTP profiles. In the power modulation experiments, the fractional model only achieves good agreement with the measurements for the high-frequency modulation in the purely Ohmic discharge #10589 in ASDEX-Upgrade for $\alpha = 1.75$. This disagreement suggests that fractional transport does not play a major part in determining the thermal waves excited in power modulation experiments.

The dissertation of Adam Bryce Kullberg is approved.

Diego del-Castillo-Negrete

Russel Caflisch

Troy Carter

Warren Mori

George Morales, Committee Chair

University of California, Los Angeles
2014

Table of Contents

List of Figures

List of Tables

ACKNOWLEDGMENTS

Several chapters in this thesis are approximate reproductions of published papers by this author: Chapter 2 is a version of [Transport in the spatially tempered, fractional Fokker-Planck equation, A. Kullberg and D. del-Castillo-Negrete (2012), *J. Phys. A: Math. Theor.* **45** 255101]; Chapter 3 is a version of [Isotropic model of fractional transport in two-dimensional bounded domains, A. Kullberg, D. del-Castillo-Negrete, G.J. Morales, and J.E. Maggs (2013), *Phys. Rev. E* **87** 052115]; Chapter 5 is a version of a submitted manuscript [Comparison of a Radial Fractional Transport Model with Tokamak Experiment, A. Kullberg, G.J. Morales, and J.E. Maggs, submitted to Physics of Plasmas on Dec. 10, 2013]. In Chapter 2, the perturbative solution of the tempered fractional Fokker Planck equation was developed by Dr. D. del-Castillo-Negrete. The work presented in this thesis is sponsored by DOE grant SC0004663 at UCLA.

VITA

2007	B.S. in Mathematics, Utah State University. B.S. in Physics, Utah State University.
2008–2010	Teaching Assistant, Physics and Astronomy Department, UCLA.
2010	UCLA Physics and Astronomy Department Outstanding Teaching Award for academic year 2009-2010.
2010–2013	Graduate Student Researcher, Physics and Astronomy Department, UCLA.

PUBLICATIONS

Transport in the spatially tempered, fractional Fokker-Planck equation, A. Kullberg and D. del-Castillo-Negrete (2012), *J. Phys. A: Math. Theor.* **45** 255101

Isotropic model of fractional transport in two-dimensional bounded domains, A. Kullberg, D. del-Castillo-Negrete, G.J. Morales, and J.E. Maggs (2013), *Phys. Rev. E* **87** 052115

Kullberg, A., del-Castillo-Negrete, D., Morales, G. J., and Maggs, J. E., "Nonlocal Transport Across Shear Flows", 52nd Meeting of the Division of Plasma Physics of the American Physical Society, Chicago, Ill., November 8-12, 2010, APS Bull. 55, 321 (2010).

Kullberg, A., del-Castillo-Negrete, D., Morales, G. J., and Maggs, J. E., "Two-dimensional non-local transport across zonal shear flows", 53rd Meeting of the Division of Plasma Physics of the American Physical Society, Salt Lake City, Utah, Nov. 14-18, 2011, CP9.69.

Kullberg, A., del-Castillo-Negrete, D., Morales, G. J., and Maggs, J. E., "Non-local models of nondiffusive transport in magnetically confined plasmas", 54th Meeting of the Division of Plasma Physics of the American Physical Society, Providence, Rhode Island, Oct. 29 - Nov. 2, 2012, Poster Session I, 9:30 AM, Monday

Kullberg, A., Morales, G.J., Maggs, J.E., and del-Castillo-Negrete, D., "Comparison of a 2D Fractional Transport Model with Tokamak Experiments", 55th Meeting of the Division of Plasma Physics of the American Physical Society, Denver, Colorado, Nov. 11-15, 2013, GP8.00010

CHAPTER 1

Introduction

1.1 Motivation and History

A vital topic in developing a working fusion reactor is understanding the transport properties of a confined plasma. In most transport models that have been applied to magnetically confined plasmas, the transport paradigm has consisted of the continuity equation and an expression for the flux that includes terms due to Fick's law and convection:

$$\begin{aligned} \frac{\partial}{\partial t} T &= -\nabla \cdot \vec{q} \\ \vec{q} &= -\chi_d \nabla T + \vec{V} T \ . \end{aligned} \tag{1.1}$$

In many situations, however, this model is insufficient. Within the field of plasma physics, examples of non-diffusive transport, or transport in which equations (1.1) fail, are as follows: the fast propagation phenomena in perturbative transport experiments [CMN08, Gen95, MR06], the non-Gaussianity of experimentally measured fluctuations [JKK03, Gon03], numerical simulations of 3-dimensional, resistive, pressure gradient-driven plasma turbulence in cylindrical [CCL04, CCL05, CLZ01] and toroidal geometry [GC06], gyro-kinetic turbulence [SNL08], and observations of nonlocal enhanced heat transport in magnetized temperature filament experiments [BMM00, PSM08].

The deficiencies associated with the standard diffusion paradigm of equations (1.1) have motivated the study of a class of nonlocal, non-diffusive transport models which are based on *fractional derivative operators.* These fractional derivatives are, mathematically, integro-differential operators that extend the definition of regular differentiation [OS74, Pod99, SKM93] to arbitrary real values. An intuitive representation of a fractional derivative, for example, can be found in the Fourier transform of a one-dimensional, symmetric, fractional derivative in the unbounded domain:

$$\mathcal{F}\left\{\frac{d^\alpha}{d|x|^\alpha} f(x)\right\} = -|k|^\alpha \hat{f}(k) \ . \tag{1.2}$$

In this equation, α is the order of the fractional derivative and is a continuous real parameter such that $0 < \alpha < 2$.

The use of fractional derivative operators in the description of non-diffusive transport is appealing for several reasons. One reason is the connection between fractional derivatives and non-Gaussian Lévy processes. In the context of Continuous Time Random Walk (CTRW) models, fractional operators in the spatial variable appear in the coarse grained description of a generalized random walk in which the underlying jump probability density function (PDF) of the stochastic process corresponds to Lévy flights [MK00, SZK93]. The distributions associated with Lévy flights have divergent second and higher moments, i.e. $\langle x^2 \rangle > \infty$, and as a result, they have long algebraic tails that allow for anomalously large displacements. Thus fractional derivatives operators form a natural model for transport in systems in which large non-Gaussian displacements are present.

Fluid limit descriptions of CTRW models can also contain fractional derivatives when the waiting time distributions obey algebraic scaling laws. In this case, the relevant transport equations contain fractional derivatives in the time variable and describe systems in which memory effects play a significant part in the transport process. In this work, all transport processes are assumed to be Markovian, i.e., no memory effects are included, and so in the transport equations considered here, fractional derivative operators only appear in the space variable.

Over the years, a great deal of research has been devoted to the use of fractional derivative operators in the description of non-diffusive transport. For example, fractional diffusion equations have been developed and discussed in the context of Hamiltonian chaotic dynamics [Zas94, ZEN97], turbulent systems near their critical point in phase space [Pes87], quantum chaotic dynamics [KBD99], and the transport of liquids in porous silica glass [ZSK99]. In each of these cases, the resulting transport equation contained fractional derivatives in space, indicating an underlying transport process containing Lévy flights, or in time, indicating the presence of memory effects. A more thorough survey of fractional dynamics can be found in Refs. [MK00, MK04].

The goal of this thesis is to address several limitations in the current state of the art fractional models, and to apply fractional transport concepts to transport in confined plasmas. One limitation that this thesis addresses is the discrepancy between the strict mathematical properties of the Lévy distributions that underlie fractional diffusion models and the PDFs that are observed in experiment and numerical simulation. For example, the second and higher moments of the Lévy distributions are strictly infinite; in contrast, the moments of observed PDFs are finite since the statistical samples from which they are constructed are finite and do not allow jumps larger than some maximum value. In Refs. [Kop95, Ros07] truncated or tempered Lévy distributions are introduced which guarantee the finiteness of all the moments by including an exponential damping in the Lévy densities. These tempered Lévy statistics motivated the development of truncated fractional derivatives and tempered fractional diffusion models in Ref. [CC07]. In Chapter 2 of this thesis, these truncated fractional derivatives are incorporated into a tempered fractional Fokker Planck equation, and the transport of particles under the influence of tempered Lévy noise and external potentials is studied.

Other limitations that this thesis addresses are related to the dimensionality of the fractional derivatives commonly used to model transport, and the application of fractional derivatives to transport in bounded, finite-sized domains. Many fractional models of transport are based on one-dimensional Cartesian fractional derivatives, regardless of the dimensionality of the system in which the transport occurs. Furthermore, there are subtleties in applying fractional derivative operators, which are often formulated on an unbounded domain, to a finite domain. For example in Ref. [Cas06], a bounded domain Cartesian fractional model is proposed that is based on the Caputo formulation of the fractional derivative which avoids the singularities at the boundary that appear when truncating the range of other types of fractional derivatives, such as the Riemann-Liouville derivative [Pod99]. In Ref. [CMN08] this model is applied to radial transport situations observed in the major European tokamak device JET[Gor08] during cold pulse and perturbative power modulation experiments. Although Cartesian models are reasonable in the slab approximation, in cylindrical systems they are insufficient in describing transport near the origin. Moreover, there is no straightforward method for modeling isotropic transport in the poloidal direction with Cartesian operators. In Chapter 3 of this thesis, a fully two-dimensional fractional Laplacian is developed from a two-dimensional master equation associated with a Continuous Time Random Walk model. The resultant 2D fractional diffusion equation is expanded into a poloidal Fourier series, giving a fractional diffusion equation for each poloidal mode $T^{(n)}$ of the expansion of the transported scalar T. The fractional diffusion equation for $n = 0$ describes isotropic transport in an azimuthally symmetric system. This radial fractional diffusion equation correctly incorporates, near the origin, all the geometric effects of a 2D circular system. Transport in the poloidal direction is described by including the higher $n > 0$ solutions $T^{(n)}$ in the calculation of T. Furthermore, in Chapter 3, an $n = 0$ bounded domain, radial diffusion equation is also developed that is based on the use of mask functions to modify the unbounded domain kernel. This method produces a bounded domain model that avoids the mathematical singularities associated with directly truncating the range of integration in the Riemann-Liouville expression of the fractional derivative; it also avoids a spurious heat flux term that is present in the Caputo expression of the fractional derivative.

In Chapter 4, a derivation is presented of an analytic solution to the one-dimensional unbounded domain fractional diffusion equation in the presence of a harmonically oscillating delta function source. To the author's knowledge, no such thermal wave solution is present in the literature. From this derivation it is learned that there are two contributions to the solution: an evanescent wave-like part, with a wave-number k that is determined by a fractional dispersion relation, and an anomalous algebraically decaying part $H(x)$. It is hoped that knowledge of the analytic thermal wave solutions will allow the development of some perturbative experiment that can determine the fractional order α, and other relevant transport properties, of a fractional system.

Finally, in Chapter 5, results from the $n = 0$ bounded domain radial fractional model developed in Chapter 3 are compared to experimental measurements from several different tokamaks.

1.2 Major results

The major results of this thesis are summarized in this section. In Chapter 2, a tempered fractional Fokker Planck (TFFP) equation is studied in the presence of harmonic and periodic (ratchet) external potentials. The TFFP equation describes the transport of particles governed by a tempered Lévy noise and external forces or potentials. In the presence of a harmonic potential it is found that the steady state solutions of the TFFP equation do not reduce to the Boltzmann distributions in the limit $t \to \infty$ when a finite level of truncation λ is included. However as $\lambda \to \infty$, the steady state solutions $P(x)$ do approach the expected Boltzmann distribution. Figure 2.1 on page 22 shows the numerically calculated PDFs $P(x)$ for increasing λ and show the asymptotic approach to the classical Boltzmann distribution. Previous studies [CGC08] of the (untempered) fractional

Fokker Planck equation have found that a finite current exists in the presence of a periodic potential that lacks reflection symmetry (i.e., a ratchet potential). When truncation is included, these currents are reduced but not eliminated. Figure 2.7 on page 37 shows the reduced current for different levels of truncation λ and for different α. Furthermore, the dependence of the current on other system parameters such as ratchet potential asymmetry A, external tilting force F, and diffusivity scale $\sigma = \chi_\alpha^{1/\alpha}$ is qualitatively similar (aside from a reduction in current magnitude) in both the untempered ($\lambda = 0$) and tempered ($\lambda > 0$) cases; see, respectively, figures 2.12 on page 42, 2.13 on page 43, and 2.16 on page 46. An exception to this general behavior occurs in the presence of an asymmetric Lévy noise (i.e. $\theta \neq 0$) where the inclusion of truncation can change the direction of the current. Figure 2.15 on page 45 plots the current for different fixed asymmetries in the noise and shows a reversed current for increasing λ.

In Chapter 3, a fully 2D fractional diffusion model is derived. This 2D diffusion equation is expanded into a poloidal Fourier series that gives a separate fractional diffusion equation for each term $T^{(n)}$ in the Fourier expansion. This expansion allows for the description of fractional transport in an azimuthally symmetric system (by considering only the $n = 0$ term) and allows one to account for poloidal fractional transport (by considering the $n > 0$ terms). This expansion is given in equation (3.18) on page 55. From the unbounded domain operator, a bounded domain $n = 0$ radial fractional model is developed using kernels that have been modified with mask functions. The resulting bounded domain model is given by equation (3.48) on page 65. A numerical scheme that solves the non-trivial integro-differential part of the bounded domain model is given in the appendix B. The bounded domain radial model allows for the presence of uphill transport over a large extent of the domain. By uphill transport it is meant that the heat flux is in the direction of the temperature gradient. Figure 3.6 on page 73 shows the resulting flux and steady temperature profiles for a strong off-axis heating situation. In that figure, the temperature profile is hollow, or peaks near the off-axis source, and has a region of uphill transport that extends from the origin to 72% of the domain radius. These hollow profiles are a characteristic of the radial fractional model when the diffusivity is constant. In figure 3.7 on page 74, the temperature profiles calculated from the radial fractional model are compared to temperature profiles found from the Cartesian model proposed in Ref. [Cas06]. In that work, the Cartesian model produces profile peaking, or an enhancement in the core temperature, when a strong off-axis heat source is present. This is in contrast to the hollow profiles of the radial fractional model.

In Chapter 4 analytic solutions to the one-dimensional fractional thermal wave problem are derived. The solution is given in equation (4.20) on page 94. The main insight that is learned from the analytic expression is that there are two contributions to the solution: an evanescent wave-like term, with wavenumber k given by a fractional dispersion relation (equation (4.19) on 94), and an anomalous algebraic-decaying term $H(x)$ (equation (4.21) on 94). Figure 4.3 on page 98 shows the log-normal plots of the amplitude and the plots of the phase for a thermal wave due to a symmetric fractional diffusion. The phase panel of this figure displays an interference pattern due to the evanescent wave term and the anomalous $H(x)$ term.

In Chapter 5 calculations from the radial fractional model developed in Chapter 3 are compared to experimental results from several different tokamak devices. The survey presented in this Chapter concentrates on experimental results from the devices: Rijnhuizen Tokamak Project (RTP), ASDEX-Upgrade, JET, and DIII-D. In the RTP, steady off-axis ECH experiments have observed hollow electron temperature profiles that peak near the power source location. These steady hollow profiles are well reproduced by the radial fractional model: see figure 5.4 on page 117 which compares experimental data, the calculated results from the radial fractional model, and results from an internal transport barrier model proposed by de Baar et al. in Ref. [BBH99]. Also, in the RTP experiments, several hollow profiles are found for different heating locations. In figure 5.3 on page 116 the results from the radial fractional model, for each different power location, are compared to experimental results. It is found that as the heating source is moved towards the outer edge, the α value of the best fitting fractional result decreases. This suggests that either the global fractional order α is changed as the heating location is moved, or that the parameter α should depend on the spatial variable ρ such that $\alpha(\rho)$ decreases with ρ. Such an $\alpha(\rho)$ profile would correspond to a system that has increasingly non-local and anomalous transport towards the edge of the domain.

With regards to ASDEX-Upgrade, JET, and DIII-D, Chapter 5 applies the fractional model to off-axis power modulation experiments performed in those devices. These devices are chosen because the equilibrium temperature profiles for each specific modulation experiment are readily available in the literature. In figures 5.7 on page 125, and 5.8 on page 126 calculated results from the radial fractional model are compared to experimental results from ASDEX-Upgrade discharges #10589 and #10591, respectively. These two discharges represent two different experimental regimes: discharge #10589 included steady Ohmic heating, a dominant modulated ECH source, and a higher modulation frequency of 100 Hz, while discharge #10591 included steady ECH heating and steady Ohmic heating, a weaker perturbative modulated ECH source, and a lower modulation frequency of 30 Hz. From figure 5.7 (i.e. discharge #10589), one observes reasonably good agreement between the fractional results for $\alpha = 1.75$ and the measured results. From figure 5.8 (i.e. discharge #10591) it is seen that none of the calculated fractional results agree well with the experimental data; however the best fit is found for $\alpha = 2.0$, corresponding to conventional diffusion with diffusivity obtained from a power balance analysis. Figure 5.9 on page 127 compares the radial fractional model to results from a critical temperature gradient model proposed by Imbeaux et al. in Ref. [IRG01], and experimental data for discharge #10589 in ASDEX-Upgrade.

Figure 5.12 on page 132 compares calculated results from the radial fractional model, a Cartesian Caputo fractional model proposed by del-Castillo-Negrete in Ref. [CMN08], and a critical temperature gradient model given in Ref. [MCG08], to experimental results taken from JET discharge #55809. In this figure both the CGT model and the Cartesian fractional model fit the experimental data better than the radial fractional model. As the Cartesian fractional calculation included Fick's law diffusion, this suggests that an adequate description of transport in this experiment must include at least some level of conventional diffusion.

Figure 5.14 on page 136 compares the calculations from the radial fractional model to experimental results from DIII-D reported in Ref. [DPW12]. In these calculations, the power source profile width is varied and fitted to the experimental data. It is found that for both a fractional model ($\alpha = 1.75$), and a conventional diffusion model, good agreement can be achieved between calculation results and experimental measurements. However, the fractional calculations require a modulation source profile with an unrealistically large width, suggesting that transport in DIII-D may be adequately described by conventional Fick's law diffusion.

CHAPTER 2

Transport in the spatially tempered, fractional Fokker-Planck equation

2.1 Introduction

The problem of fluctuation-driven transport has a long and interesting history, with early discussions dating back to a work by Smoluchowsky in 1912 [Ula57]. As is well known, when the fluctuations follow Gaussian statistics, the dynamics of the probability density function (PDF) can be described, in the continuum limit, using the Fokker-Planck equation. However, there has been growing interest in the study of modified versions of the Fokker-Planck equation that describe transport processes involving anomalous diffusion. In this chapter, a particular interest is the inclusion of tempered fractional diffusion operators in the Fokker-Planck equation.

From the statistical mechanics point of view, there is a close connection between fractional diffusion operators and non-Gaussian Lévy processes. In the context of the continuous time random walk (CTRW) model, fractional diffusion operators arise naturally from the continuum (long wavelength) limit of the generalized random walks with jump PDFs corresponding to Lévy flights; see, e.g., Ref. [MK00] and references therein. Lévy statistics have been used to model a wide range of problems involving PDFs with slowly decaying tails. However, an often-overlooked issue is the differences that exist between the strict mathematical properties of Lévy distributions and the PDFs found in practical problems involving experiments or numerical simulations. For example, although the second and higher moments of an α-stable Lévy distribution with $1 < \alpha < 2$ are formally infinite, all the moments of PDFs of practical interest are finite. One of the reasons why PDFs of practical interest have finite moments is that they typically have finite support since the statistical samples upon which they are constructed are finite. For example, PDFs with algebraic decaying tails have been observed in the description of particle displacements in turbulent transport [CCL05]. These numerically determined PDFs have finite moments because their support is limited by the largest possible displacement computed in the numerical simulation.

One alternative to overcome the divergence of the moments of Lévy α-stable distributions in transport models is to use truncated, or tempered Lévy distributions. These distributions were originally introduced in [MS94, Kop95] as a simple prescription to guarantee the finiteness of the second moment. In [Ros07], a general class of multivariate-tempered stable Lévy processes was considered and their parametrization and probabilistic representations were established. General Lévy processes, and in particular tempered stable processes, were incorporated into the CTRW model and macroscopic transport models in [CC07]. In that work, the notions of truncated fractional derivatives and tempered fractional diffusion (TFD) in the construction of non-diffusive transport models driven by truncated Lévy flights were introduced.

Truncated Lévy distributions have shown applicability in many areas. In plasma physics, it has been shown that these distributions reproduce the PDF of the electrostatic potential fluctuations measured in the edge of Ohmically heated tokamaks [JKK03]. In fluid mechanics, it was observed that the PDF and the scaling properties of truncated Lévy processes display several features of two-dimensional turbulence simulations including a sharp transition from the algebraic to the exponential decay in the tails of the velocity probability distribution function [DL98]. Truncated Lévy distributions were used in [BSC04] to fit and model the statistics of interplanetary solar-wind velocity and magnetic velocity fluctuations measured in the heliosphere. In finance, it has been shown that truncated Lévy distributions describe the scaling of the PDF of the S&P 500 economic index [MS95].

Given the vast literature in the study of fractional diffusion, it is important for applications to explore the role of tempering. Of particular interest is to study how the results obtained in the context of models that assume Lévy distributions with infinite moments are modified when tempering is incorporated. For example, in [Cas09], the role of tempering on the super-diffusive acceleration of fronts in reaction-diffusion systems in the presence of fractional diffusion was studied. In this chapter the goal is to study the role of tempering in the fractional Fokker-Planck equation.

The approach taken in this chapter is based on the spatially tempered, fractional Fokker Planck (TFFP) equation, obtained by replacing the diffusion operator with the truncated fractional diffusion operator introduced in [CC07]. Two complementary numerical techniques are used: a finite-difference method based on the Grunwald-Letnikov discretization of the truncated fractional derivatives, and a Fourier-based spectral method. The discussion focuses on the study of harmonic (quadratic) confining potentials and on the study of periodic potentials with broken spatial symmetry, also known as ratchet potentials. Previous studies in the context of the standard (α-stable) fractional Fokker-Planck equation for confining potentials include the case of harmonic [JMF99, CG00] and non-harmonic [CGK02, SG03, DS07] potentials, and the study of Kramers' problem in [Dit99, CGK05, DGH07, IP06]. The study of the standard fractional Fokker Planck equation with periodic potentials with broken symmetry is more recent. The early work reported in [CGC08] originally proposed a minimal model for Lévy ratchets consisting of a time-independent ratchet potential in the presence of uncorrelated Lévy noise. It was shown that, even in the absence of an external tilting force or time dependence in the potential, or a bias in the noise, the Lévy flights drive the system out of thermodynamic equilibrium and generate an uphill current (i.e., a current in the direction of the steeper side of the asymmetric potential). Following this, in [DGS08], the Lévy ratchet problem was studied and robust probability measures of directionality of transport were proposed. In [Dyb08], the influence of periodically modulated Lévy noise asymmetry was studied.

In the context of fusion plasmas, ratchet models have been invoked to explain the inwardly directed transport of impurity ions[VSB06] in tokamaks; in that model, the random noise is a Gaussian process, instead of a tempered (or untempered) Lévy process, and the directed current is driven by a time-dependent stochastic electrostatic potential and the asymmetry in the magnetic field magnitude across the tokamak cross-section.

The rest of the chapter is organized as follows. In section 2.2, the main ideas behind TFD are discussed. In particular, the truncated fractional derivative operator is defined, the fundamental solution (Green's function) of the TFD equation is computed and a large-truncation expansion of the TFD operator is presented. In section 2.3, perturbative and numerical steady-state solutions of the truncated fractional Fokker-Planck equation for a harmonic potential are presented. The case of periodic potentials with broken spatial symmetry is considered in section 2.4. In this section, a numerical solution of the PDF along with a detailed study of the ratchet current as a function of the truncation level is also presented. The conclusions are presented in section 2.5.

2.2 Review of tempered fractional diffusion

The concept of tempered fractional diffusion (TFD) is first introduced in Ref. [CC07] in the context of the CTRW model. In that work, the following model is proposed to study the fluid (long-wavelength) limit of a CTRW with tempered

Lévy jump distribution functions:

$$ {}_0^c D_t^\beta \, P = \chi_\alpha \, \partial_x^{\alpha,\,\theta,\,\lambda} \, P \ , \tag{2.1}$$

where the parameter $\chi_\alpha > 0$ is the fractional diffusivity. The operator on the left-hand side of the equation (2.1) is the Caputo fractional derivative of order $0 < \beta < 1$, which in the limit $\beta \to 1$ reduces to the regular time derivative, d/dt. The operator on the right-hand side is the TFD operator defined in [CC07] as

$$\partial_x^{\alpha,\,\theta,\,\lambda} \, P = \mathcal{D}_x^{\alpha,\,\theta,\,\lambda} \, P + v \, \frac{d}{dx} \, P - \nu P \ , \tag{2.2}$$

where $\mathcal{D}_x^{\alpha,\,\theta,\,\lambda}$ is the λ-truncated fractional derivative of order $0 < \alpha < 2$ and asymmetry $-1 < \theta < 1$:

$$\mathcal{D}_x^{\alpha,\,\theta,\,\lambda} = l(\theta) \, \exp(-\lambda x) \, {}_{-\infty}D_x^\alpha \, \exp(\lambda x) + r(\theta) \, \exp(\lambda x) \, {}_x D_\infty^\alpha \, \exp(-\lambda x) \ , \tag{2.3}$$

with the parameter $\lambda > 0$ determining the level of the truncation. The operators ${}_{-\infty}D_x^\alpha$ and ${}_x D_\infty^\alpha$ are the well-known Riemann-Liouville derivatives, which in Fourier space are defined as

$$\mathcal{F}\left[{}_{-\infty}D_x^\alpha\right] = (-ik)^\alpha \, \hat{P}, \quad \mathcal{F}\left[{}_x D_\infty^\alpha\right] = (ik)^\alpha \, \hat{P} \ , \tag{2.4}$$

when the Fourier transforms are defined as

$$\mathcal{F}\left[f\right](k) = \hat{f} = \int f(x) \, \exp(ikx) \, \mathrm{d}x \ . \tag{2.5}$$

The factors

$$l = -\frac{1-\theta}{2\cos(\alpha\pi/2)}, \quad r = -\frac{1+\theta}{2\cos(\alpha\pi/2)} \ , \tag{2.6}$$

determine the relative weight of the left and the right fractional derivatives in terms of the asymmetry parameter θ, and

$$v = \begin{cases} 0, & 0 < \alpha < 1 \\ \dfrac{\alpha\theta\lambda^{\alpha-1}}{|\cos(\alpha\pi/2)|} & 1 < \alpha < 2 \end{cases} , \quad \nu = -\frac{\lambda^\alpha}{\cos(\alpha\pi/2)} \ . \tag{2.7}$$

In the context of the CTRW model, the order α of the fractional derivative and the parameter λ correspond to the index and tempering of the Lévy density $w_{ET}(x) \sim |x|^{-(1+\alpha)} \exp(-\lambda|x|)$ which describes the statistics of the particle jumps. In detail, for this Lévy density, the Lévy -Kintchine formula gives the following expression for the characteristic exponent Λ_{ET} of the PDF of jumps η:

$$\begin{aligned}\Lambda_{ET} &= \ln \hat{\eta} = -\frac{\chi_\alpha}{2\cos(\alpha\pi/2)} \\ &\times \begin{cases} (1+\theta)(\lambda+ik)^\alpha + (1-\theta)(\lambda-ik)^\alpha - 2\lambda^\alpha, & 0 < \alpha < 1 \\ (1+\theta)(\lambda+ik)^\alpha + (1-\theta)(\lambda-ik)^\alpha - 2\lambda^\alpha - 2ik\alpha\theta\lambda^{\alpha-1}, & 1 < \alpha \leq 2 \end{cases}\end{aligned} \tag{2.8}$$

where $\hat{\eta} = \exp(\Lambda_{ET}(k))$ denotes the Fourier transform of η. From equation (2.8), it follows that, for $\lambda > 0$, all the moments of the jump PDF η are finite since

$$\langle \delta x^n \rangle_\eta = \int \delta x^n \, \eta \, \mathrm{d}\delta x = i^{-n} \left. \frac{\partial^n \hat{\eta}}{\partial k^n} \right|_{k=0} . \tag{2.9}$$

For example,

$$\langle \delta x \rangle_\eta = \begin{cases} V_*, & 0 < \alpha < 1 \\ 0, & 1 < \alpha < 2 \end{cases} , \tag{2.10}$$

and

$$\langle (\delta x)^2 \rangle_\eta = 2\chi_* + \langle \delta x \rangle_\eta^2 \quad 0 < \alpha < 2, \tag{2.11}$$

where the asterisked quantities are defined as

$$V_* = \frac{-\chi_\alpha \alpha \theta}{|\cos(\alpha\pi/2)|\, \lambda^{1-\alpha}}, \quad \chi_* = \frac{\chi_\alpha \alpha |\alpha - 1|}{2|\cos(\alpha\pi/2)|\lambda^{2-\alpha}}. \tag{2.12}$$

For $\lambda = 0$ (i.e. the absence of truncation), the Lévy density reduces to that of an α-stable Lévy process, $w_{LS}(x) \sim |x|^{-(1+\alpha)}$, and equation (2.2) reduces to Riemann-Liouville fractional derivatives. As expected, in this limit, $\langle \delta x^2 \rangle_\eta \to \infty$. In addition, if $\theta \neq 0$, $\langle \delta x \rangle_\eta \to \infty$ for $0 < \alpha < 1$. On the other hand, as expected, in the limit $\alpha \to 2$, the right-hand side of equation (2.1) reduces to the diffusion Laplacian operator $\partial_x^2 P$. Further details on the definition and properties of the TFD operator and the λ-truncated fractional derivative can be found in

[CC07, Cas]. Finally, as is well known, (see [MK00] and references therein) for $0 < \beta < 1$, the operator ${}_0^cD_t^\beta$ on the left-hand-side of equation (2.1) accounts for memory effects resulting from waiting time PDFs with algebraic decaying tails in the CTRW.

In principle, it is possible to generalize the previous discussion to model transport processes in which the truncation itself is asymmetric. One possible way to do this is by assigning different truncation scales to the left and the right fractional derivatives:

$$\Delta^{\alpha,\,\theta,\,\lambda_l,\,\lambda_r}\,P = a_l\,\partial_x^{\alpha,\,-1,\,\lambda_l}\,P + a_r\,\partial_x^{\alpha,\,1,\,\lambda_r}\,P, \tag{2.13}$$

where $a_l = (1-\theta)/2$ and $a_r = (1+\theta)/2$, with $-1 < \theta < 1$. However, in this thesis, the discussion focuses solely on the symmetric truncation case, which corresponds to $\lambda_r = \lambda_l = \lambda$. In this case $\Delta^{\alpha,\,\theta,\,\lambda_l,\,\lambda_r}\,P = \partial_x^{\alpha,\,\theta,\,\lambda}\,P$.

2.2.1 Green's function and temporal scaling of moments

The fundamental solution of the TFD equation is given by the solution of the initial value problem

$${}_0^cD_t^\beta\,G_\lambda = \chi_\alpha\,\partial_x^{\alpha,\,\theta,\,\lambda}\,G_\lambda, \quad G_\lambda(x,0) = \delta(x)\ . \tag{2.14}$$

Using the Fourier transform properties of the truncated fractional derivatives

$$\begin{aligned} \mathcal{F}\left[\exp\left(-\lambda x\right)\ {}_{-\infty}D_x^\alpha\ \exp\left(\lambda x\right)\ \phi\right] &= \left(\lambda - ik\right)^\alpha\ \hat{\phi} \\ \mathcal{F}\left[\exp\left(\lambda x\right)\ {}_xD_\infty^\alpha\ \exp\left(-\lambda x\right)\ \phi\right] &= \left(\lambda + ik\right)^\alpha\ \hat{\phi} \end{aligned}\ , \tag{2.15}$$

it follows that

$$G_\lambda(x,t) = \frac{1}{2\pi}\int_{-\infty}^{\infty}\exp\left(-ikx\right)\ E_\beta\ \left[t^\beta\,\Lambda_{ET}(k)\right]\ \mathrm{d}k, \tag{2.16}$$

where E_β is the Mittag-Leffler function of order β [CC07].

As mentioned before, one of the key issues of the tempered Lévy distributions is the finiteness of the moments. Likewise, for $\lambda > 0$, all the moments of the

Green's function exist, viz. $\langle x^n \rangle = \int x^n\, G_\lambda\, \mathrm{d}x = i^{-n}\, \partial_k^n\, \hat{G}_\lambda \Big|_{k=0}$. The temporal scaling of the first and second moments are given by

$$\langle x \rangle = \begin{cases} \dfrac{V_*}{\Gamma(\beta+1)}\, t^\beta, & 0 < \alpha < 1, \\ 0, & 1 < \alpha < 2, \end{cases} \tag{2.17}$$

and

$$\langle [x - \langle x \rangle]^2 \rangle(t) = \begin{cases} C_\beta^2\, V_*^2\, t^{2\beta} + \dfrac{2\chi_*}{\Gamma(\beta+1)}\, t^\beta, & 0 < \alpha < 1, \\ \dfrac{2\chi_*}{\Gamma(\beta+1)}\, t^\beta, & 1 < \alpha < 2, \end{cases} \tag{2.18}$$

where $C_\beta = 2/\Gamma(2\beta+1) - 1/\left[\Gamma(\beta+1)\right]^2$, and V_* and χ_* are defined in equation (2.12). Note that the truncation gives rise to a finite first moment for $\theta \neq 0$ only when $0 < \alpha < 1$. In this case, the scaling is sub-advective for $0 < \beta < 1$. Although less studied than anomalous diffusion, anomalous advection, characterized by $\langle x \rangle \sim t^\zeta$ with $\zeta \neq 1$, has been observed in transport problems in fluid mechanics [Cas98]. As expected, according to equations (2.10), the constant V_* is the first moment of the asymmetric, truncated jump distribution function in the CTRW for $0 < \alpha < 1$. Moreover, as discussed below, V_* determines the effective drift velocity in the large-λ expansion of the transport equation (2.33) for $0 < \alpha < 1$.

Two cases of particular interest in the solution of equation (2.14) correspond to symmetric and totally asymmetric Green's functions. In the symmetric, $\theta = 0$, case, the Green's function for $1 < \alpha < 2$ can be written as

$$\frac{\pi}{\lambda}\, G_\lambda(\tilde{x}, \tau) = \int_0^\infty \cos(\tilde{x} u)\, E_\beta\left[\tau^\beta \Phi(u)\right]\, \mathrm{d}u, \tag{2.19}$$

where

$$\Phi(u) = \frac{1}{|\cos(\alpha\pi/2)|}\, \left[\left(1 + u^2\right)^{\alpha/2} \cos\left(\alpha \tan^{-1}(u)\right) - 1\right]\,, \tag{2.20}$$

and where $\tilde{x} = \lambda x$, $\tau = t/t_c$, and

$$t_c = \chi_\alpha^{-1/\beta}\, \lambda^{-\alpha/\beta}\,. \tag{2.21}$$

As discussed in [CC07, Cas], for $2\beta > \alpha$, the solution in equation (2.19) implies that the scaling of the PDF transitions from super-diffusion at short times to sub-diffusion at large times, with the cross-over time t_c given in (2.21). This transition is accompanied by a transition in the tails of Green's function from algebraic decay to stretched exponential decay. Another case, which is relevant to the study of front propagation in reaction-diffusion systems [Cas09, Cas], corresponds to the totally asymmetric, $\theta = -1$, for $\beta = 1$, and $1 < \alpha < 2$, solution

$$G_\lambda = \exp\left(-\lambda x - \chi_\alpha \lambda^\alpha t\right) \left(\chi_\alpha t\right)^{-1/\alpha} G_0(\tilde{x}) \ , \tag{2.22}$$

where

$$G_0(\tilde{x}) = \frac{1}{2\pi} \int_{-\infty}^{\infty} \exp\left(i^\alpha k^\alpha + ik\tilde{x}\right) \, \mathrm{d}k \ , \tag{2.23}$$

is Green's function of the asymmetric, α-stable ($\lambda = 0$) fractional diffusion equation, in terms of the similarity variable

$$\tilde{x} = x \left(\chi_\alpha \, t\right)^{-1/\alpha}, \tag{2.24}$$

where, for simplicity, it has been assumed that an advection velocity $V = -v$ is present that cancels the drift velocity, which according to equation (2.7) arises for $\lambda > 0$ and $\theta \neq 0$.

Using the asymptotic expression of the α-stable Lévy distributions, $G_0(\tilde{x}) \sim \tilde{x}^{-1-\alpha}$ for $\tilde{x} > 0$, it follows from equation (2.22) that the right tail exhibits the tempered decay

$$G_\lambda \sim \chi_\alpha t \exp\left(-\chi_\alpha \lambda^\alpha t\right) \frac{\exp(-\lambda x)}{x^{1+\alpha}}, \quad x >> \left(\chi_\alpha t\right)^{1/\alpha} \ , \tag{2.25}$$

while the left tail, $x < 0$, exhibits the exponential decay

$$\begin{aligned} G_\lambda \sim \left(\chi_\alpha t\right)^{-(a_2+1)/\alpha} \exp(-\chi_\alpha \, \lambda^\alpha t) \, |x|^{a_2} \exp\left(-b_2 (\chi_\alpha t)^{-c_2/\alpha} |x|^{c_2} + \lambda |x|\right) \ , \\ |x| >> \left(\chi_\alpha t\right)^{1/\alpha} \ , \end{aligned} \tag{2.26}$$

for all values of $\lambda > 0$, where a_2, b_2 and c_2 are constants.

2.2.2 λ-expansion

To further understand the role of truncation, it is useful to consider an expansion of the truncated fractional diffusion operator in the limit of large λ. Taking the Fourier transform of the λ-truncated fractional derivative in equation (2.3), and using equation (2.15), gives

$$\mathcal{F}\left[\mathcal{D}_x^{\alpha,\,\theta,\,\lambda}\,P\right] = \lambda^\alpha\left[l(\theta)\left(1-\frac{ik}{\lambda}\right)^\alpha + r(\theta)\left(1+\frac{ik}{\lambda}\right)^\alpha\right]\hat{P}, \tag{2.27}$$

for $\lambda > 0$. The power functions in equation (2.27) can be replaced with the expansion

$$(1-z)^\alpha = \sum_{j=0}^{\infty} w_j^{(\alpha)}\, z^j, \tag{2.28}$$

which is valid for $|z| < 1$, where $w_j^{(\alpha)}$ are the fractional binomial coefficients, $w_0^{(\alpha)} = 1$, and $w_j^{(\alpha)} = [1-(\alpha+1)/j]\; w_{j-1}^{(\alpha)}$. Doing so gives

$$\mathcal{F}\left[\mathcal{D}_x^{\alpha,\,\theta,\,\lambda}\,P\right] = \lambda^\alpha \sum_{j=0}^{\infty} w_j^{(\alpha)}\left(\frac{ik}{\lambda}\right)^j \left[l(\theta) + (-1)^j\, r(\theta)\right]\,\hat{P} \quad , \tag{2.29}$$

which leads to the following expansion in Fourier space of the truncated fractional diffusion operator in equation (2.2):

$$\begin{aligned}\mathcal{F}\left[\partial_x^{\alpha,\,\theta,\,\lambda}\,P\right] &= -\frac{V_*}{\chi_\alpha}\,H(1-\alpha)\,\widehat{\partial_x P}\\ &\quad - \frac{\lambda^\alpha}{\cos\left(\alpha\pi/2\right)}\sum_{j=1}^{\infty} w_{2j}^{(\alpha)}\left(\frac{ik}{\lambda}\right)^{2j}\left[1-\left(\frac{2j-\alpha}{2j+1}\right)\frac{ik\theta}{\lambda}\right]\hat{P}\ ,\end{aligned} \tag{2.30}$$

where V_* is defined in equation (2.12), and $H(x)$ is the Heaviside function equal to 1 for $x > 0$ and equal to 0 otherwise.

Since the series in equation (2.30) converges in general only for $|k| < \lambda$, care must be taken when inverting the Fourier transform; rigorous inversion of (2.30) requires the use of the low-pass filter operator defined for a given function $f(x)$ as

$$\bar{f}(x) = \mathcal{F}^{-1}\left[H(\lambda-|k|)\,\mathcal{F}[f]\right]\ . \tag{2.31}$$

When applied to $P(x)$, this operator gives the coarse-grained function $\bar{P}(x)$ resulting from filtering all scales with wavelengths smaller than the truncation length scale $1/\lambda$. Applying the low-pass filter to the operator, $\partial_x^{\alpha,\,\theta,\,\lambda} P$, in equation (2.30), gives the following expression for the coarse grained truncated fractional diffusion operator:

$$\begin{aligned}\overline{\partial_x^{\alpha,\,\theta,\,\lambda} P} = & -\frac{V_*}{\chi_\alpha} H(1-\alpha)\,\frac{\partial \bar{P}}{\partial x} \\ & -\frac{1}{\lambda^{2-\alpha}\,\cos(\alpha\pi/2)} \sum_{j=1}^{\infty} \frac{w_{2j}^{(\alpha)}}{\lambda^{2(j-1)}}\,\frac{\partial^{2j}}{\partial x^{2j}} \left[1 + \left(\frac{2j-\alpha}{2j+1}\right) \frac{\theta}{\lambda}\,\frac{\partial}{\partial x}\right] \bar{P}\ ,\end{aligned} \tag{2.32}$$

where the convergence of equation (2.30) is guaranteed because $\hat{\bar{P}}(k) = 0$ for $|k| > \lambda$. The first terms of equation (2.32) yield the following transport equation for the coarse grained PDF at scales larger than $1/\lambda$:

$$\begin{aligned}\frac{\partial}{\partial t}\bar{P} + V_* H(1-\alpha)\,\frac{\partial \bar{P}}{\partial x} = \chi_*\,\frac{\partial^2 \bar{P}}{\partial x^2} + \chi_* \frac{(2-\alpha)\theta}{3\lambda}\,\frac{\partial^3 \bar{P}}{\partial x^3} \\ + \chi_*\,\frac{(3-\alpha)(2-\alpha)}{12\lambda^2}\,\frac{\partial^4 \bar{P}}{\partial x^4} + \ldots ,\end{aligned} \tag{2.33}$$

where V_* and χ_* are defined in equation (2.12).

2.3 Tempered fractional Fokker-Planck equation: harmonic potentials

When TFD is included in the Fokker-Planck equation, the model equation becomes,

$$\frac{\partial}{\partial t} P = \frac{\partial}{\partial x}\left[P \frac{\partial}{\partial x} V\right] + \chi_\alpha\,\partial_x^{\alpha,\,\theta,\,\lambda} P\ , \tag{2.34}$$

where $\partial_x^{\alpha,\,\theta,\,\lambda}$ is the operator in equation (2.2) and V is the potential. In this section steady state solutions ($\frac{\partial}{\partial t} P = 0$) of equation (2.34) are found for harmonic potentials. This is equivalent to solving the following equation

$$P \frac{dV}{dx} - \Gamma_\lambda = 0\ , \tag{2.35}$$

where Γ_λ is the flux defined by

$$-\frac{\partial}{\partial x}\,\Gamma_\lambda = \chi_\alpha\,\partial_x^{\alpha,\,\theta,\,\lambda}\,P\ . \tag{2.36}$$

Explicitly, the harmonic potential used here is given by

$$V(x) = \chi_*\,\tilde{V}_0\,x^2\ . \tag{2.37}$$

In the calculations that follow, it is assumed that $\theta = 0$. The case of steady-state and time-dependent solutions with $\theta \neq 0$ for periodic ratchet-type potentials is considered in section 2.4.

2.3.1 Steady-state solution: Fourier spectral method

A spectral method can be used to numerically compute the steady state solutions. In the case of the harmonic potential (2.37), the Fourier transform of equation (2.35) gives

$$2\tilde{V}_0 k\chi_*\,\frac{d\hat{P}}{dk} = \Lambda_{ET}(k)\,\hat{P}\ , \tag{2.38}$$

where Λ_{ET} is the characteristic exponent of the symmetric, $\theta = 0$, tempered Lévy processes with $1 < \alpha < 2$ as given in equation (2.8). The analytic solution of equation (2.38) is

$$\hat{P}(k) = \exp\left(\mathcal{L}(k)\right)\ ,\quad \mathcal{L}(k) = \frac{1}{2\tilde{V}_0\,\chi_*}\int_0^k \kappa^{-1}\,\Lambda_{ET}(\kappa)\,\mathrm{d}\kappa\ . \tag{2.39}$$

Using the expansion in equation (2.30), the function $\mathcal{L}(k)$ can be written as the series

$$\mathcal{L}(k) = \frac{\lambda^2}{2\alpha|\alpha-1|\,\tilde{V}_0}\sum_{j=1}^{\infty}\frac{(-1)^j}{j}\,w_{2j}^{(\alpha)}\left(\frac{k}{\lambda}\right)^{2j}\ , \tag{2.40}$$

for $|k| < \lambda$.

An approximation of the solution $P(x)$ is found by numerical integration of the Fourier transform using the trapezoid rule and a large computational domain

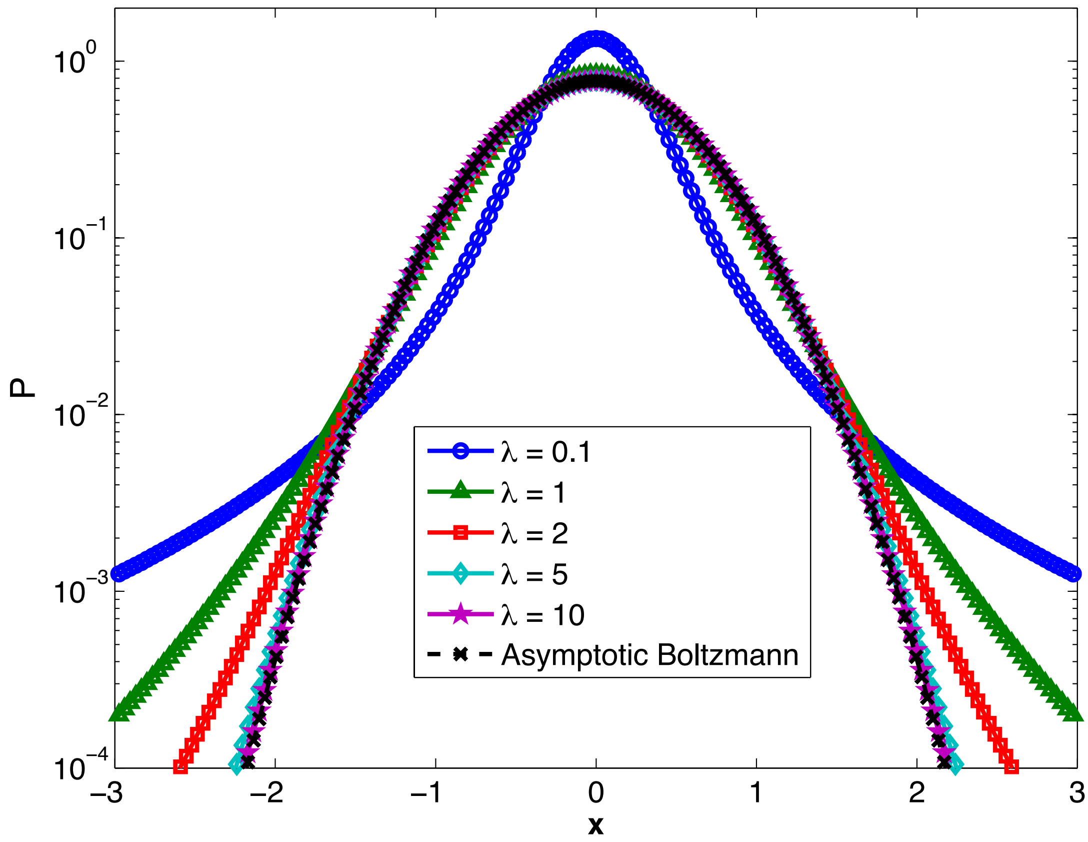

Figure 2.1: Convergence to the Boltzmann distribution in the large truncation, $\lambda >> 1$, limit for the harmonic potential in equation (2.37). The different curves show the numerically computed, steady-state solutions of the TFFP equation (2.34) for $\alpha = 1.5$, and different values of the truncation parameter λ with $\chi_* = \text{constant}$.

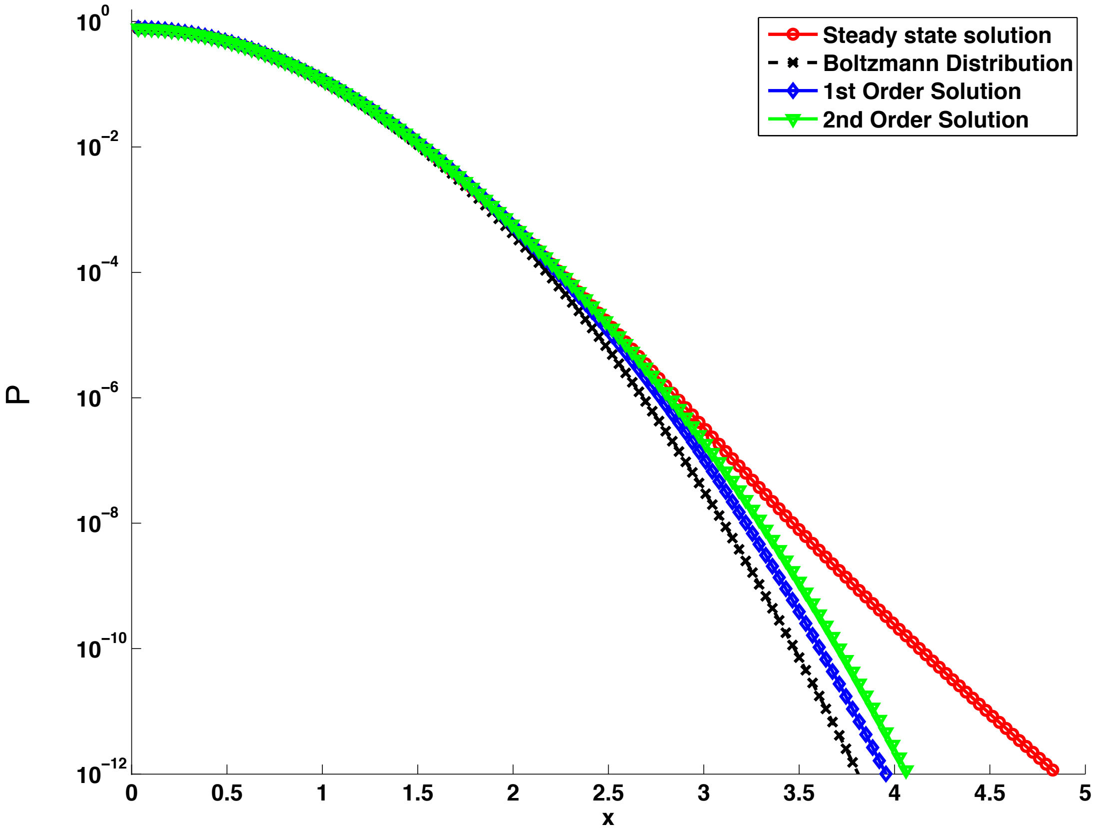

Figure 2.2: Comparison between the first- and the second-order pertubative analytic solution according to equations (2.49) and (2.50), and the numerically computed steady-state solutions of the TFFP equation (2.34) for the harmonic potential in equation (2.37), with $\alpha = 1.5$ and $\lambda = 5$. For reference, the corresponding Boltzmann distribution is also shown.

L

$$P(x) = \frac{1}{\pi} \int_0^\infty \cos(kx)\, \hat{P}(k)\, \mathrm{d}k$$
$$\approx \frac{\Delta k}{\pi} \left[\frac{1}{2} \hat{P}_0 + \frac{1}{2} \cos(k_N x) \hat{P}_N + \sum_{n=1}^{N-1} \cos\left(k_n x\right) \hat{P}_n \right] . \tag{2.41}$$

The first line in equation (2.41) is the inverse Fourier transform for a real symmetric function, i.e., $P(x) \in \Re$ and $P(x) = P(-x)$. The parameters in (2.41) are defined as follows: $k_n = n\Delta k$, $\hat{P}_n = \hat{P}(k_n)$ and $\Delta k N = L >> 1$. The vector $\hat{P}_n$ is obtained by evaluating equation (2.39) at $k = k_n$. For $k_n < \lambda$, $\mathcal{L}(k_n)$ is evaluated using the convergent series in equation (2.40). For $k_n > \lambda$, $\mathcal{L}(k_N)$ is computed using the recursion relation

$$\mathcal{L}(k_n) = \frac{1}{2\tilde{V}_0\, \chi_*} \int_{k_{n-1}}^{k_n} \kappa^{-1}\, \Lambda_{ET}(\kappa)\, \mathrm{d}\kappa + \mathcal{L}(k_{n-1}), \tag{2.42}$$

where the integration between k_{n-1} and k_n is done using Simpson's rule with ten points. The numerically computed steady-state solutions are shown in figure 2.1 for different values of λ and $\chi_* =$ constant. For small values of λ, the PDF approaches the steady-state solution of the α-stable fractional Fokker-Planck equation, which, as originally discussed in [JMF99, YCS00], is a Lévy distribution. On the other hand when λ increases, the solution converges to the Boltzmann PDF of the regular Fokker-Planck equation.

2.3.2 Steady-state solution: perturbation expansion

To gain further insight into the role of truncation, a perturbative solution of the TFFP equation for the coarse-grained distribution $\bar{P}$ can be studied. Using equation (2.32), the steady-state equation (2.35) for $\bar{P}$ can be written as

$$\chi_* \frac{d\bar{P}}{dx} + \bar{P}\frac{dV}{dx} + \chi_* \sum_{k=1}^{\infty} a_k\, \epsilon^k\, \frac{d^{2k+1}}{dx^{2k+1}} \bar{P} = 0 \ , \tag{2.43}$$

where

$$\epsilon = \lambda^{-2} \ , \quad a_k = \frac{2 w^{(\alpha)}_{2(k+1)}}{\alpha(\alpha-1)} \ . \tag{2.44}$$

Although the general solution of equation (2.43) requires the use of numerical methods, this equation can be solve perturbatively in the limit of large truncation or $\epsilon << 1$. This method gives the solution in the form of a perturbative expansion

$$\bar{P} = \sum_{n=0}^{\infty} \epsilon^n \, \mathcal{P}_n(x) \ . \tag{2.45}$$

When (2.45) is inserted into the transport equation (2.43), equating equal powers of ϵ gives a hierarchy of equations for each $\mathcal{P}_n$. The zeroth order term is, as expected, the Boltzmann distribution

$$\mathcal{P}_0(x) = \frac{1}{\mathcal{Z}} \exp\left(-V(x)/\chi_*\right) \ , \tag{2.46}$$

where $\mathcal{Z}$ is a normalization constant. The higher order corrections of the Boltzmann distribution are determined by the recurrence relation

$$\mathcal{P}_n(x) = -\exp\left(-V(x)/\chi_*\right) \sum_{k=1}^{n} a_k \int \exp\left(V(x)/\chi_*\right) \frac{d^{2k+1}}{dx^{2k+1}} \mathcal{P}_{n-k}(x) \, \mathrm{d}x \ , \tag{2.47}$$

for $n > 1$. Note that, for any $\lambda > 0$, the resulting equilibrium distribution is not a Boltzmann distribution if $\alpha \neq 2$. When $\alpha = 2$, all the corrections identically vanish (since $a_k = 0$ for all k), and $P = P_0$ is a Boltzmann distribution. As expected, the Boltzmann distribution is also recovered in the limit $\lambda \to \infty$.

In the case of a quadratic, harmonic potential, as in equation (2.37), the zeroth order ϵ^0 Boltzmann distribution is

$$\bar{P}(x) = \sqrt{\frac{\tilde{V}_0}{\pi}} \exp\left(-\tilde{V}_0 \, x^2\right) \ , \tag{2.48}$$

and the peturbative solution to first order ϵ^1 is

$$\bar{P}(x) = \frac{1}{\mathcal{Z}} \exp\left(-\tilde{V}_0 x^2\right) \left[1 + \frac{\tilde{V}_0}{96 \, \lambda^2} (2-\alpha)(3-\alpha) \, H_4\left(\sqrt{\tilde{V}_0} \, x\right)\right] \ . \tag{2.49}$$

After some algebra, the second order correction $\mathcal{P}_2$ is found to be

$$\mathcal{P}_2 = \tilde{V}_0^2 \left[\frac{a_1^2}{128} H_8\left(\sqrt{\tilde{V}_0} \, x\right) + \frac{a_2}{12} H_6\left(\sqrt{\tilde{V}_0} \, x\right)\right] \mathcal{P}_0 \tag{2.50}$$

Note that in the above corrections H_n denotes the Hermite polynomial of order n. Figure 2.2 shows a comparison between the numerical steady solution and the first- and second-order perturbative solutions.

2.4 Periodic potentials

In this section the TFFP equation is studied for periodic potentials with broken spatial symmetry. These potentials, also called 'ratchets', satisfy a periodicity condition $V(x) = V(x+L)$, where L is the length of the period, but also lack reflection symmetry. A paradigmatic example is $V = V_0\,[\sin(2\pi x/L) + 0.25\,\sin(4\pi x/L)]$. For an easier control of the degree of spatial symmetry, following [CGC08], the potential below is used:

$$V(x) = V_0 \begin{cases} 1 - \cos\left[\pi x/a_1\right], & \text{if } 0 \leq x < a_1, \\ 1 + \cos\left[\pi(x - a_1)/a_2\right], & \text{if } a_1 \leq x < L, \end{cases} \tag{2.51}$$

where V_0 is the amplitude, $L = a_1 + a_2$ is the period and $A = (a_1 - a_2)/L$ is the asymmetry parameter. In all the calculations presented here, $V_0 = L = 1$. In the study of ratchets, it is customary to add an external constant 'tilting' force F to the potential and to consider the effective potential $V_{eff} = V - Fx$. However, unless mentioned otherwise, the calculations presented here for the most part assume $F = 0$. Figure 2.3 shows a plot of the ratchet potential in equation (2.51) with $a_1 = 1/4$, $a_2 = 3/4$, $V_0 = 1$ and $L = 1$ that correspond to $A = -0.5$.

The conditions for the existence of ratchet currents in the presence of diffusive transport have been extensively studied and are well understood; see, e.g. [Rei02] and references therein. However, this is not the case for fluctuation-driven transport in the presence of non-diffusive transport. The study of ratchet currents in the case of fluctuation-driven transport in the presence of α-stable Lévy noise was originally studied in [CGC08] in the context of the α-stable fractional Fokker-Planck equation and the corresponding Langevin equation. The goal of this section is to study this problem in the context of the TFFP equation in equation (2.34) with the potential in equation (2.51).

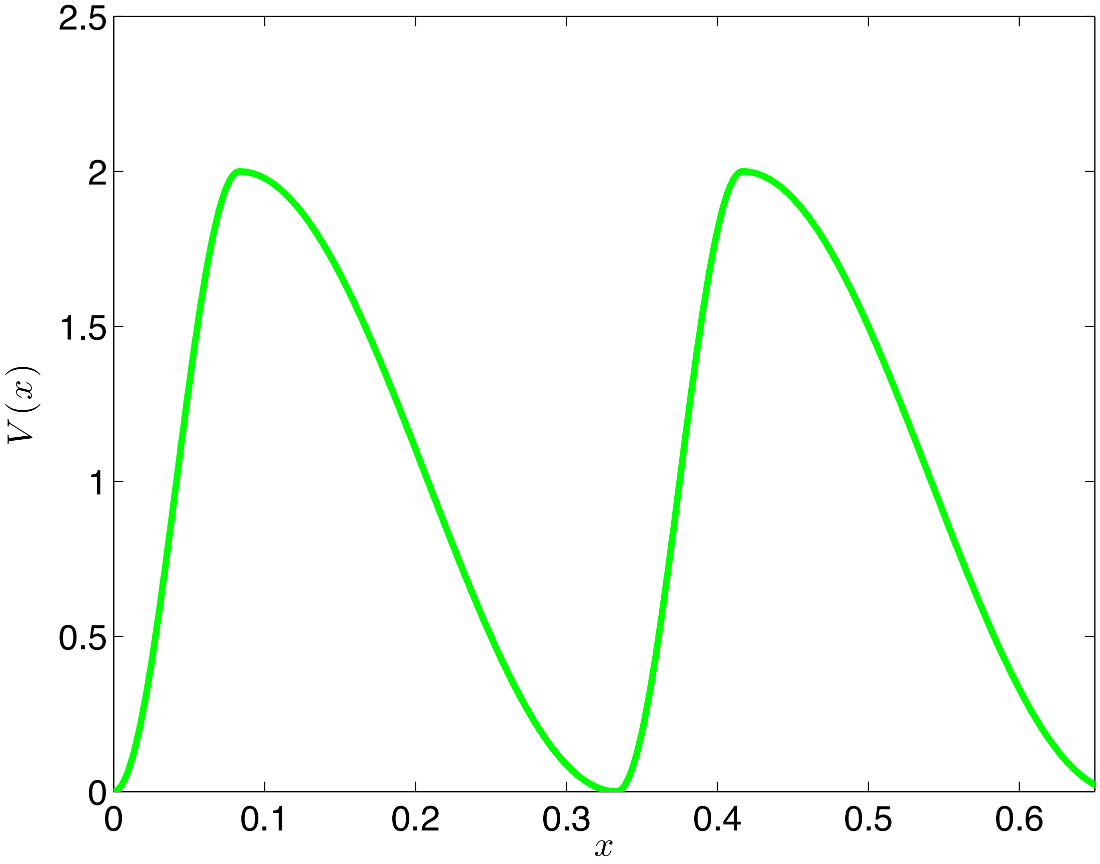

Figure 2.3: Ratchet potential in equation (2.51) for $A = -0.5$ and $V_0 = 1$.

2.4.1 Time-dependent and steady-state solutions

For the solution of the TFFP equation with periodic potentials, two complementary techniques have been used: a finite-difference method and a Fourier spectral method. The finite-difference method is based on the discretization of the truncated fractional diffusion operator in a finite domain. Following the scheme reported in [Cas06], the finite-difference method uses the Grunwald-Letnikov representation of the regularized (in the Caputo sense) fractional derivatives. The incorporation of the contribution of the potential is done using an operator splitting method that separates the time step in a pure TFD step and a pure potential term step. For the time discretization, a weighted average Crank-Nicholson method is used.

The starting point of the alternative Fourier spectral method is the TFFP equation (2.34) in Fourier space

$$\frac{\partial \hat{P}}{\partial t} = \Lambda_{ET}(k)\,\hat{P} - ik\,\mathcal{F}\left[P\,\frac{\partial V}{\partial x}\right](k)\ . \tag{2.52}$$

In general, for a periodic potential, $V(x+L) = V(x)$, the following expansion can be made

$$\frac{\partial V}{\partial x} = \sum_{n=-\infty}^{\infty} c_n\, \exp\left(ik_n x\right)\ , \tag{2.53}$$

where $k_n = 2\pi n/L$, and therefore,

$$\mathcal{F}\left[P\,\frac{\partial V}{\partial x}\right](k) = \sum_{n=-\infty}^{\infty} c_n\,\hat{P}(k+k_n,t)\ . \tag{2.54}$$

Substituting equation (2.54) into equation (2.52) and evaluating the resulting expression at $k = k_n$ gives

$$\frac{d\hat{P}_n}{dt} = \Lambda_n\,\hat{P}_n - ik_n \sum_{j=-\infty}^{\infty} c_j \hat{P}_{n+j}, \tag{2.55}$$

where $\Lambda_n = \Lambda_{ET}(k = k_n)$ and $\hat{P}_n = \hat{P}(k = k_n)$. For steady-state solutions, $d\hat{P}_n/dt = 0$ and the problem reduces to the solution of a set of coupled-algebraic equations:

$$\Lambda_n \hat{P}_n - ik_n \sum_{j=-\infty}^{\infty} c_j \hat{P}_{n+j} = 0. \tag{2.56}$$

In both equations (2.55) and (2.56), $\hat{P}_0$ is constant and normalization of the PDF requires that $\hat{P}_0 = 1$. In the numerical computations, the infinite series in equations (2.55) and (2.56) are truncated at a large value of $n = N >> 1$; typically N ranged from 500 to 2000. From the set of values $\{\hat{P}_n\}$, the PDF corresponding to the steady-state solution of the TFFP equation in a periodic domain is obtained from the inverse Fourier transform: $P(x) = \sum_{n=-N}^{N} \hat{P}_n \exp(ik_n x)$.

In the Fourier spectral method, information about the solution of the TFFP equation for a periodic potential is extracted from the solution of the set of coupled equations given in either equation (2.55) or (2.56). For example, the time dependent values of $\{\hat{P}_n\}$, obtained from (2.55), can be used to calculate the current $J(t)$ of the system for all times. The steady-state values of $\{\hat{P}_n\}$, obtained from (2.56), can be used to find the asymptotic steady-state PDF solution of the TFFP. Note that this steady-state solution is never exactly achieved in the system; instead, as $t \to \infty$ the PDF solution of the TFFP equation is better and better approximated by the asymptotic steady-state solution.

Figure 2.4 shows snapshots in time of the numerically calculated PDFs for different levels of truncation using the finite-difference method. The initial condition corresponds to a PDF localized in the potential well at the middle of the computational domain:

$$P(x, 0) = \frac{1}{\sigma\sqrt{2\pi}} \exp\left(-\frac{(x - 1/2)^2}{\sigma^2}\right), \tag{2.57}$$

with $\sigma = 0.12$. Compared to the $\lambda = 0$ (α-stable) case, it is observed that the tempering reduces the 'leakage' of the PDF out of the potential well. However, for both $\lambda = 0$ and $\lambda = 3$, the profile peaks are higher on the right than on the left, indicating the presence of a net current. The existence of the current for $\lambda = 0$ is consistent with the results previously reported in [CGC08]. The understanding and characterization of the current for $\lambda > 0$ is one of the objectives of this section.

Figure 2.5 shows the steady-state PDF P in the α-stable case, i.e. $\lambda = 0$, for different values of α. As expected, for $\alpha = 2$, P corresponds to the Boltzmann distribution $P(x) = (1/\mathcal{Z}) \exp\left(-V(x)/\chi_\alpha\right)$, where $\mathcal{Z}$ is the normalization constant. As the value of α decreases, the PDF significantly departs from the Boltzmann distribution and develops the asymmetry responsible for the finite net current observed for $\alpha < 2$. The dependence of P on λ with $\chi_\alpha = \chi_0\, \lambda^{2-\alpha}$ for a fixed value of α is shown in figure 2.6. As expected, as the value of λ increases, the PDF approaches the Boltzmann distribution.

2.4.2 Ratchet current

The current $J(t)$ is defined as the rate of change of the first moment, $\langle x \rangle = \int x P \, \mathrm{d}x$,

$$J = \frac{d\langle x \rangle}{dt} = -i \, \frac{\partial}{\partial t} \left(\frac{\partial \hat{P}}{\partial k} \right)_{k=0} , \tag{2.58}$$

where $\hat{P}$ is the solution of the TFFP in Fourier space. From equation (2.58) and (2.52), it follows that

$$J = -i \left(\frac{d\Lambda_{ET}}{dk} \right)_{k=0} - \mathcal{F}\left[P \frac{\partial V}{\partial x} \right]_{k=0} . \tag{2.59}$$

The computation of the first term on the right-hand side follows directly from the definition in equation (2.8). For $1 < \alpha < 2$, this term has no contribution because, $d\Lambda_{ET}/dk = 0$, for any value of λ. However, in the case $0 < \alpha < 1$,

$$-i \left(\frac{d\Lambda_{ET}}{dk} \right)_{k=0} = \begin{cases} \infty & \lambda = 0 \\ V_* & \lambda > 0 \end{cases} \tag{2.60}$$

That is, without tempering, the current is not well-defined for $\alpha < 1$ due to the divergence of the first moment of Lévy distributions. This issue motivated the alternative characterization of the ratchet current in [DGS08]. However, the truncation regularizes this term and gives rise to a finite contribution to the current

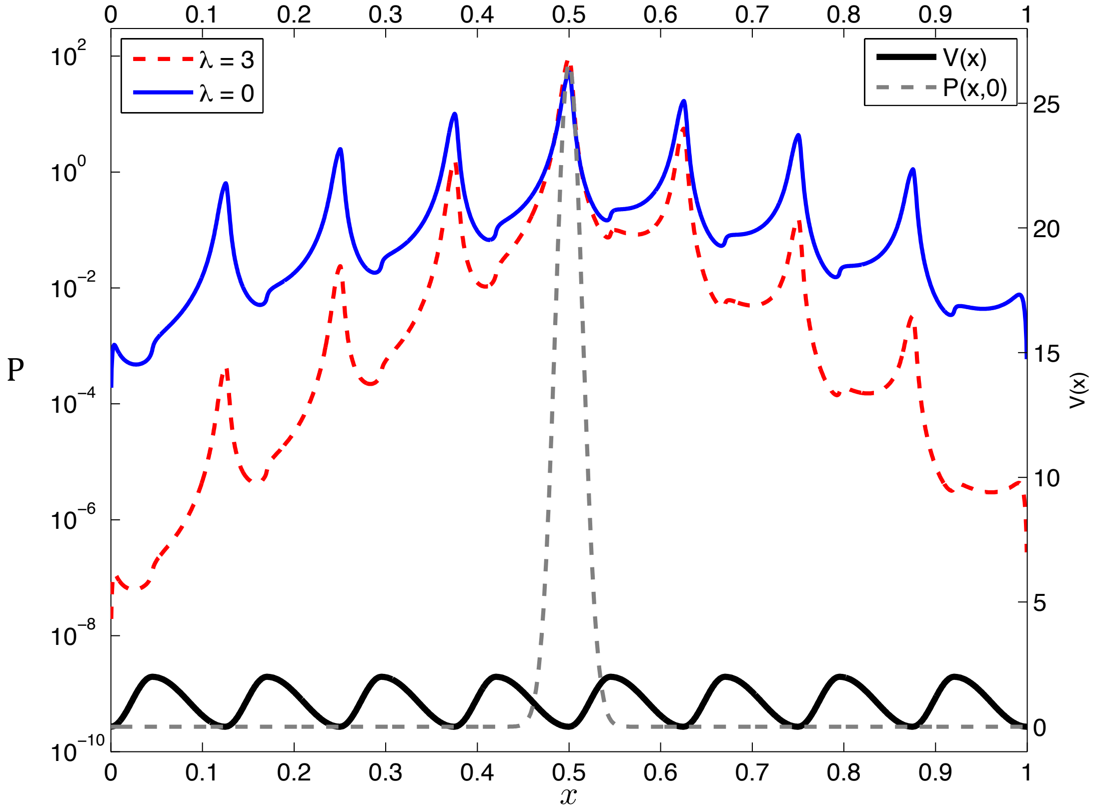

Figure 2.4: Time-dependent solutions of the TFFP-equation (2.34) for $\lambda = 0$ and $\lambda = 3$, with $\alpha = 1.5$, $\theta = 0$, $V_0 = 1$ and $\chi_\alpha = 0.5$. Both solutions are found from the initial condition (2.57) for the same final time. The solid line at the bottom is the potential in linear-linear scale. The PDFs for $\lambda = 0$ and $\lambda = 3$ are shown in a log-linear scale.

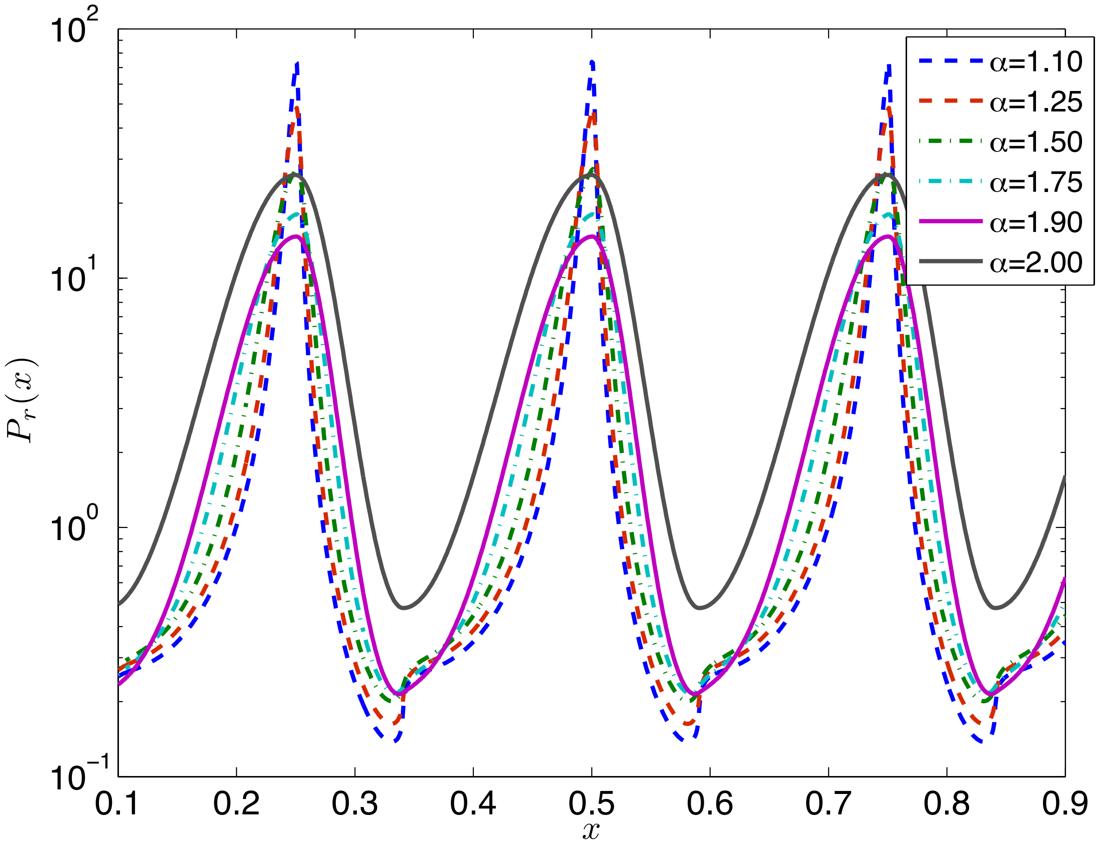

Figure 2.5: Dependence on α of the steady-state solutions of the fractional Fokker–Planck equation with the periodic potential in equation (2.51). The plot shows the PDFs in a periodic domain for different values of α, and $\lambda = 0$, $\theta = 0$, $V_0 = 1$, $A = -0.274$, and $\chi_\alpha = 0.5$.

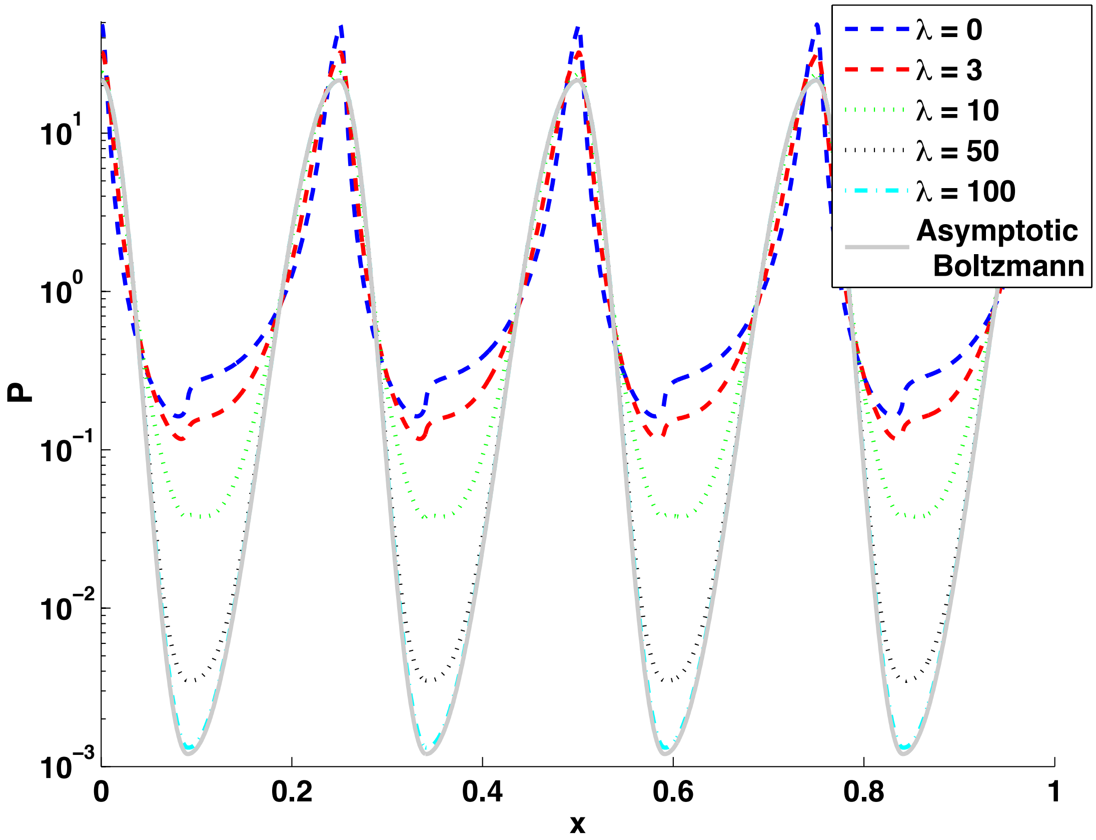

Figure 2.6: Dependence on λ of the steady-state solution of the TFFP equation (2.35) with the periodic potential in equation (2.51). The plot shows the PDFs in a periodic domain for different values of λ, and $\alpha = 1.25$, $\theta = 0$, $V_0 = 1$, $A = -0.274$, and $\chi_\alpha = \chi_0\,\lambda^{2-\alpha}$ with $\chi_0 = 0.5$. The solid line denotes the corresponding Boltzmann distribution.

equal to V_* in equation (2.12) that, as expected, corresponds to the mean drift in equation (2.33) and to the first moment of the jump distribution in equation (2.10) and the first moment of Green's function in equation (2.17).

The computation of the second term on the right-hand side of equation (2.59) follows directly from equation (2.54) and leads to

$$J = - \sum_{n=-\infty}^{\infty} c_n \hat{P}_n - i \left(\frac{d\Lambda_{ET}}{dk} \right)_{k=0} . \tag{2.61}$$

Figure 2.7 shows the dependence of the current on the value of α for different levels of tempering. In agreement with the results reported in [CGC08], in the absence of tempering $\lambda = 0$, a net current is observed for $\alpha < 2$ with a maximum around $\alpha \approx 1.4$. Most importantly, as the figure shows, a finite (albeit smaller) current remains for $\lambda > 0$. That is, in the presence of a ratchet potential, a net non-equilibrium current persists in the steady-state asymptotic regime. Regardless of the value of λ, in the limit $\alpha = 2$, the current vanishes. It is observed that as truncation increases, the value of α for which the maximum current is attained shifts to the right, and for large values of λ, the strength of the current exhibits only a weak dependence on α. Figure 2.8 plots $\delta J(t) = J(t) - J(\infty)$ as a function of time to show the rate of convergence to the steady-state asymptotic current. An exponential convergence of the form

$$\delta J \sim \exp\left(-\gamma_\tau t\right) , \tag{2.62}$$

is observed, and as shown in table 2.1, the decay rate γ_τ exhibits a very weak dependence on the value of α and λ. In all the numerical results, the current has been been reported in units of L/τ where $\tau = L^\alpha / \chi_\alpha$ is the fractional diffusion time scale.

As the previous calculations show, as λ increases, the current is reduced, and a problem of significant interest is to find the rate of decay of the current in the asymptotic limit $\lambda \to \infty$. As shown in figures 2.9-2.11, depending on the value of α, two asymptotic regimes are observed. For α near the diffusion value $\alpha = 2$, the current exhibits an algebraic decay for large λ of the form

$$J \sim \lambda^{-\zeta}, \tag{2.63}$$

where $\zeta \approx 2.5$ for $\alpha = 1.9$ and $\zeta \approx 6$ for $\alpha = 1.75$. This slow algebraic scaling breaks down as α is reduced from the diffusion value. In particular, as shown in figure 2.10, for $1 < \alpha < 1.5$, the current decays exponentially fast:

$$J \sim \exp\left(-\zeta\lambda\right), \tag{2.64}$$

with $\zeta \approx 0.40$. As verified in figure 2.11, the same scaling is observed for $\alpha < 1$.

Figure 2.12 shows the dependence of the current J on the potential asymmetry A. In all cases, the current vanishes when the potential is symmetric $A = 0$. Consistent with the results reported in [CGC08], the curve $\lambda = 0$, which corresponds to an α-stable Lévy ratchet, shows the existence of a ratchet current in the direction of the steepest side of the potential. An important conclusion of this study is that, even in the presence of truncation, a ratchet current is observed and its dependence on A is qualitatively similar to the α-stable case.

To elicit the dependence of the current on an external tilting force, the current is also computed for an effective potential of $V_{eff} = V(x) - Fx$, where $V(x)$ is the ratchet potential in equation (2.51), and F is constant. As shown in figure 2.13, the $\lambda = 0$ case recovers the α-stable Lévy ratchet results, and as λ increases, the strength of the current decreases. Note that the value of the stopping force, $F \approx -1$, or the force needed to cancel the ratchet current, seems to be independent of λ.

An interesting effect of the truncation is observed when the truncated fractional diffusion operator is asymmetric, i.e., when the weighting factors l and r of the left and right fractional derivatives in equation (2.3) are different. As shown in figure 2.14, in the absence of truncation, $\lambda = 0$, the current can be reversed by

α	1.25	1.25	1.25	1.5	1.5	1.5	1.75	1.75	1.75
λ	0	10	30	0	10	30	0	10	30
γ_τ	64	58	58	60	57	58	52	51	53

Table 2.1: Dependence of exponential decay rate γ_τ of transient current in equation (2.62) as a function of α and λ for $\theta = 0$, $A = -0.274$, $V_0 = 1$, and $\chi_\alpha = 0.5$. Case $\alpha = 1.5$, $\lambda = 10$ is shown in figure 2.8.

biasing the asymmetry. In particular, for the case shown, increasing θ to a large enough value stops the positive current. As the value of θ is further increased, a negative current eventually appears. A similar phenomenology is observed when the truncation is present, except that (in addition to the usual overall decrease of the magnitude of the current) the critical value of θ for current reversal increases. The fact that the critical θ for current reversal depends on λ implies that for a range of θ values it is possible to reverse the current by changing λ only. This interesting feature of truncated Lévy ratchets is clearly illustrated in figure 2.15, where it is shown that for $\theta = 0.275$ the truncation can in fact lead to a current reversal. Consistent with the fact that for $\lambda = 0$ and $\theta = 0.180$, the current vanishes (see figure 2.14), the current in figure 2.15 for $\theta = 0.180$ is always positive and vanishes for $\lambda = 0$ and for large λ. A further increase of the asymmetry to $\theta = 0.275$ gives rise to the vanishing of the current for $\lambda \approx 1/3$. For successively larger values of θ, the value of λ for which the current reverses increases. To conclude the numerical simulations of the steady-state current, figure 2.16 shows the dependence of the current on $\sigma = \chi_\alpha^{1/\alpha}$, where χ_α is the diffusivity. In the absence of truncation, the current is maximum for $\sigma \sim 1$. However, as the truncation increases, the value of the diffusivity for which the maximum current is attained increases.

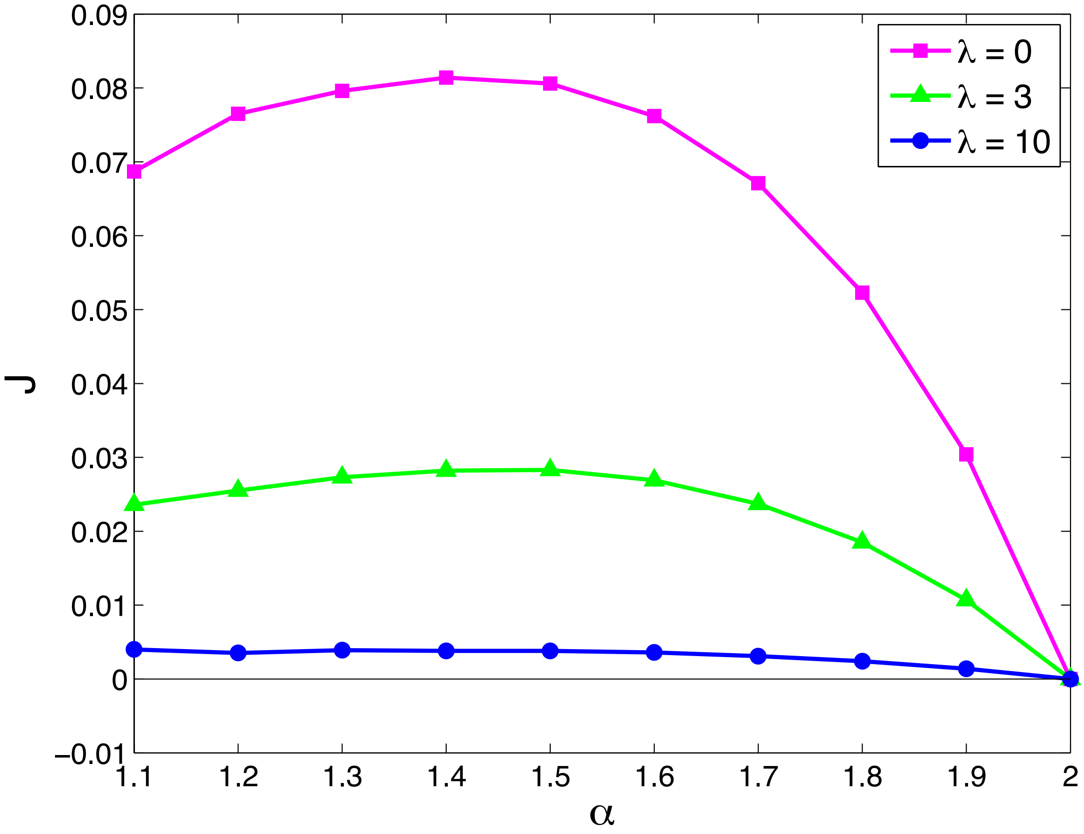

Figure 2.7: Ratchet current J as a function of α for different levels of truncation λ, with $\theta = 0$, $A = -0.6$, $V_0 = 1$, and $\chi_\alpha = 0.5$.

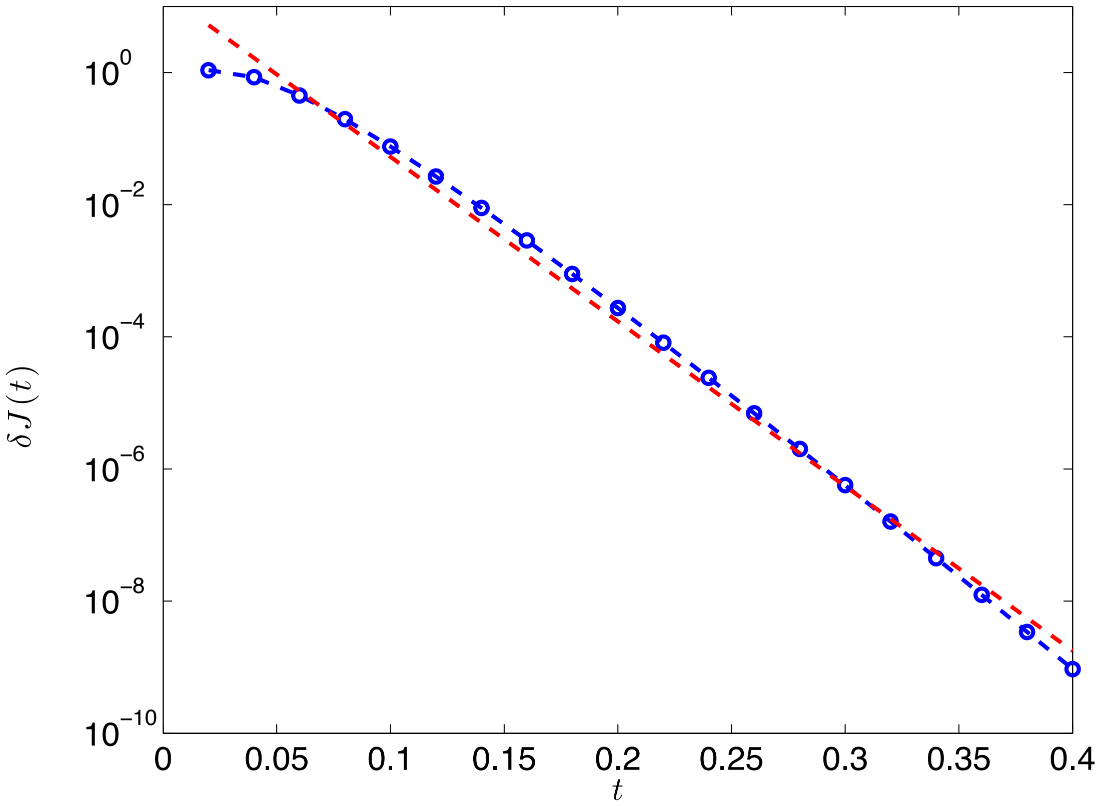

Figure 2.8: Exponential convergence of ratchet current as a function of time. The plot shows $\delta J = J(\infty) - J(t)$, where $J(\infty)$ is the steady-state asymptotic current (obtained from the solution of equation (2.56)) and $J(t)$ is the time-dependent transient current (obtained from the solution of equation (2.55)). The parameter values are $\alpha = 1.5$, $\lambda = 10$, $\theta = 0$, $A = -0.274$, $V_0 = 1$, and $\chi_\alpha = 0.5$. The dashed line is an exponential fit of the form $\delta J \sim \exp(-\gamma_\tau t)$ with $\gamma_\tau \sim 57$. Table 2.1 shows the exponential decay rate for different values of α and λ.

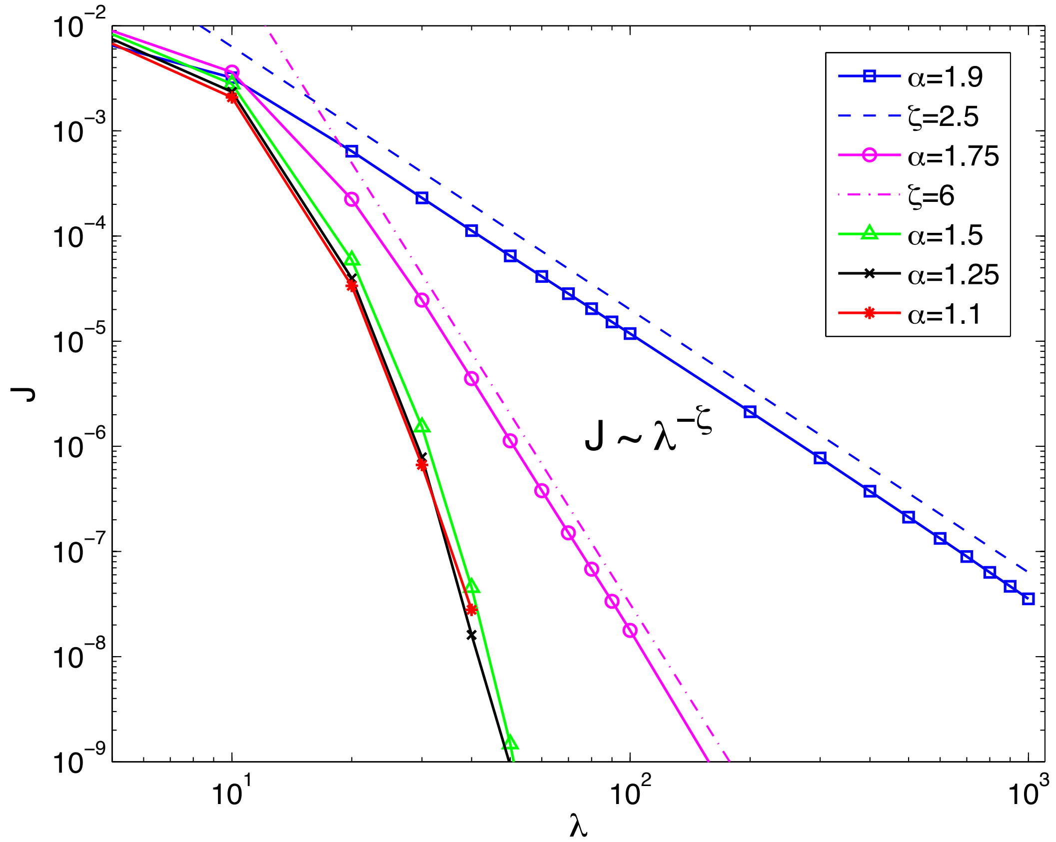

Figure 2.9: Decay of ratchet current J as a function λ for different values of α and $\theta = 0$, $V_0 = 1$, and $A = -0.274$. The log-log scale shows evidence of algebraic decay for $\alpha \geq 1.75$.

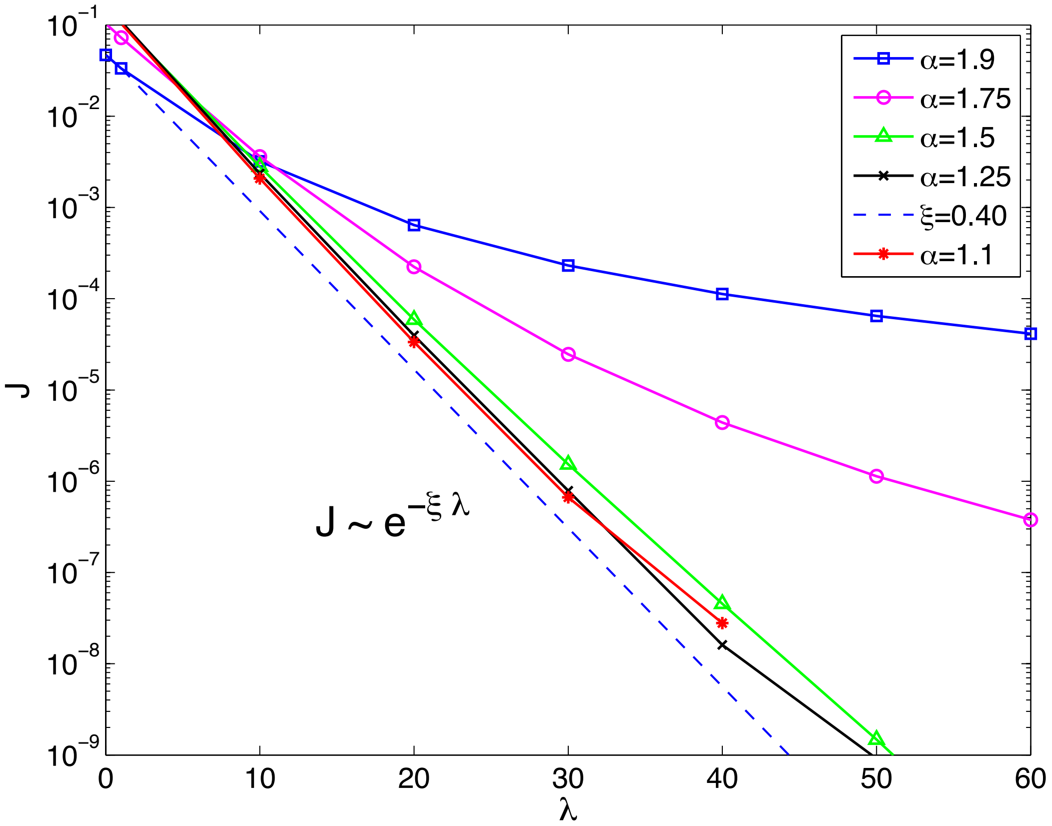

Figure 2.10: Decay of ratchet current J as a function λ for different values of α and $\theta = 0$, $V_0 = 1$, and $A = -0.274$. The log-linear scale shows the evidence of exponential decay for $\alpha \leq 1.5$.

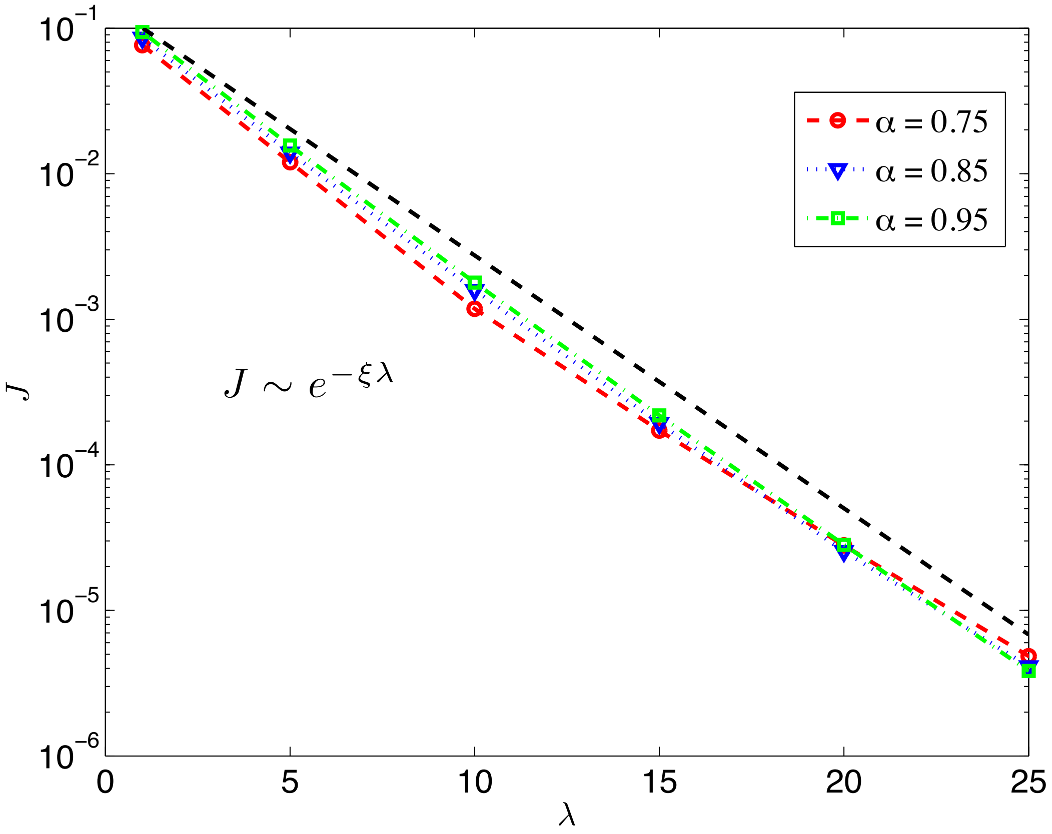

Figure 2.11: The same as figure 2.10 but for $\alpha < 1$.

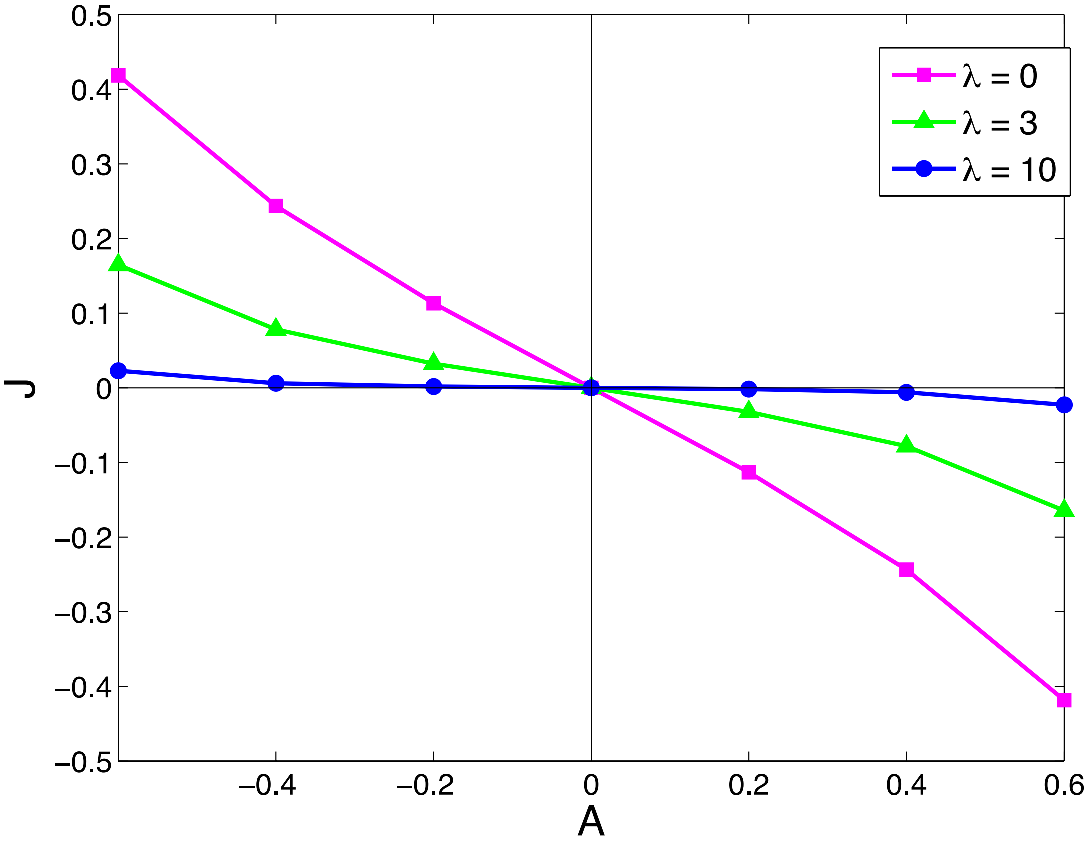

Figure 2.12: Ratchet current J as a function of ratchet potential symmetry A for different levels of truncation λ, with $\alpha = 1.5$, $\theta = 0$, $V_0 = 1$, and $\chi_\alpha = 0.5$.

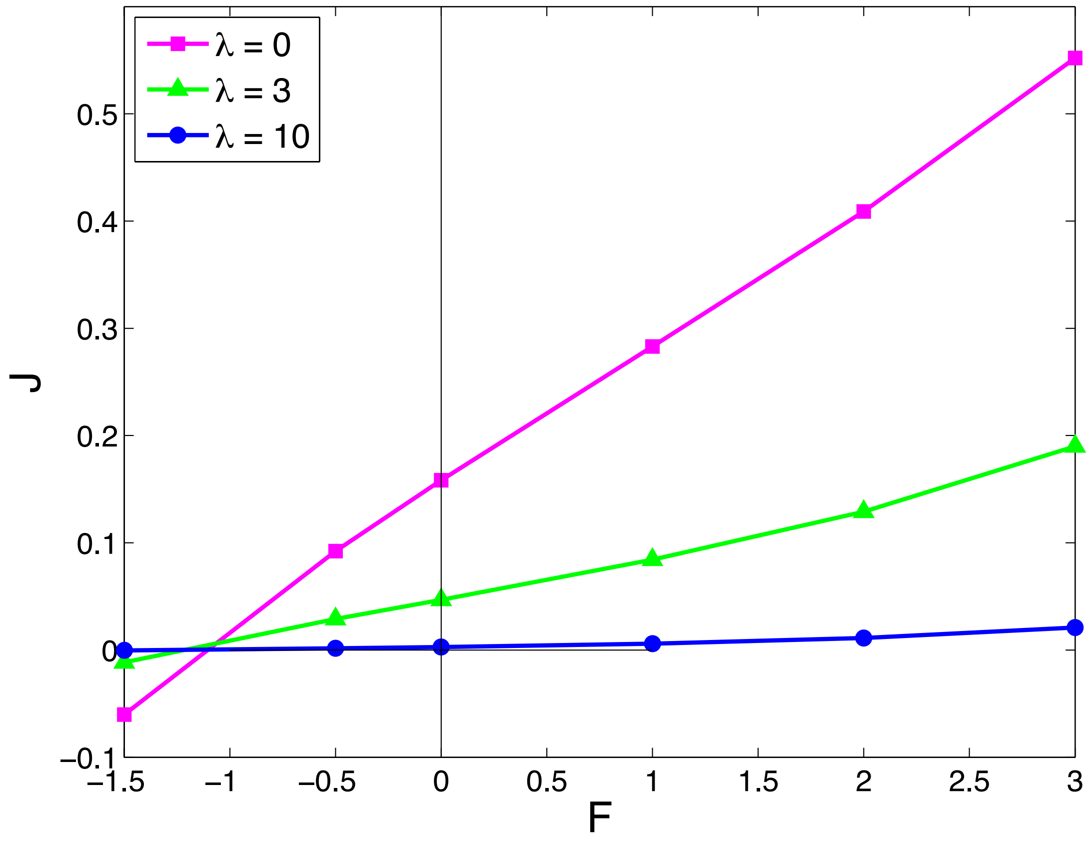

Figure 2.13: Ratchet current J as a function of external force F for different levels of truncation λ, with $\alpha = 1.5$, $\theta = 0$, $V_0 = 1$, $A = -0.274$, and $\chi_\alpha = 0.5$.

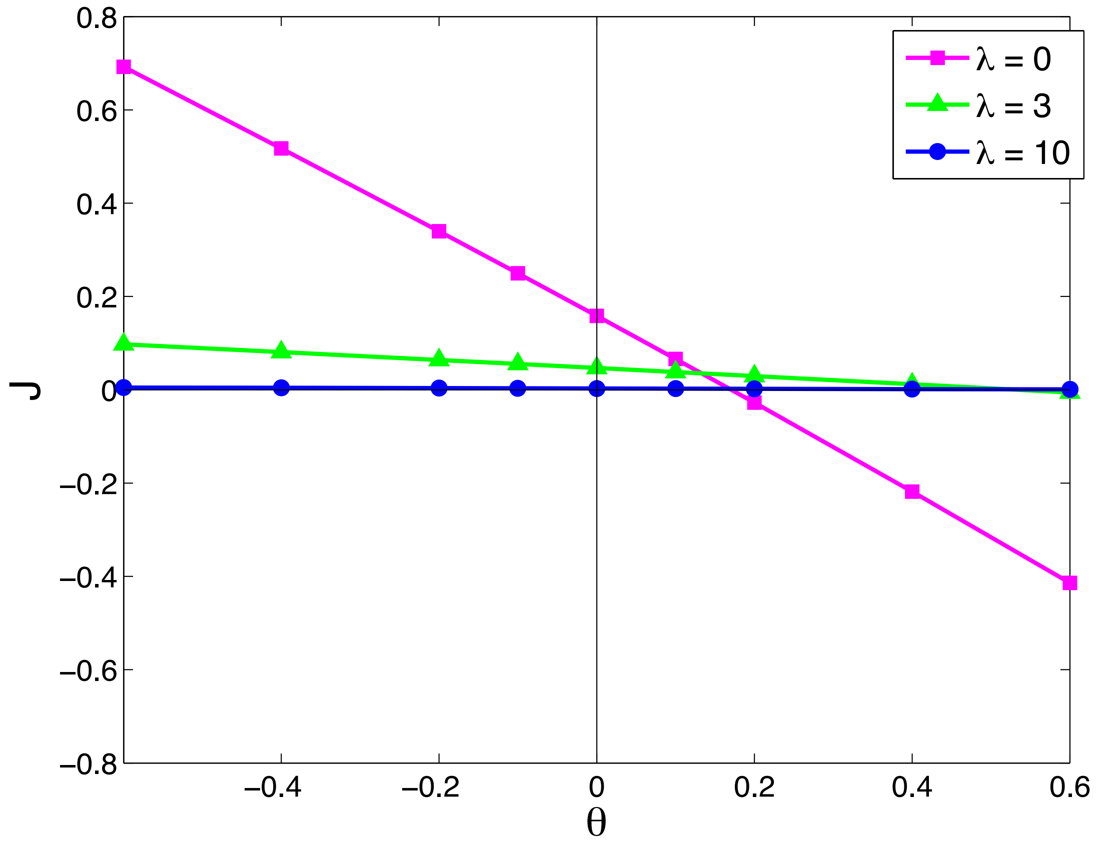

Figure 2.14: Ratchet current, J, as function of fractional diffusion asymmetry θ for different levels of truncation λ, with $\alpha = 1.5$, $V_0 = 1$, $A = -0.274$, and $\chi_\alpha = 0.5$.

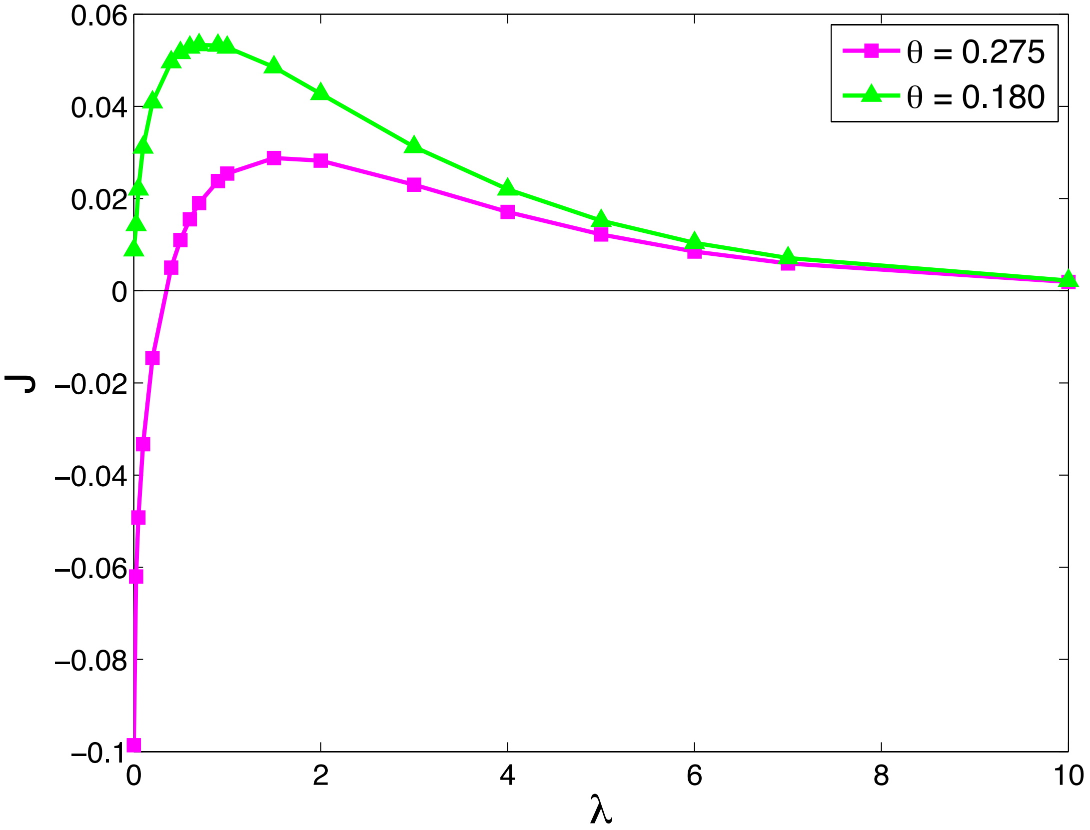

Figure 2.15: Ratchet current J as a function of truncation parameter λ for different levels of fractional diffusion asymmetry θ, $\alpha = 1.5$, $V_0 = 1$, $A = -0.274$, and $\chi_\alpha = 0.5$. For $\theta = 0.275$, the current is reversed for $\lambda \approx 1/3$.

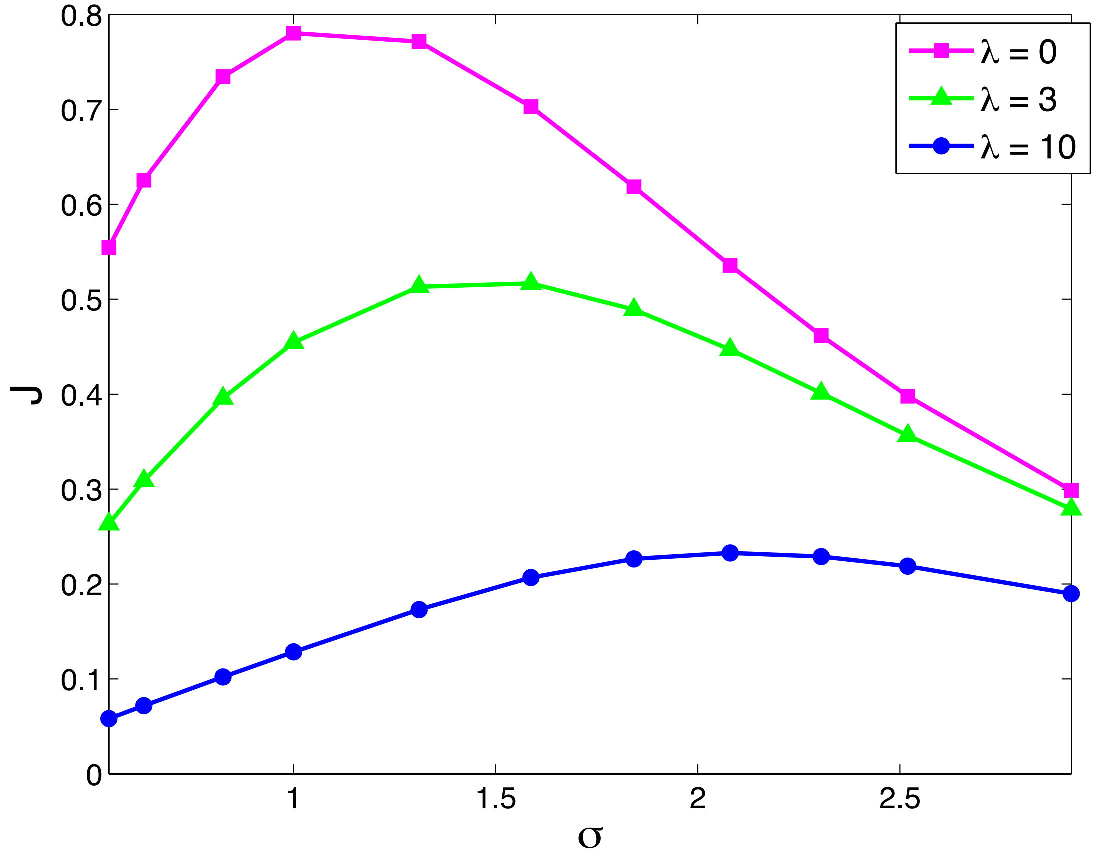

Figure 2.16: Ratchet current J as a function of $\sigma = \chi_\alpha^{1/\alpha}$ for different levels of truncation λ, with increase, the value of the diffusivity for which the maximum current is attained increases.

2.5 Conclusions

The incorporation of tempering in models of anomalous transport due to Lévy flights is motivated by the fact that in problems of practical interest, the moments of the PDFs represent physical quantities that cannot be unbounded. For example, although anomalously large displacements have been well documented in numerical simulations of turbulent transport and in fluid mechanics experiments, it is clear from the physical point of view that particle displacements cannot be arbitrarily large and that a cut-off or truncation has to be incorporated in the PDFs describing these processes. This was the intuition behind the original proposal of truncated Lévy flight in [MS94] and the main motivation for the construction of spatially tempered FD operators in [CC07]. In this chapter, the effects of spatial tempering on super-diffusive transport is studied in the presence of an external potential. This study is based on the spatially tempered FFP equation which is obtained by replacing the diffusion term in the standard Fokker-Planck equation with a tempered fractional diffusion operator.

The parameter study presented in this chapter focuses on harmonic potentials and periodic potentials with broken spatial symmetry. In the case of harmonic potentials, perturbative analytic solutions are constructed in the limit of large truncation, i.e. $\lambda >> 1$. Also steady-state solutions are numerically computed, showing that the PDFs approach the Boltzmann distribution in the limit of large λ. In the study of periodic potentials, two complementary numerical methods are used. For the computation of the space-time evolution of the PDF in a finite-size computational domain, a finite-difference method is used which is based on the Grunwald-Letnikov discretization of the truncate fractional derivatives regularized in space. For the computation of the PDF in a periodic domain as well as the time-dependent and asymptotic steady-state current, a Fourier-based spectral method is used. The main object of study is the dependence of the steady-state current on the level of truncation λ, the stability index α and the asymmetry θ, as well as the asymmetry of the potential. The general conclusion is that in most parameter regimes the inclusion of truncation does not change the qualitative dependencies of the current on the different system parameters; instead, the effect of truncation is mainly to decrease the magnitude of current. As expected, in the limit $\lambda \to \infty$, the PDFs converge to the Boltzmann distribution and the current vanishes. An interesting situation occurs when there is an asymmetry on the truncated fractional diffusion operator, i.e. for $\theta \neq 0$. In this case, truncation can lead to a reversal of the current direction. The current is observed to converge exponentially in time to the steady-state value, and the decay rate exhibits only a weak dependence on α and λ. The decay of the current for increasing values of λ exhibits different scaling properties depending on the value of α. For large values of α, $1.75 \leq \alpha$, the current exhibits an algebraic decay and for small values, $\alpha \leq 1.5$, the current exhibits an exponential decay.

CHAPTER 3

Isotropic model of fractional transport in two-dimensional bounded domains

3.1 Introduction

Previous applications of fractional models to transport situations relevant to fusion plasmas have been based on one dimensional Cartesian fractional derivative operators. A summary of this approach, for instance, can be found in Ref. [Cas08] (see references therein as well). Although the 1D model can produce theoretical results that are in relative agreement with perturbative transport experiments[CMN08], there are several deficiencies associated with using a purely 1D formulation to model radial transport in a two dimensional domain. One important limitation is the need for an ad hoc spatially-dependent fractional diffusivity that must go to zero at the origin in order to keep the heat flux at that point equal to zero[Cas06]. Forcing the diffusivity to drop to zero creates a fractional transport barrier at the origin that may not be physical and that can have a significant effect on the predicted transport in the core. This condition on the diffusivity is needed, because the boundary condition $\partial_x T(0) = 0$ does not in general lead to a zero fractional flux when 1D Cartesian operators are used. More generally, the 1D Cartesian operator also cannot correctly include, near the origin, all the geometric effects of a 2D circular system.

Although radial transport is the more important contribution in determining the confinement properties of a fusion plasma, it should also be noted that 1D operators cannot be applied to the polodial component of transport when the total transport in the system is isotropic (cf. discussion in section 3.2). That is, any sum of 1D operators (e.g., one for transport in the x-direction and one for the y-direction) describes a 2D *non-isotropic* transport process that implicitly depends on the directions of the x, y-axes.

In light of the limitations associated with 1D fractional operators, one objective of this Chapter is to derive a 2D isotropic fractional derivative operator, referred to as the *fractional Laplacian.* When expressed in polar geometry, this fractional Laplacian can be expanded into a Fourier series in the θ-direction. For each mode n, this expansion gives an integro-differential equation in r, with kernels that are parametrized by n. The $n = 0$ equation corresponds to an azimuthally-averaged radial fractional transport model that naturally incorporates near-origin geometric effects and produces a zero flux at the origin when $\partial_x T(0) = 0$. The study and application of this $n = 0$ radial fractional model is another objective of this Chapter.

In an unbounded domain, the 2D fractional diffusion equation can be derived as a macroscopic description of a continuous time random walk (CTRW). The CTRW model describes the random excursion of an ensemble of representative elements by allowing arbitrary jump, and waiting, probability distributions. A key assumption in the present derivation is that the underlying stochastic process associated with the CTRW is without a characteristic length-scale, i.e., it is scale-free. This means that the underlying probability distribution function (PDF) has infinite second and higher moments, i.e., $\langle x^2 \rangle$ diverges.

Although the fractional diffusion model for an unbounded domain can be derived in a straightforward manner from a CTRW model, there is no direct method for applying the unbounded domain fractional Laplacian to a bounded domain. One practical difficulty lies in the appearance of singular terms that depend on the truncation of the range of integration in the non-local integro-differential fractional

Laplacian. One objective of this Chapter is to develop a plausible, and well-posed, bounded domain model for the $n = 0$ radial fractional derivative operator.

Finally, this Chapter is organized as follows. The isotropic, 2D model is developed in Sec. 3.2. Section 3.3 examines applications of the bounded domain model including: steady-state calculations with and without sources, comparison to the Cartesian model, anomalous scaling of the confinement time, the propagation of cold pulses, and fractional thermal waves. Technical details, including a numerical method that solves the radial fractional diffusion equation, are discussed in the appendices A and B.

3.2 2D Model

3.2.1 Isotropic CTRW and fractional diffusion limit in 2D unbounded domains.

Fractional diffusion models are closely connected to continuous time random walk (CTRW) models that are characterized by infinite second moments and anomalously large displacements, or Lévy flights. In particular, fractional diffusion equations in 1D can be derived as macroscopic descriptions of these types of non-Brownian random walks by taking a fluid limit of the kinetic master equation associated with the CTRW. In this section, a 2D model is derived based on these concepts, as a way of obtaining a physically plausible model of fractional diffusion. The derivation results in an operator that is well-defined in the unbounded domain.

In the separable CTRW model, the random displacement of a group of representative elements is described by two suitably chosen PDFs: $\eta(\Delta\vec{x})$, the jump PDF and $\psi(\Delta t)$, the waiting time PDF. The product of these functions, $\eta(\Delta\vec{x})\,\psi(\Delta t)$, gives the probability that an element at a position $\vec{x}$ and at time t is displaced to position $\vec{x}+\Delta\vec{x}$ at time $t+\Delta t$. This work only considers Markovian and isotropic CTRWs which correspond, respectively, to making $\psi(\Delta t)$ a Poisson distribution and to assuming that $\eta(\Delta\vec{x}) = \eta(|\Delta\vec{x}|)$, i.e., the jump distribution only depends on the size of the jump and not on the direction of the jump. Under these assumptions, the time evolution of the probability density $P(\vec{x},t)$ is governed by the master equation

$$\frac{\partial}{\partial t}P(\vec{x},t) = \frac{1}{\tau}\int\int \eta(|\vec{x}-\vec{x}'|)\, P(\vec{x}',t)\,\mathrm{d}\vec{x}' - \frac{P(\vec{x},t)}{\tau} \quad , \tag{3.1}$$

where τ is the average waiting time between jumps. As it is written, the master equation (3.1) gives a complete description of an arbitrary isotropic transport process in terms of an unspecified PDF, η. For (3.1) to describe a fractional diffusion process, it is assumed that the second moments of η are infinite. Equivalently, it is assumed that the tails of η are algebraically decaying, i.e.

$$\eta(|\vec{x}|) \sim \frac{1}{|\vec{x}|^{\alpha+2}} \quad , \tag{3.2}$$

where α ranges between $1 < \alpha < 2$.

The fluid-like continuum limit of (3.1) is achieved by introducing a small scale factor ϵ into η, e.g.,

$$\eta(\vec{x}) \to \frac{1}{\epsilon^2}\,\eta\left(\vec{x}/\epsilon\right) \quad , \tag{3.3}$$

and then taking the distinguished limit $\epsilon \to 0$ and $\tau \to 0$ while holding ϵ^α/τ constant. Note that α is part of the exponent in (3.2) and that α is the order of the fractional derivative. The continuum limit can be taken in Fourier space, where equation (3.1) becomes,

$$\frac{\partial}{\partial t}\,\hat{P}(\vec{k},t) = \frac{1}{\tau}\left[\hat{\eta}(\epsilon|\vec{k}|) - 1\right]\,\hat{P}(\vec{k},t)\ . \tag{3.4}$$

Thus the fluid limit is equivalent to expanding the Fourier transform $\hat{\eta}$ for small wave numbers k or large wavelengths (i.e., at scale lengths pertinent to the tail regions of the probability density). When η has tails of the form (3.2), the leading order term of $\hat{\eta}(\epsilon|\vec{k}|) - 1$ in the limit $\epsilon \to 0$ is as follows (cf. appendix A.1)

$$\hat{\eta}(\epsilon\,|\vec{k}|) - 1 = -\tau\,\chi_\alpha\,|\vec{k}|^\alpha \quad , \tag{3.5}$$

where $\chi_\alpha \propto \epsilon^\alpha/\tau$ is the *fractional diffusivity* and it is assumed constant as $\epsilon, \tau \to 0$. *Expression* (3.5) *is the Fourier transform of the 2D fractional Laplacian.* To perform the inverse Fourier transform and obtain the fractional Laplacian in configuration space, the $|\vec{k}|^\alpha$ term is written as

$$-\chi_\alpha\,|\vec{k}|^\alpha\,\hat{P}(\vec{k},t) = -\chi_\alpha\,|\vec{k}|^2\,\left(|\vec{k}|^{\alpha-2}\,\hat{P}(\vec{k},t)\right) \quad , \tag{3.6}$$

and the convolution theorem for Fourier transforms is applied with $|\vec{k}|^{\alpha-2}$ as one of the convolved functions. Note (cf. appendix A.2) that

$$\mathcal{F}^{-1}\left\{|\vec{k}|^{\alpha-2}\right\} = \frac{1}{\gamma_\alpha}\,\frac{1}{|\vec{x}|^\alpha} \quad , \tag{3.7}$$

and

$$\gamma_\alpha = \pi\,2^{2-\alpha}\,\frac{\Gamma\left(1-\frac{1}{2}\alpha\right)}{\Gamma\left(\frac{1}{2}\alpha\right)} \quad . \tag{3.8}$$

There are two equivalent ways of applying the convolution theorem

$$\begin{aligned} -|\vec{k}|^\alpha\,\hat{P}(\vec{k},t) &= -|\vec{k}|^2\,\left(|\vec{k}|^{\alpha-2}\,\hat{P}(\vec{k},t)\right) = -|\vec{k}|^2\,\mathcal{F}\left\{\frac{1}{\gamma_\alpha}\,\frac{1}{|\vec{x}|^\alpha} * P(\vec{x},t)\right\} \\ &= |\vec{k}|^{\alpha-2}\,\left(-|\vec{k}|^2\,\hat{P}(\vec{k},t)\right) = \mathcal{F}\left\{\frac{1}{\gamma_\alpha}\,\frac{1}{|\vec{x}|^\alpha} * [\Delta P(\vec{x},t)]\right\} \quad , \end{aligned} \tag{3.9}$$

where the *star* operator indicates convolution. The difference between the two forms is in the location of the Laplacian operator due to the $-|\vec{k}|^2$ factor; in the first it appears outside the convolution integral, and in the second on the inside of the integral. Thus, the inverse transform of (3.4) with (3.5) is

$$\begin{aligned} \frac{\partial}{\partial t}P(\vec{x},t) &= \chi_\alpha \int\!\!\int_{R^2} \frac{1}{\gamma_\alpha}\,\frac{\Delta'\,P(\vec{x}',t)}{|\vec{x}-\vec{x}'|^\alpha}\,\mathrm{d}\vec{x}' \qquad \text{(or)} \\ &= \chi_\alpha\,\Delta \int\!\!\int_{R^2} \frac{1}{\gamma_\alpha}\,\frac{P(\vec{x}',t)}{|\vec{x}-\vec{x}'|^\alpha}\,\mathrm{d}\vec{x}' \quad , \end{aligned} \tag{3.10}$$

where Δ is the conventional Laplacian derivative operator and the range of the integration is R^2 or over the entire plane. In the unbounded domain, both expressions in equation (3.10) are equivalent. Defining the fractional Laplacian $\Delta^{\alpha/2}$ in an unbounded domain as follows,

$$\Delta^{\alpha/2}\, P(\vec{x}) \equiv \Delta \int\!\!\int_{R^2} \frac{1}{\gamma_\alpha} \frac{P(\vec{x}',t)}{|\vec{x}-\vec{x}'|^\alpha}\, \mathrm{d}\vec{x}' \quad , \tag{3.11}$$

the fractional diffusion equation (3.10) becomes

$$\frac{\partial}{\partial t} P(\vec{x},t) = \chi_\alpha\, \Delta^{\alpha/2}\, P(\vec{x},t) \ . \tag{3.12}$$

When this equation is expressed in the form of a continuity equation,

$$\frac{\partial}{\partial t} P + \nabla \cdot \vec{q} = 0 \quad , \tag{3.13}$$

the corresponding fractional flux is

$$\vec{q} \equiv -\chi_\alpha \nabla \int\!\!\int_{R^2} \frac{1}{\gamma_\alpha} \frac{P(\vec{x}',t)}{|\vec{x}-\vec{x}'|^\alpha}\, \mathrm{d}\vec{x}' \ . \tag{3.14}$$

3.2.2 Isotropic fractional diffusion in 2D unbounded cylindrical domains

In systems with cylindrical geometry it is possible to expand the fractional Laplacian given in equation (3.11) into a Fourier series in the variable θ. This expansion gives a set of integro-differential equations for each poloidal mode n, with kernels that are parametrized by n. In this section, this poloidal Fourier expansion is obtained and the proper treatment of the boundary conditions at the origin is developed for the $n = 0$ mode. Later sections focus on the study of the $n = 0$ radial fractional equation developed here.

In polar coordinates, the unbounded domain fractional Laplacian takes the form

$$\begin{aligned}\Delta^{\alpha/2}\, P(r,\theta) = &\left[\frac{1}{r}\frac{\partial}{\partial r}\left(r\frac{\partial}{\partial r}\right) + \frac{1}{r^2}\frac{\partial^2}{\partial \theta^2}\right] \\ &\int_0^\infty r'\mathrm{d}r' \int_0^{2\pi} \mathrm{d}\theta' \, \frac{P(r',\theta')}{\gamma_\alpha\, \left(r^2 + r'^2 - 2rr'\cos(\theta-\theta')\right)^{\alpha/2}} \ .\end{aligned} \tag{3.15}$$

When $P(r,\theta)$ is expanded into a poloidal Fourier series,

$$P(r,\theta) = \sum_{n=-\infty}^{\infty} P_n(r)\, \exp(in\theta) \ , \tag{3.16}$$

the expansion (3.16) can be substituted into (3.15) so that, after the change of variables $z = \theta' - \theta$, the following is obtained

$$\Delta^{\alpha/2}\, P = \frac{\Delta}{\gamma_\alpha} \sum_{n=-\infty}^{\infty} \exp(in\theta) \int_0^\infty r'\mathrm{d}r' \int_0^{2\pi} \mathrm{d}z \frac{P_n(r')\exp(inz)}{[r^2 + r'^2 - 2rr'\cos(z)]^{\alpha/2}} \ . \tag{3.17}$$

The integration in z can be done analytically[GR80] to give the following poloidal expansion of the fractional Laplacian:

$$\Delta^{\alpha/2}\, P(r,\theta) = \sum_{n=-\infty}^{\infty} \exp(in\theta) \left[\frac{1}{r}\frac{\partial}{\partial r} r \frac{\partial}{\partial r} - \frac{n^2}{r^2}\right] \int_0^\infty r'\mathrm{d}r'\, K_\alpha^{(n)}(r,r')\, P_n(r') \ , \tag{3.18}$$

where the kernel $K_\alpha^{(n)}(r,r')$ is given by, for all n,

$$K_\alpha^{(n)}(r,r') = \frac{2\pi}{\gamma_\alpha} \frac{1}{|n|\, B(\alpha/2, |n|)} \frac{1}{r_>^\alpha} \left(\frac{r_<}{r_>}\right)^{|n|} {}_2F_1\left(\frac{\alpha}{2}, \frac{\alpha}{2} + |n|; |n| + 1; \left(\frac{r_<}{r_>}\right)^2\right) \ . \tag{3.19}$$

In the kernel (3.19), $B(x,y)$ is the beta function, ${}_2F_1(a,b;c;z)$ is Gauss' hypergeometric function[AS72] and $r_< = \min\{r,r'\}$ and $r_> = \max\{r,r'\}$.

Equation (3.18) allows for the 2D fractional diffusion equation (3.12) to be solved in cylindrical geometry; solutions can be found by solving the poloidal mode fractional diffusion equation

$$\frac{\partial}{\partial t} P_n(r,t) = \chi_\alpha \left[\frac{1}{r}\frac{\partial}{\partial r} r \frac{\partial}{\partial r} - \frac{n^2}{r^2}\right] \int_0^\infty r'\mathrm{d}r'\, K_\alpha^{(n)}(r,r')\, P_n(r') \ , \tag{3.20}$$

for each P_n and then summing according to (3.16). Although each n mode is governed by an integral equation with a different kernel, in practice this method is much easier to implement than directly solving the two dimensional integral equation in (3.12).

When $n = 0$, a radial fractional diffusion operator is obtained that describes the transport of the poloidally averaged profile (i.e., $P_0(r) = \langle P(r,\theta)\rangle_\theta$). In this case the average scalar profile $P_0(r)$ obeys the transport equation

$$\frac{\partial}{\partial t} P_0(r,t) = \chi_\alpha\, \Delta_r^{\alpha/2}\, P_0(r,t) \ , \tag{3.21}$$

where

$$\Delta_r^{\alpha/2} P(r) = \frac{1}{r}\frac{\partial}{\partial r} r \frac{\partial}{\partial r} \int_0^{\infty} r' \mathrm{d}r' \, K_\alpha^{(0)}(r,r') \, P(r') \ . \tag{3.22}$$

Note that the zeroth order kernel $K_\alpha^{(0)}(r,r')$ reduces to

$$K_\alpha^{(0)}(r,r') = \frac{2\pi}{\gamma_\alpha} \frac{1}{r_>^\alpha} \, {}_2F_1 \left[\frac{\alpha}{2}, \frac{\alpha}{2}; 1; \left(\frac{r_<}{r_>} \right)^2 \right] \ , \tag{3.23}$$

since $\lim_{n\to 0} \ |n| \, B(\alpha/2, |n|) = 1$.

In order for equation (3.21) to remain finite at the origin, the corresponding radial fractional flux must go to zero there at least as fast as $q \sim r$. This requirement is general to polar geometry, and is needed to remove the $1/r$ singularity that appears in the polar form of the divergence operator. The radial fractional non-local flux corresponding to the $n = 0$ transport equation (3.21) can be written as

$$q_0(r) = -\chi_\alpha \frac{\partial}{\partial r} \int_0^{\infty} \mathrm{d}r' \ r' K_\alpha^{(0)}(r,r') \, P_0(r') \ . \tag{3.24}$$

For small r, this flux is governed by an asymptotic series with the following dependence on the derivatives at the origin

$$q_0(r) = \sum_{m=1}^{\infty} \ P_0^{(m)}(0) \, A_m \, r^{m+1-\alpha} + \sum_{m=1}^{\infty} \ B_m \, r^{2m-1} \ . \tag{3.25}$$

The coefficients A_m and B_m, given by equation (A.28) in appendix A.3, are constants with respect to r and the values of $P_0(r)$ and its derivatives, evaluated at the origin. From this expression, it is seen that the boundary condition

$$\left. \frac{\partial}{\partial r} P_0(r) \right|_0 = 0 \ , \tag{3.26}$$

is sufficient to make the flux scale as (to leading order) $q \sim B_1 r$ for $r \to 0$ and to keep the divergence finite.

In the remaining Chapters and sections of this manuscript, the $n = 0$ radial fractional model defined by the equations (3.21), (3.22), and (3.23) is of primary interest. In the subsequent discussion of the azimuthally averaged model, the reference to 0 in the sub- and superscripts are dropped so that the scalar profile P_0, kernel $K_\alpha^{(0)}(r,r')$, etc. are referred to by

$$P_0(r,t) \mapsto P(r,t)\,, \quad K_\alpha^{(0)}(r,r') \mapsto K_\alpha(r,r')\,. \tag{3.27}$$

Likewise, the $n = 0$ model is simply referred to as the *radial fractional model.*

3.2.3 Green's function solutions of the initial value problem

The initial value problem associated with the 2D fractional diffusion equation (3.12) has solutions that can be given in terms of a propagator function or a Green's function $G(|\vec{x}-\vec{x}'|,t)$. For an arbitrary initial condition $f(x)$, the solutions are

$$P(\vec{x},t) = \int\int f(\vec{x}')\, G\left(|\vec{x}-\vec{x}'|,t\right)\, \mathrm{d}\vec{x}' \quad . \tag{3.28}$$

The Fourier transform of $G(|\vec{x}-\vec{x}'|,t)$ can be found from equation (3.12) with expression (3.5) and the initial condition $G(|\vec{x}-\vec{x}'|,t=0) = \delta(\vec{x}-\vec{x}')$. When transformed back to configuration space, the Green's function takes the form

$$\begin{aligned} G(|\vec{x}-\vec{x}'|,t) &= \mathcal{F}^{-1}\left[\exp\left(i\vec{k}\cdot\vec{x}' - \chi_\alpha\,|\vec{k}|^\alpha\, t\right)\right] \\ &= \frac{1}{2\pi}\,\left(\chi_\alpha\, t\right)^{-2/\alpha} \int_0^\infty y\, e^{-y^\alpha}\, J_0\left(\frac{|\vec{x}-\vec{x}'|}{(\chi_\alpha t)^{1/\alpha}}\, y\right)\, \mathrm{d}y \quad , \end{aligned} \tag{3.29}$$

where $J_0(z)$ is the zeroth-order Bessel function[AS72]. The Green's functions are self-similar, meaning they can be expressed as

$$G(|\vec{x}-\vec{x}'|,t) = (\chi_\alpha\, t)^{-2/\alpha}\, \mathcal{G}(X) \quad , \tag{3.30}$$

where X is the self-similarity variable

$$X = \frac{|\vec{x}-\vec{x}'|}{\left(\chi_\alpha\, t\right)^{1/\alpha}} \quad . \tag{3.31}$$

The dependence of $\mathcal{G}(X)$ on X for different values of α is illustrated in the log-log display of figure 3.1. The dashed line fits for large X indicates a power-law behavior

$$\mathcal{G}(X) \sim \frac{1}{X^{\alpha+2}}\ . \tag{3.32}$$

This scaling is a consequence of assumption (3.2) concerning the nature of the jump distributions. It should be noted that in 1D, the Green's function has the scaling $\sim |x|^{-\alpha-1}$.

As in the full 2D model, there exist radial Green's functions $G_{radial}(r, r', t)$ for the isotropic radial diffusion equation (3.21). These Green's functions describe the time evolution of the 2D azimuthally symmetric delta function in radius, a ring centered at r',

$$G_{radial}(r, r', t = 0) = \frac{\delta(r - r')}{2\pi r'} \ . \tag{3.33}$$

The solutions to the initial value problem, with initial condition $f(r)$, are given in terms of a convolution integral as follows

$$P(r, t) = 2\pi \int_0^\infty r' f(r')\, G_{radial}(r, r', t)\, \mathrm{d}r' \ . \tag{3.34}$$

The expression for the radial Green's functions can be found by substituting the initial condition (3.33) into the general convolution expression (3.28) to obtain

$$G_{radial}(r, r', t) = \frac{(\chi_\alpha\, t)^{-2/\alpha}}{2\pi} \int_0^\infty y\, e^{-y^\alpha}\, J_0\left(\frac{r}{(\chi_\alpha t)^{1/\alpha}}\, y\right)\, J_0\left(\frac{r'}{(\chi_\alpha t)^{1/\alpha}}\, y\right)\, \mathrm{d}y \ . \tag{3.35}$$

Note that when $r' = 0$ the radial Green's function reduces to the 2D self-similar Green's function (3.29).

When $r' \neq 0$, the radial Green's functions approximate the Cartesian Green's functions for small times. By introducing the dimensionless time variable $\tilde{t} = \chi_\alpha\, t / r'^\alpha$ into (3.35), and taking the limit $\tilde{t} \to 0$ and $r/r' \to 1$, the radial Green's function reduces to

$$2\pi\, r'^2\, G_{radial}(r, r', t) \sim \tilde{t}^{-1/\alpha}\, \frac{1}{2\pi} \sqrt{\frac{r'}{r}} \left[\int_{-\infty}^\infty e^{-|y|^\alpha} \cos\left(\frac{r - r'}{(\chi_\alpha\, t)^{1/\alpha}}\, y\right)\, \mathrm{d}y + O\left(\tilde{t}^{1/\alpha}\right) \right] \ . \tag{3.36}$$

When $r \approx r'$, the leading order part of (3.36) is equivalent to the Cartesian Green's function given by

$$\begin{aligned} G_{cart}(x-x',t) &= \frac{1}{2\pi}\int_{-\infty}^{\infty} \exp\left[ik\,(x-x') - \chi_\alpha\,|k|^\alpha\,t\right]\,\mathrm{d}k \\ &= \frac{1}{2\pi}\,(\chi_\alpha\,t)^{-1/\alpha}\int_{-\infty}^{\infty} \exp\left[ik\,\frac{(x-x')}{(\chi_\alpha\,t)^{1/\alpha}} - |k|^\alpha\right]\,\mathrm{d}k \quad . \end{aligned} \tag{3.37}$$

It should be noted that both the Cartesian and the small-time radial Green's functions are self-similar, i.e., they can be written as

$$2\pi r'^2\,G_{radial}(r,r',\tilde{t} << 1) \approx x'\,G_{cart}(x-x',t) = \tilde{t}^{-1/\alpha}\,\mathcal{G}(X)\ , \tag{3.38}$$

with self-similarity variables

$$X = \frac{r-r'}{(\chi_\alpha\,t)^{1/\alpha}} = \frac{x-x'}{(\chi_\alpha\,t)^{1/\alpha}}\ . \tag{3.39}$$

As a measure of the agreement between the radial and Cartesian Green's functions, figure 3.2 displays in log-linear format the dependence of $2\pi\,r'^2\,\tilde{t}^{1/\alpha}\,G_{radial}(r,r',t)$ on X for several different times. For small times, the time-rescaled Green's functions collapse onto the self-similar function $\mathcal{G}(X)$ which is also the self-similar function for the Cartesian Green's functions. At longer times the influence of the origin is felt and the left tail of the radial Green's function lifts and departs from the Cartesian self-similar function. In summary, for initial pulses, the slab approximation requires

$$\tilde{t} = \frac{\chi_\alpha\,t}{r'^\alpha} << 1 \quad \text{and} \quad r \approx r'\ . \tag{3.40}$$

Figure 3.3 displays the temporal decay of the radial Green's functions at the peak $r = r'$; they obey the power law $G_{radial}(r',r',t) \sim \tilde{t}^{-1/\alpha}$.

3.2.4 Isotropic fractional diffusion in a bounded domain

This section examines a model of fractional diffusion for a disk of finite radius L. Obtaining a well-defined bounded-domain model for fractional diffusion is

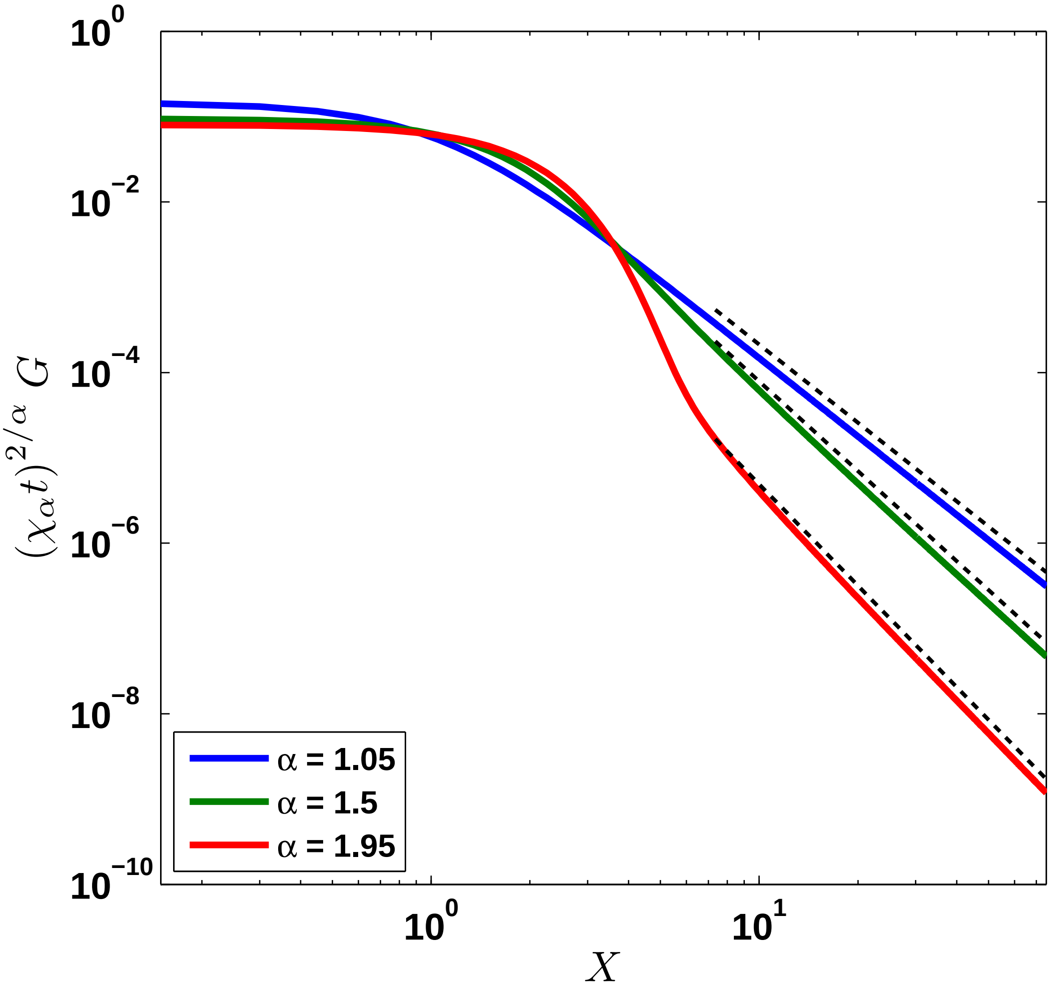

Figure 3.1: Log-log display of the scaled Green's function $\mathcal{G}(X)$ from equation (3.30) for different values of α. The dashed lines are the power law fits $\mathcal{G} \sim X^{-\alpha-2}$.

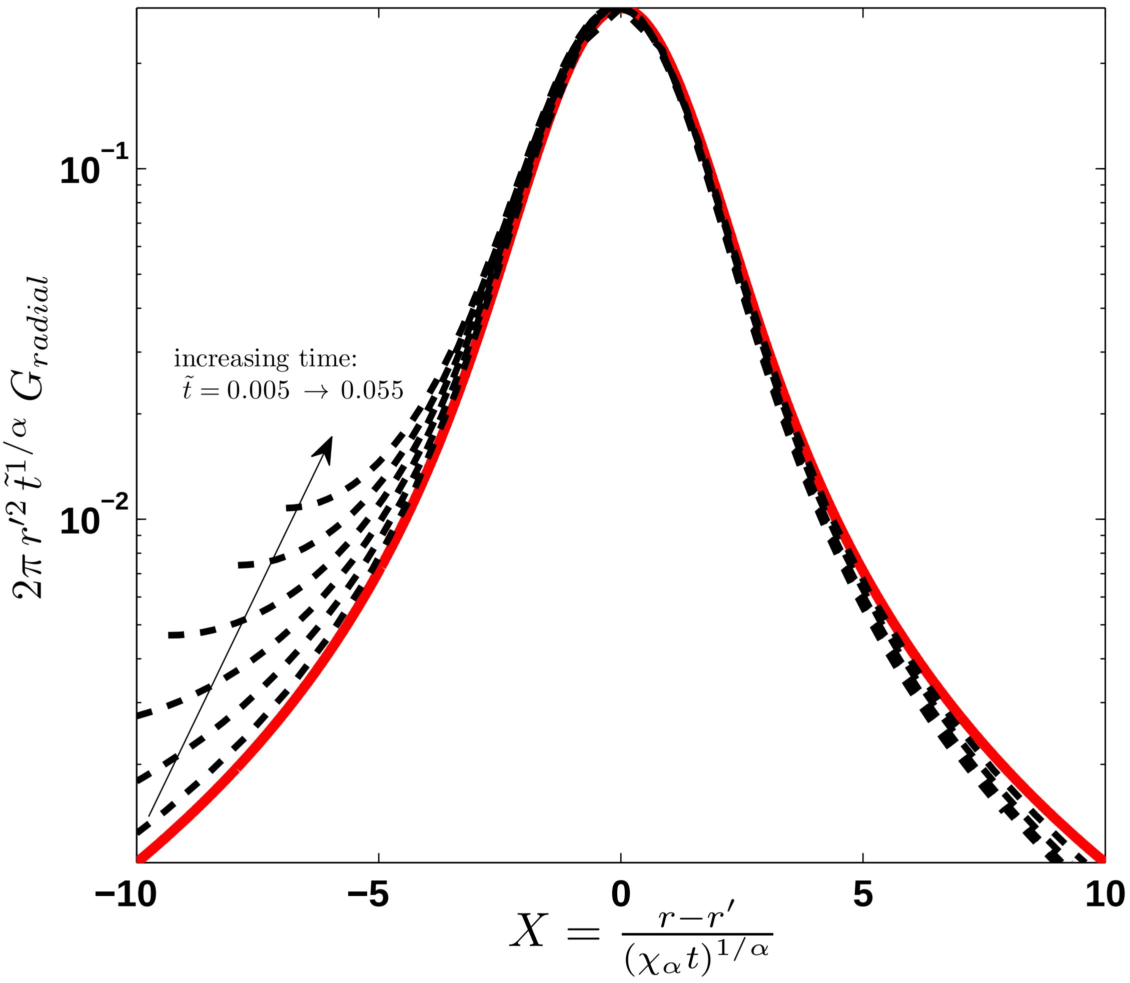

Figure 3.2: Log-linear display of radial Green's function (3.35) at different times for $\alpha = 1.5$. The red curve is the Cartesian self-similar function $\mathcal{G}(X)$ that appears in (3.38). The peak of the radial Green's function is re-scaled at each time by multiplying with a factor of $\tilde{t}^{1/\alpha}$. At earlier times, the scaled radial Green's function well approximates the Cartesian self-similar function. At later times, the radial and Cartesian functions deviate at the origin.

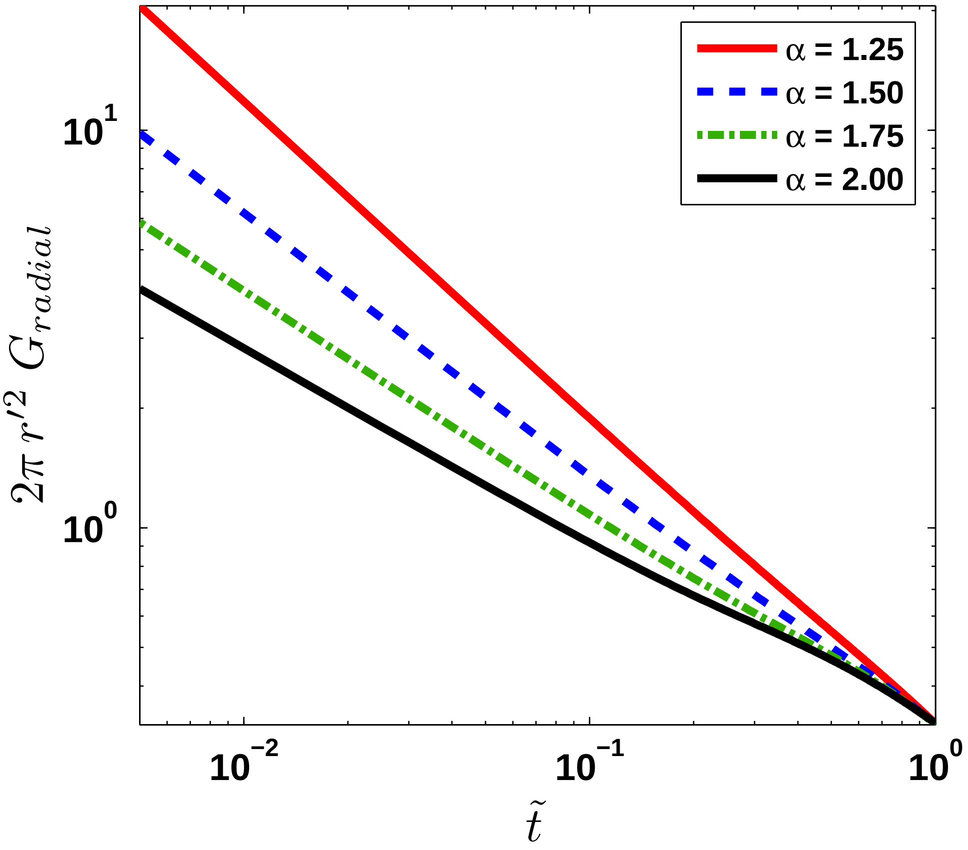

Figure 3.3: Time dependence of the peak value of the radial Green's functions given by (3.35). For small times the peaks behave according to the power law $G_{radial}(r', r', \tilde{t}) \sim \tilde{t}^{-1/\alpha}$.

not straightforward. Such a model requires that the range of integration in the (radial) fractional Laplacian $\Delta_r^{\alpha/2}$ be limited to the bounded domain $0 < r' < L$. If the range of integration is simply truncated in the unbounded domain fractional operator, without modifying the kernel, then there are two possible finite domain models (in light of equation (3.10))

$$ {}^{C}\Delta_{r,L}^{\alpha/2} P(r) = \int_0^L r' K_\alpha(r,r') \, \frac{1}{r'} \frac{\partial}{\partial r'} \left[r' \frac{\partial}{\partial r'} P(r') \right] \mathrm{d}r' \ , \tag{3.41} $$

$$ {}^{R}\Delta_{r,L}^{\alpha/2} P(r) = \frac{1}{r} \frac{\partial}{\partial r} \left[r \frac{\partial}{\partial r} \int_0^L r' K_\alpha(r,r') \, P(r') \, \mathrm{d}r' \right] \ . \tag{3.42} $$

Note that these two expressions *are no longer* equivalent; the integration and the radial part of the conventional Laplacian can only be commuted when the range of integration goes to infinity or when $P(L) = P'(L) = 0$. The superscripts "C" and "R" on the operators refer to the fractional derivatives "Caputo" and "Riemann-Liouville", respectively, which have the same ordering of integration and derivatives[Pod99] as the operators defined previously.

These operators appear to be the straightforward application of the fractional Laplacian (3.11) to a bounded domain; however they both result in unsatisfactory models for different reasons. The Riemann-Liouville type of fractional Laplacian ${}^{R}\Delta_{r,L}^{\alpha/2}$ has singularities at the boundary. The leading order singular terms of ${}^{R}\Delta_{r,L}^{\alpha/2} P(r)$ are as follows

$$ \begin{aligned} & \frac{1}{r} \frac{\partial}{\partial r} \left[r \frac{\partial}{\partial r} \int_0^L K_\alpha(r,r') P(r') \, \mathrm{d}r' \right] \sim \\ & \frac{2\pi}{\gamma_\alpha} \left(-\frac{1}{L} (2-\alpha) \, c_1 \, P(L) + (2-\alpha)(3-\alpha) \left[c_2 \, P(L) + c_3 \, P'(L) \right] \right) (L-r)^{1-\alpha} \\ & \qquad + \frac{2\pi}{\gamma_\alpha} (2-\alpha)(1-\alpha) \, c_1 \, P(L) \ (L-r)^{-\alpha} + O\left(1\right) \ , \end{aligned} \tag{3.43} $$

where the c_j's are numerical constants (cf. section A.4). This operator has singularities if $P(L)$ and $P'(L)$ are non-zero.

The Caputo-type of fractional Laplacian is regular regardless of the boundary conditions at $r = L$. Mathematically this operator is well-posed and produces a solvable fractional derivative equation. However, whenever steep negative gradients appear at the boundary (for example, if a narrow, positive heat source is located near the boundary) then the Caputo bounded-domain model predicts cooling in the core of the system that is proportional to the strength of the positive heat source near the edge. This effect is due to a spurious flux term that is included to keep ${}^{C}\Delta_{r,L}^{\alpha/2}$ finite at the boundary.

To overcome these deficiencies, the Riemann-Liouville operator (3.42) is adopted, but with the incorporation of a modified kernel that includes a mask function $H_\alpha(r)$ whose purpose is to ensure that the operator is finite at the boundary. The proposed bounded-domain operator has the form

$$\Delta_{r,L}^{\alpha/2} P(r) \equiv \frac{1}{r}\frac{\partial}{\partial r}\left[r\frac{\partial}{\partial r}\int_0^L r' K_\alpha(r,r')\, H_\alpha(r')\, P(r')\, \mathrm{d}r' \right] , \tag{3.44}$$

where $H_\alpha(r)$ obeys the conditions

$$H_\alpha(L) = 0 \ , \quad \frac{d}{dr} H_\alpha(L) = 0 \ . \tag{3.45}$$

These conditions on $H_\alpha(r)$ ensure that the singular part of the operator (cf. (3.43)) is removed via a narrow and smoothly varying boundary layer. In the interior of the domain, $H_\alpha(r) = 1$.

Although the mask function removes the singularities associated with (3.42), the operator (3.44) is not well posed when a boundary condition is included. Because $H_\alpha(r)$ is zero near the boundary, any possible solution in the interior of the domain is independent of the boundary value and it is not possible to solve the diffusion equation while satisfying an arbitrary boundary condition. The situation is similar to what would occur if one tried to find the steady-state solution to a conventional diffusion equation

$$\frac{d}{dx}\left[\chi_d(x) \frac{d}{dx} P(x) \right] = 0 \quad x \in [a,b] \ , \tag{3.46}$$

for $\chi_d(x)$ vanishing at $x = b$. In this case the steady-state solution has the form

$$P(x) = P(a) + \int_a^x \frac{\beta}{\chi_d(x')}\, \mathrm{d}x' \ , \tag{3.47}$$

which cannot satisfy the boundary condition at $x = b$ since the singular integral requires that the constant $\beta = 0$ for a finite solution. To obtain a well-posed fractional model, it is necessary to include at least a boundary layer of conventional diffusion that connects the interior of the domain to the boundary. This motivates the final definition of a bounded domain fractional Laplacian operator

$$\begin{aligned}\Delta_{r,L}^{\alpha/2} P(r) \equiv \frac{1}{r}\frac{\partial}{\partial r}\left[r\frac{\partial}{\partial r}\int_0^L r' K_\alpha(r,r')\, H_\alpha(r')\, P(r')\, \mathrm{d}r'\right] \\ + \zeta\, \frac{1}{r}\frac{\partial}{\partial r}\left[r\left[1 - H_\alpha(r)\right]\frac{\partial}{\partial r}P(r)\right] \ ,\end{aligned} \tag{3.48}$$

where ζ has units of $[\text{length}]^{2-\alpha}$ and controls the strength of the boundary layer. Equation (3.48) represents a well-posed, stand-alone, radial fractional diffusion operator when $\zeta \neq 0$ and can be used for systems in which transport is purely fractional in the interior. The first integro-differential operator is labeled the masked Riemann-Liouville operator and the second term the boundary layer diffusion operator.

If a finite amount of conventional diffusion is retained throughout the domain, including at the boundary, it is possible to drop the boundary layer diffusion term by setting $\zeta = 0$ and still have a well-posed equation. In this case the fractional diffusion is considered to be an enhancement of the background diffusion and as something that cannot exist without the background diffusion present.

The flux that corresponds to the bounded domain fractional Laplacian (3.48) is

$$q(r) = -\chi_\alpha \left[\frac{\partial}{\partial r}\int_0^L r'\, K_\alpha(r,r')\, H_\alpha(r')\, P(r')\, \mathrm{d}r' + \zeta\ (1 - H_\alpha(r))\ \frac{\partial}{\partial r}\, P(r)\right] \ . \tag{3.49}$$

Before the bounded domain fractional Laplacian proposed in (3.48) can be applied, the mask function $H_\alpha(r)$ and the boundary layer diffusion strength ζ must be chosen. While the mask function is partially determined by the boundary conditions (3.45) and the amorphous condition that $H_\alpha(r) = 1$ for r in the interior, the width of the boundary layer in which $H_\alpha(r)$ goes from 1 to 0 remains arbitrary. The calculations presented in Sec. 3.3 use a mask function of the form

$$H_\alpha(\rho) = 1 - \exp\left[-\left(\frac{\rho-1}{b}\right)^2\right] \quad ; \quad 0 < \rho < 1 \ , \tag{3.50}$$

with the boundary layer width set by b. In systems with no source and a finite Dirichlet boundary condition, the boundary width and ζ can significantly influence the temperature profiles throughout the entire domain. However, the temperature profiles resulting from a source with homogeneous Dirichlet boundary condition can be made relatively insensitive to the choice of ζ, and width b, if these quantities are made sufficiently small. Figure 3.4 provides a quantitative assessment for the sensitivity of the results to the values of the mask parameters. The curves displayed (for fractional order $\alpha = 1.5$) show the dependence of the percentage change in average interior temperature on the width parameter b for several choices of the diffusivity strength ζ. The average temperatures (on $\rho \in [0,\ 0.9]$) are calculated from the steady state radial fractional diffusion equation that is formed with (3.48) and (3.50) (cf. (3.52)) with heat source

$$S(\rho) = \begin{cases} 1 & 0 < \rho < 0.5 \\ 0 & 0.5 \le \rho \le 1 \end{cases} \ . \tag{3.51}$$

It is seen from figure 3.4 that for narrow boundary layers, the average temperatures converge to an asymptotic value regardless of value of ζ. In the following sections, calculations are presented that use the values $b = 0.025\,L$ and $\zeta = 1.0\,L^{2-\alpha}$ which, in figure 3.4, results in an 4.4% difference from the $b \to 0$ asymptotic value.

3.3 Applications

This section examines several applications of the radial fractional model for a bounded domain. Although the transport problems considered here are general, most of the applications are motivated by transport in magnetically confined plas-

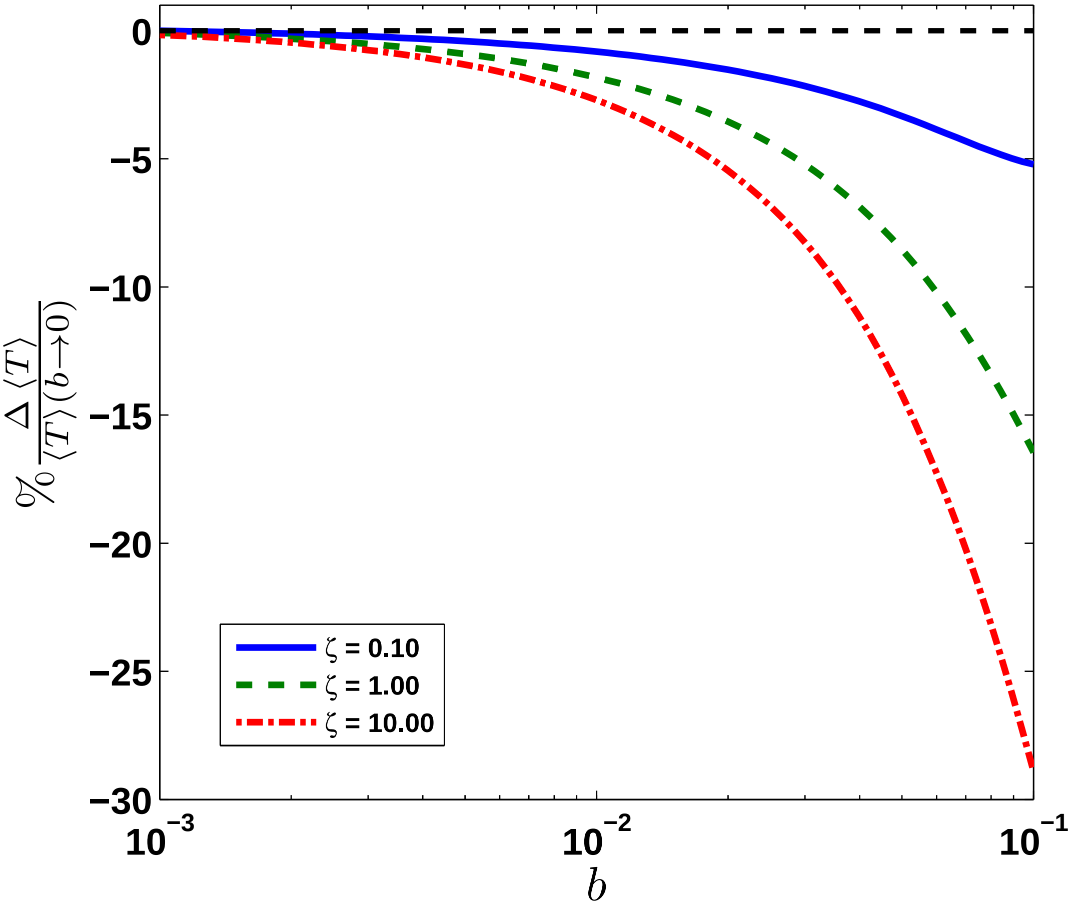

Figure 3.4: Sensitivity of results to parameters of mask function (b, ζ). Curves correspond to the percentage fractional change in calculated average values described in the text. The percentage change is measured relative to the narrow width $b \to 0$ asymptotic value. The fractional order is $\alpha = 1.5$.

mas. The radial model is well-suited, in particular, for idealized models of plasmas confined in tokamaks or stellarators since the temperature in those devices rapidly equilibrates on each magnetic surface and only radial transport is relevant to confinement. In Chapter 5, the application of the radial fractional model to transport situations observed in tokamaks is explored in greater detail. The following discussions are based on numerical solutions (cf. appendix B) of the radial fractional diffusion equation

$$\frac{\partial}{\partial t}T(\rho,t) = \tilde{\chi_\alpha}\,\Delta^{\alpha/2}_{\rho,L}T(\rho,t) + \tilde{\chi_d}\,\frac{1}{\rho}\frac{\partial}{\partial\rho}\left[\rho\,\frac{\partial}{\partial\rho}T(\rho,t)\right] + S(\rho)\ ;\ 0<\rho<1\ , \quad (3.52)$$

where $S(\rho)$ is a source term. The computational domain is fixed to the interval $[0,\ 1]$; this is reflected in equation (3.52) with the use of the scaled parameters

$$\tilde{\chi_\alpha} = \frac{\chi_\alpha}{L^\alpha} \quad \tilde{\chi_d} = \frac{\chi_d}{L^2} \quad \rho = \frac{r}{L} \quad \tilde{\zeta} = \frac{\zeta}{L^{2-\alpha}} \quad , \quad (3.53)$$

where χ_α, χ_d, ρ and ζ are their dimensional counterparts. Table 3.1 reports the different values of the model parameters used in each figure.

All the calculations (excluding those shown in figure 3.13) use a mask function of the form

$$H_\alpha(\rho) = 1 - \exp\left[-\left(\frac{\rho-1}{0.025}\right)^2\right] \quad 0<\rho<1\ . \quad (3.54)$$

The e-folding length of the boundary layer is set to 2.5% of the domain size. For most of the calculations reported here this choice results in boundary layers that have negligible effects on the interior solutions. In all calculations a boundary layer diffusion strength of

$$\tilde{\zeta} = \frac{\zeta}{L^{2-\alpha}} = 1\ , \quad (3.55)$$

is used.

Figure	α	$\tilde{\chi_\alpha}$	$\tilde{\chi_d}$	$\tilde{\zeta}$
3.5	1.25, 1.50, 1.75, 2.00	1	0	1
3.6	1.5	1	0	1
3.7	1.5	1	0.5	1
3.8	1.25	$\left(\frac{L}{\hat{L}}\right)^{2-\alpha}$	1	1
3.9	1.25	$\left(\frac{L}{\hat{L}}\right)^{2-\alpha}$	0	1
3.10	1.25, 1.50, 2.00	$\left(\frac{L}{\hat{L}}\right)^{2-\alpha}$	0	1
3.11	1.25, 1.50, 1.75, 2.00	1	0	1
3.12	1.5	1	0	1
3.13	1.5	1	0	1

Table 3.1: Model parameter values

3.3.1 Steady-state solutions

3.3.1.1 Uphill transport

In systems with non-local fractional diffusion, it is possible for the heat flux to flow uphill or in the same direction as the temperature gradient. This uphill transport is in contrast to conventional diffusion models in which Fick's law holds and the heat flux always flows opposite the direction of the temperature gradient.

A non-trivial example of uphill transport occurs in the radial fractional model when no heat source ($S(\rho) = 0$) is present, but the surrounding wall is held at a fixed temperature. In this case the non-local component of the flux

$$q_{nonlocal}(\rho) = -\chi_\alpha \frac{\partial}{\partial \rho} \int_0^1 \rho' \, K_\alpha(\rho, \rho') \, H_\alpha(\rho') \, T(\rho') \, \mathrm{d}\rho' \quad , \tag{3.56}$$

is directed uphill inside the boundary layer. This uphill component of the flux exactly cancels the downhill flux driven by conventional diffusion in the boundary layer, and this cancellation prevents the core from reaching the same temperature as the wall. Figure 3.5 shows the resulting profiles; the inset shows the non-local flux inside the boundary layer. Note that for conventional diffusion, the steady-state temperature profile is flat, i.e., the interior temperature is radially uniform and its value is equal to the wall temperature.

Uphill transport also appears when an off-axis heating source is included, as shown by the steady-state temperature profiles found for the following heat source

$$S(\rho) = \Theta(\rho; 0, 0.9) + 100\,\Theta(\rho; 0.7, 0.75) \quad , \tag{3.57}$$

where

$$\Theta(\rho; a, b) = \begin{cases} 1 & \rho \in [a,\ b] \\ 0 & \text{otherwise} \end{cases} \quad . \tag{3.58}$$

This heat source consists of two components: a weak, spatially uniform heater and a strong, spatially localized source placed at $\rho = 0.7$. Such a situation is

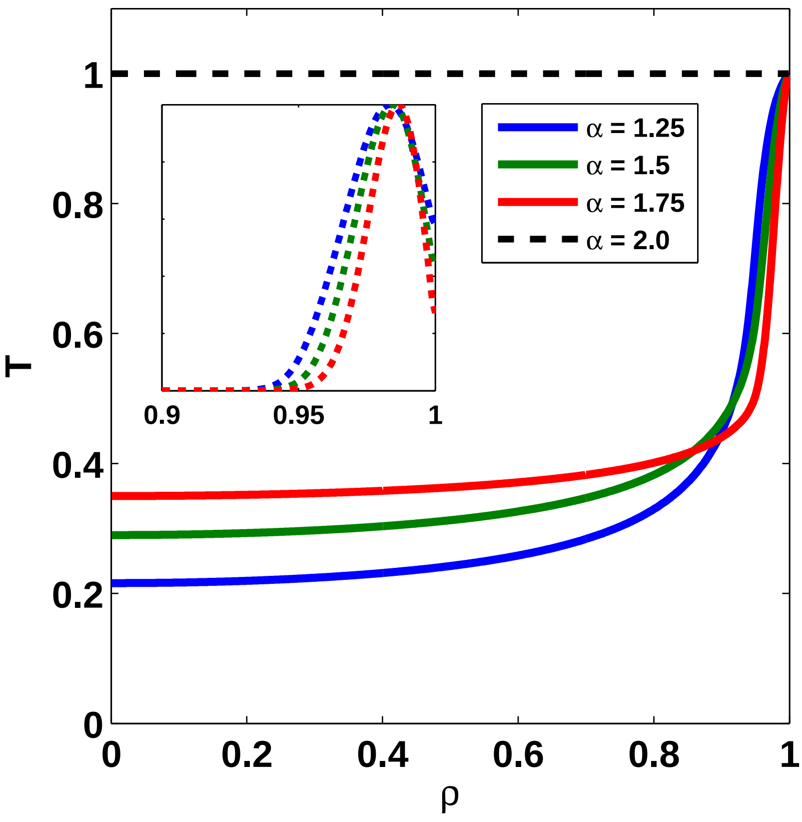

Figure 3.5: Radial dependence of temperature exhibits uphill fractional transport in a system with no heat source, but with fixed wall temperature (T(1)=1). The profiles are calculated from the steady-state model formed from equations (3.52) and (3.54) with model parameters given in Table 3.1. The inset shows the non-local flux given by (3.56) inside the narrow boundary layer.

characteristic of tokamak confinement devices that are heated by the off-axis, electron cyclotron resonance technique. Figure 3.6 displays the resulting steady-state temperature profile with the corresponding total heat flux for $\alpha = 1.5$. For nearly the entire domain ($\sim 70\%$) the heat flux is uphill. As in the no source case of figure 3.5, this uphill flux results in a profile with a reduced core temperature.

The upward concavity of the profiles in the interior of the system is a persistent feature of the radial fractional model when an off-axis heat source is present. This is in marked contrast to the temperature profiles obtained from the Cartesian fractional model proposed in [Cas06], which does not give rise to hollow profiles. In fact the symmetric Cartesian fractional model predicts profile peaking or high temperature near the core. Figure 3.7 compares a steady-state temperature profile predicted by the radial model (3.52) to a temperature profile found from the Cartesian model with fractional diffusivity given in equation (3.62) below. For sources that maintain equal heat fluxes, it is found that the Cartesian model displays an enhancement in temperature near the core while the radial model predicts a *hollow* profile in which the central temperature is a local minimum.

To better appreciate the meaning of the comparison shown in figure 3.7, it should be noted that the radial profile in figure 3.7 is found with the radial source

$$S_{radial}(\rho) = \frac{1}{\rho} \exp\left[-\left(\frac{\rho - 0.7}{0.05} \right)^2 \right] , \tag{3.59}$$

while the comparison Cartesian profile is found with the source

$$S_{cart}(x) = S_{radial}(x) - \frac{q_r(x)}{x} , \tag{3.60}$$

where q_r is the steady-state heat flux set up by the radial source (the radial integral of (3.59))

$$q_r(\rho) = \frac{\sqrt{\pi}}{2} \frac{0.05}{\rho} \left[\operatorname{erf}\left(\frac{\rho - 0.7}{0.05} \right) + \operatorname{erf}\left(\frac{0.7}{0.05} \right) \right] . \tag{3.61}$$

These different sources are chosen so that $q_x(x) = q_r(\rho)$ when $x = \rho$. Also, the

Cartesian model uses a fractional diffusivity shape-function

$$\kappa(x) = \frac{1}{2}\left[\tanh\left(\frac{x-0.1}{0.025}\right) + \tanh\left(\frac{0.1}{0.025}\right)\right] \ , \tag{3.62}$$

to make the heat flux vanish at the origin.

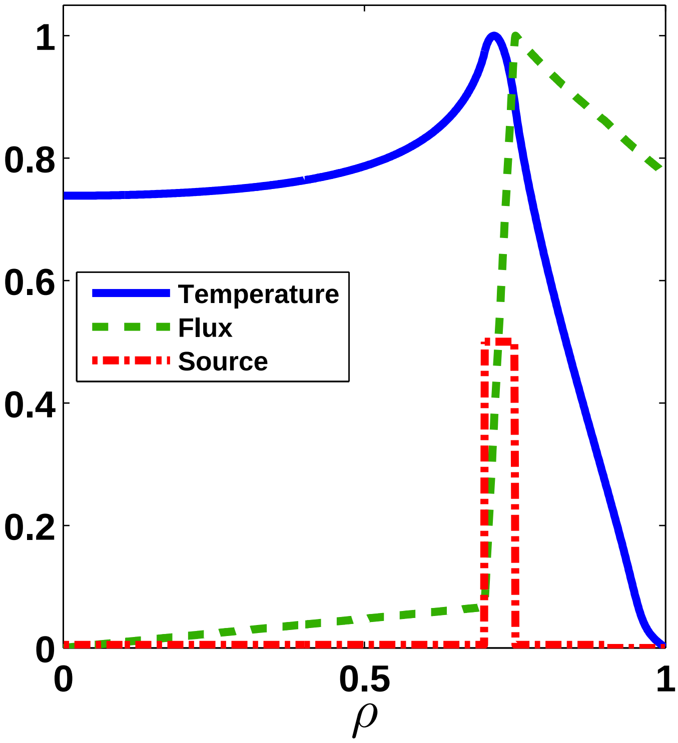

Figure 3.6: Radial dependence of temperature showing uphill fractional transport when an off-axis heat source (3.57) is present according to the radial fractional model (3.52) with parameter values given in Table 3.1. Both the temperature profile and the flux profile have been normalized by their maximum values; the source profile has been normalized to half the figure height. The region of uphill transport is approximately contained in the interval $\rho < 0.72$.

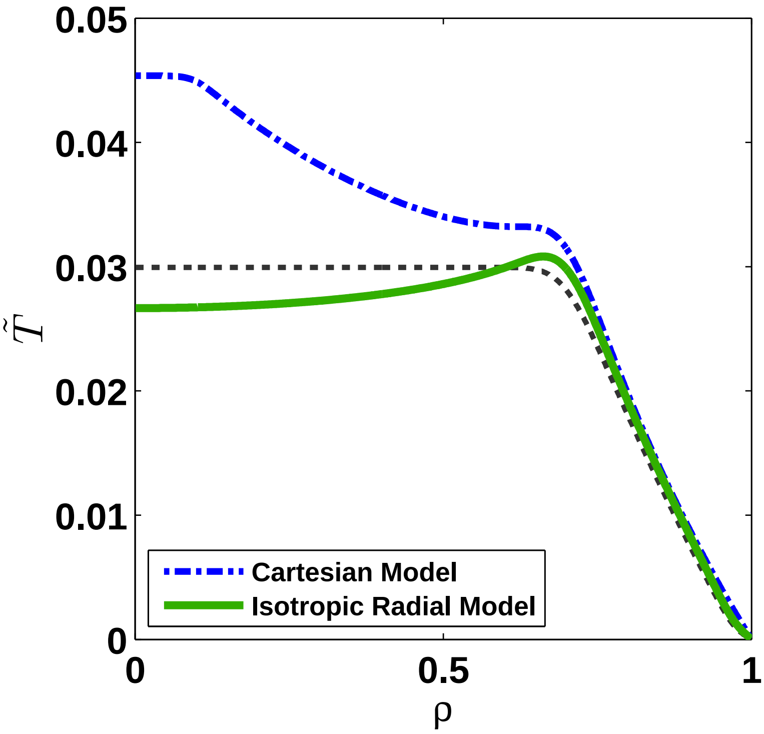

Figure 3.7: Comparison of the isotropic radial fractional model given by (3.52) and (3.54) to the Cartesian fractional model proposed in Ref. [Cas06] with diffusivity shape (3.62). The black dotted curve is the radial temperature profile with only conventional diffusion. The radial and Cartesian profiles are found from the sources (3.59) and (3.60), respectively, so that the fluxes for both cases are equal. While the Cartesian model predicts profile peaking, or an enhancement of the temperature at the origin, the isotropic radial model results in a hollow core.

3.3.1.2 Scaling of the confinement time

A common figure of merit used in describing the global transport in a steady-state system is the confinement time, defined for a disk as

$$\tau_c = \frac{\int_0^L \, rT(r) \, \mathrm{d}r}{\int_0^L \, rS(r) \, \mathrm{d}r} \ , \tag{3.63}$$

where $S(r)$ is the source and $T(r)$ is the steady-state temperature profile. To quantify the dependence of the confinement time on domain size L, it is useful to introduce the time and length scales

$$\tau_d \equiv \tilde{\chi}_d^{-1} \ , \qquad \hat{L} \equiv \left(\frac{\chi_d}{\chi_\alpha} \right)^{1/(2-\alpha)} \ . \tag{3.64}$$

Note that the length scale $\hat{L}$ is independent of the domain size L and is defined in terms of the dimensional diffusivities χ_α and χ_d. Equation (3.52) can be rewritten in terms of these parameters to obtain the dimensionless equation

$$\left(\frac{L}{\hat{L}} \right)^{2-\alpha} \Delta_{\rho,L}^{\alpha/2} \tilde{T}(\rho) + \Delta_\rho \tilde{T}(\rho) + \tilde{S}(\rho) = 0 \quad , \tag{3.65}$$

with dimensionless functions

$$\tilde{T}(\rho) = \frac{T(\rho)}{\tau_d \, S_0} \ , \qquad \tilde{S}(\rho) = \frac{S(\rho)}{S_0} \ , \tag{3.66}$$

where S_0 is the peak strength of the source. The confinement time when expressed with (3.64) becomes

$$\tau_c/\tau_d = \frac{\int_0^1 \, \rho\tilde{T}(\rho) \, \mathrm{d}\rho}{\int_0^1 \, \rho\tilde{S}(\rho) \, \mathrm{d}\rho} \ , \tag{3.67}$$

where $\tilde{T}$ is the solution to (3.65).

Panel (a) in figure 3.8 shows the dependence of the confinement time on normalized domain size $L/\hat{L}$ for the representative value of $\alpha = 1.25$. Similar results to those displayed in figure 3.8 have been obtained for other values of α but are not shown. The confinement times are obtained from (3.67) using the temperature profiles, such as those shown in panel (b), calculated from (3.65) and (3.54) with source (3.68). Confinement times are normalized to $\tau_{c,d}$ which is the confinement time, given by equation (3.67), when only the background classical diffusion term in equation 3.65 is present. The horizontal (black) dashed line marks the classical confinement time. The scaled source $\tilde{S}(\rho)$ is

$$\tilde{S}(\rho) = \Theta(\rho; 0, 0.5)\ . \tag{3.68}$$

For small scaled-domains, the confinement time approaches the value $\tau_{c,d}$ and the inclusion of fractional diffusion has a negligible effect on the confinement time. For large scaled-domains, however, the confinement time is significantly reduced from the classical value by the non-local fractional diffusion. This behavior suggests that for fixed diffusivities, the non-local fractional diffusion becomes important (compared to conventional diffusion) when the system size is much larger than the length $\hat{L}$. The effects of non-locality require a relatively large domain in terms of $\frac{L}{\hat{L}}$ to be significant.

Panel (b) in figure 3.8 shows the temperature profiles for different scaled-domain sizes $L/\hat{L}$ as well as the classical profile that is obtained when only classical diffusion is present. When the domain size is small compared to $\hat{L}$, the temperature profile is well approximated by the classical profile. When $L >> \hat{L}$ the temperature profile is significantly reduced relative to the classical profile and the confinement is degraded.

Figure 3.8 offers an opportunity to determine the value of the fractional diffusivity and assess the importance of non-diffusive transport in a particular device by using the measured ratio of the device confinement time to the confinement time for *Classical* diffusion. For any fixed value of α, a confinement time plot similar to panel (a) in figure 3.8 can be obtained, and the effective size of the device can be found by matching the ratio between the confinement curve for *Classical* diffusive confinement (the dashed black line) and the confinement curve for the appropriate value of α. For example, if the measured ratio is $1/5$ and $\alpha = 1.25$, figure 3.8 indicates that the measured ratio is matched at $\frac{L}{\hat{L}} = 16.5$. Using this value of the normalized domain size, the value of the fractional diffusivity χ_α can be determined since L and χ_d are known.

3.3.2 Non-locality in cold pulse propagation

As might be expected from the results found for off-axis heat sources, the temporal evolution of the temperature profile when subjected to sudden off-axis cooling (i.e., a cold pulse) also exhibits significant regions of uphill transport. The situation is illustrated in figure 3.9 for an initial cold pulse given at $t = 0$ by

$$\delta T(\rho, t = 0) = -\exp\left[-\frac{(\rho - 0.85)^2}{0.01^2}\right] \quad . \tag{3.69}$$

This figure shows the radial dependence of the flux and temperature at different times and displays the regions of uphill transport indicated by the black boxes. Uphill transport is present until the pulse reaches the core and the profile peak is centered on the origin.

The evolution of an initial cold pulse in the presence of fractional diffusion can display both fast and slow features when compared to the corresponding situation in a system governed by conventional diffusion, depending on the normalized size $\frac{L}{\hat{L}}$ of the bounded domain. To identify the dependence of pulse propagation on the fractional order α, the fractional model

$$\frac{\partial}{\partial t} T(\rho, t) = \tilde{\chi}_\alpha \, \Delta_{\rho,L}^{\alpha/2} \, T(\rho, t) \quad , \tag{3.70}$$

is compared to a benchmark conventional diffusion model

$$\frac{\partial}{\partial t} T(\rho, t) = \tilde{\chi}_d \, \Delta_\rho \, T(\rho, t) \quad . \tag{3.71}$$

To extract the dependence of the pulse propagation on the normalized domain size, the length scale parameter $\hat{L}$ defined in equation (3.64) is again introduced, and equation (3.70) is expressed in the form

$$\frac{\partial}{\partial \bar{t}} T(\rho, \bar{t}) = \left(\frac{L}{\hat{L}}\right)^{2-\alpha} \Delta_{\rho,L}^{\alpha/2} \, T(\rho, \bar{t}) \quad , \tag{3.72}$$

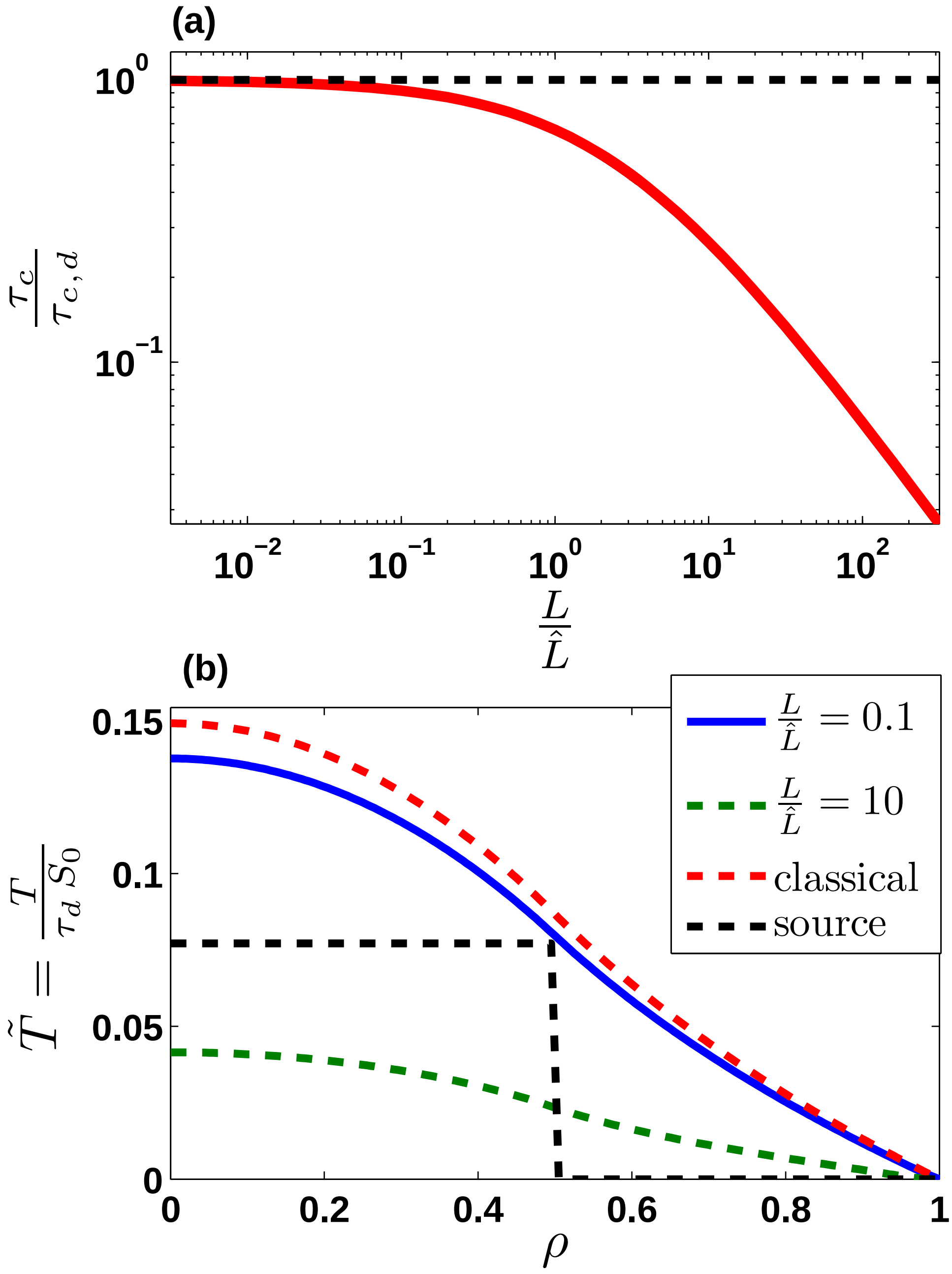

Figure 3.8: (a) Log-log display of dependence of the confinement time $\tau_c/\tau_{c,d}$ on the normalized domain size $L/\hat{L}$ for $\alpha = 1.25$. Confinement times are normalized to the classical confinement time $\tau_{c,d}$ plotted as the (black) dashed line. (b) Radial temperature profiles for selected normalized domain sizes and $\alpha = 1.25$. The classical temperature profile is shown for comparison. Table 3.1 gives the other parameter values.

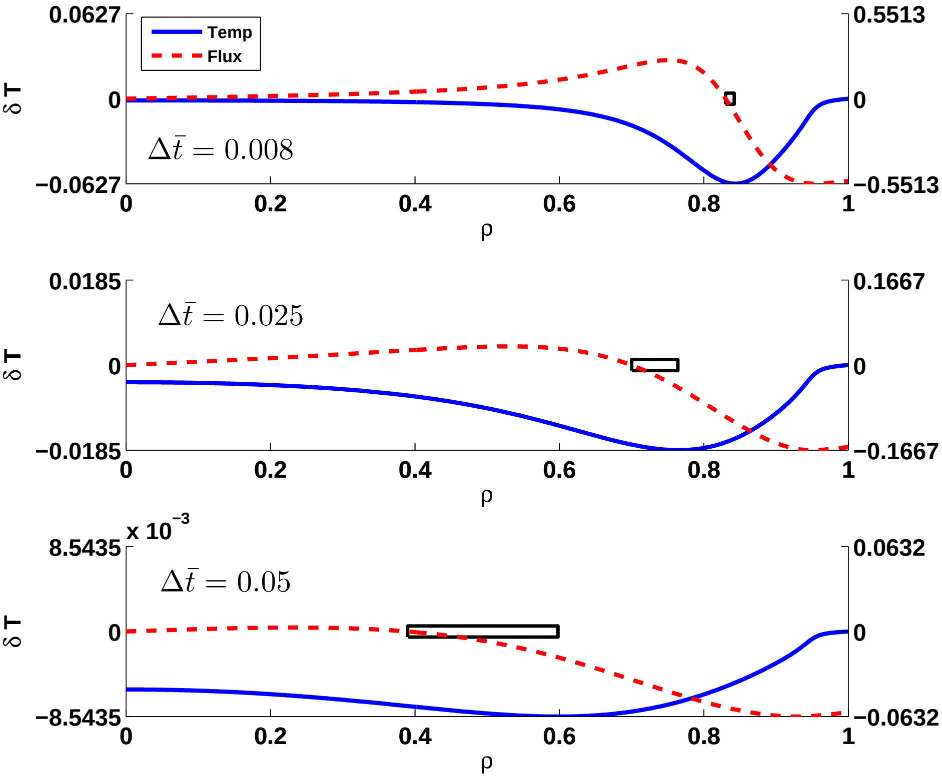

Figure 3.9: Radial dependence of temperature changes and heat flux according to the radial fractional model (3.72) due to an initial cold pulse given by (3.69). A large domain $L = 10\hat{L}$ is used. Table 3.1 gives the other parameter values. The black horizontal boxes show the region of uphill transport. Note that the left y-axis corresponds to the temperature and the right axis to the flux.

where $\bar{t} = \tilde{\chi}_d t$. That is, $\hat{L}$ is defined from the ratio of the fractional diffusivity from (3.70) and the conventional diffusivity from the benchmark equation (3.71). Figure 3.10 shows the time evolution of the temperature change at the origin due to an initial off-axis cold pulse given by (3.69). Two different domain sizes are considered: a relatively small domain, $L = \hat{L}$, and a larger domain, $L = 10\,\hat{L}$. When the domain is small, the conventional diffusion pulse reaches the origin (i.e., the time trace peaks first) before the fractional pulses; when the domain is large, the fractional pulses arrive first.

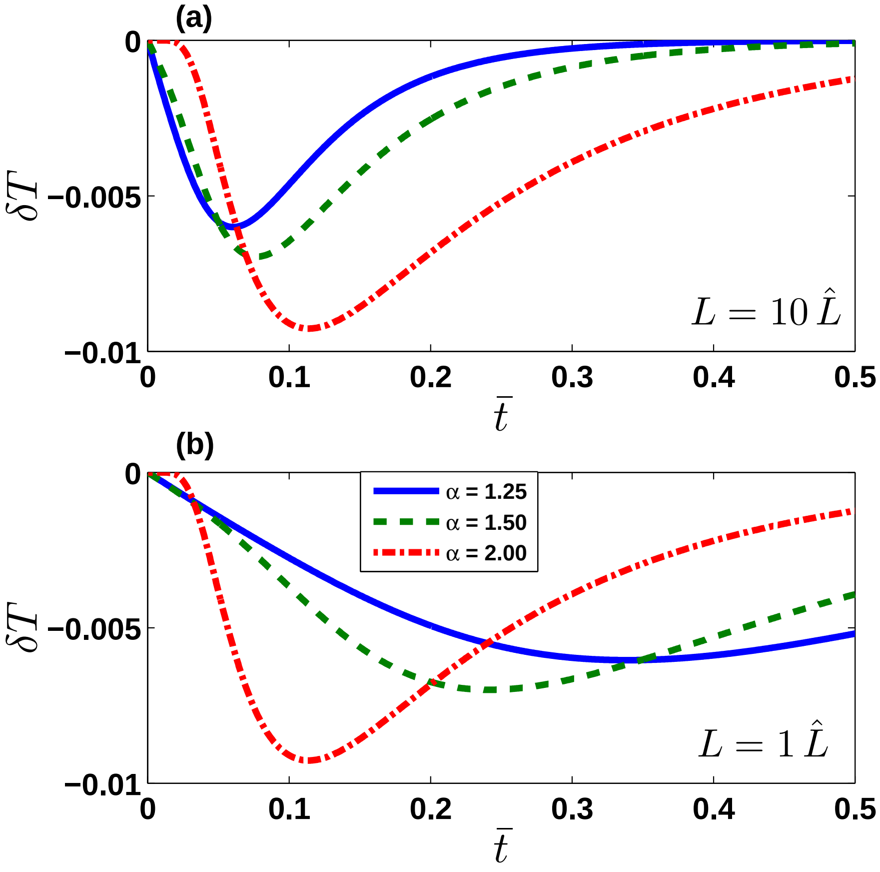

Figure 3.10: Temperature change at the center of the disk due to an initial cold pulse at $t = 0$ given by (3.69). The influence of domain size is illustrated. Panel (a) corresponds to a large domain $L = 10\,\hat{L}$ and panel (b) corresponds to a relatively small domain $L = \hat{L}$. In large domains the pulse arrives earlier for fractional diffusion; conversely in small domains the pulse arrives earlier for conventional diffusion.

3.3.3 Fractional thermal waves

The study of thermal waves that are excited by power modulation can be an important way of assessing the transport properties of a system. In the following Chapters, fractional thermal waves are studied in the context of an infinite unbounded domain and a bounded domain resonator (Chapter 4) and in the context of tokamak experimental results (Chapter 5). Thus it is useful to briefly discuss the properties of thermal waves in the radial fractional model. When a modulated power source is present, the $m = 1$ component of the resultant fractional thermal waves are described by the equation

$$-i\omega\,\tilde{T}(\rho) = \tilde{\chi_\alpha}\,\Delta^{\alpha/2}_{\rho,L}\tilde{T}(\rho) + \tilde{S}(\rho)\ , \tag{3.73}$$

where ω is the angular frequency of the power modulations, and $\tilde{T}$ represents the $m = 1$ mode of the complete Fourier expansion of the temperature, i.e.,

$$T(\rho,t) = 2\,\Re\left[\tilde{T}(\rho)\,\exp(-i\omega t)\right] + \sum_{m\neq 1,-\infty}^{\infty}\tilde{T}_m(\rho)\,\exp(-im\omega t)\ . \tag{3.74}$$

Note that in equation (3.73), the same scaled parameters are used as in equation (3.52). In all the calculations presented here the $m = 1$ modulated source $\tilde{S}(\rho)$ is given by

$$\tilde{S}(\rho) = S_0\,\exp\left[-\left(\frac{\rho - 0.5}{\sigma_S}\right)^2\right]\ . \tag{3.75}$$

Figure 3.11 shows the amplitude and phase of $\tilde{T}$ for different values of the fractional order α. As α decreases, both the amplitude and phase profiles become narrower; this trend is a characteristic feature of the radial fractional model.

Figure 3.12 compares the amplitude and phase profiles from the radial fractional model to the amplitude and phase of an exact analytic solution found in Chapter 4 for fractional thermal waves in a 1D Cartesian, unbounded domain. This comparison is done for a large frequency $\omega = 1000\,\tilde{\chi}_\alpha$ in order to minimize any boundary effects in the radial calculation. As is discussed in Chapter

4, the 1D Cartesian fractional thermal waves in an unbounded domain are composed of an outwardly-traveling, exponentially-decaying part, and an anomalous inwardly-traveling part (called the “H function”). In the Cartesian model, these two contributions interfere near the source and produce peaks in the phase of the thermal wave. Figure 3.12 shows that the radial fractional thermal waves also contain such peaks in phase, indicating the presence of an anomalous, inwardly traveling, “H function” contribution to the overall radial thermal wave.

Finally, figure 3.13 presents a study of the sensitivity of the fractional thermal waves solutions on the boundary layer width b. That is, the profiles shown in figure 3.13 are found from equations (3.73), (3.75), and the mask function

$$H_\alpha(\rho) = 1 - \exp\left[-\left(\frac{\rho - 1}{b} \right)^2 \right] , \tag{3.76}$$

where b is the e-folding length of the boundary layer. For $\tilde{\zeta} = 1$, figure 3.13 shows that as b decreases, the amplitude and phase of the thermal waves converge to asymptotic curves. Similar figures can be produced for other values of ζ, i.e., for each ζ, the $b \to 0$ limit produces the same asymptotic amplitude and phase curves as in the $\tilde{\zeta} = 1$ case. Note that this result is only valid for the boundary condition $\tilde{T}(1) = 0$; when a finite modulation is allowed at the boundary, then the thermal wave amplitude and phase are highly dependent on the boundary layer parameters b and ζ near the boundary.

3.4 Conclusion

This Chapter derives a 2D fractional diffusion operator, and presents a poloidal Fourier expansion of the 2D operator that is applicable to cylindrical systems. For systems in which azimuthal symmetry prevails, this Chapter describes a consistent mathematical model, with a practical numerical method reported in appendix B, for the description of fractional diffusion in bounded cylindrical systems. To the

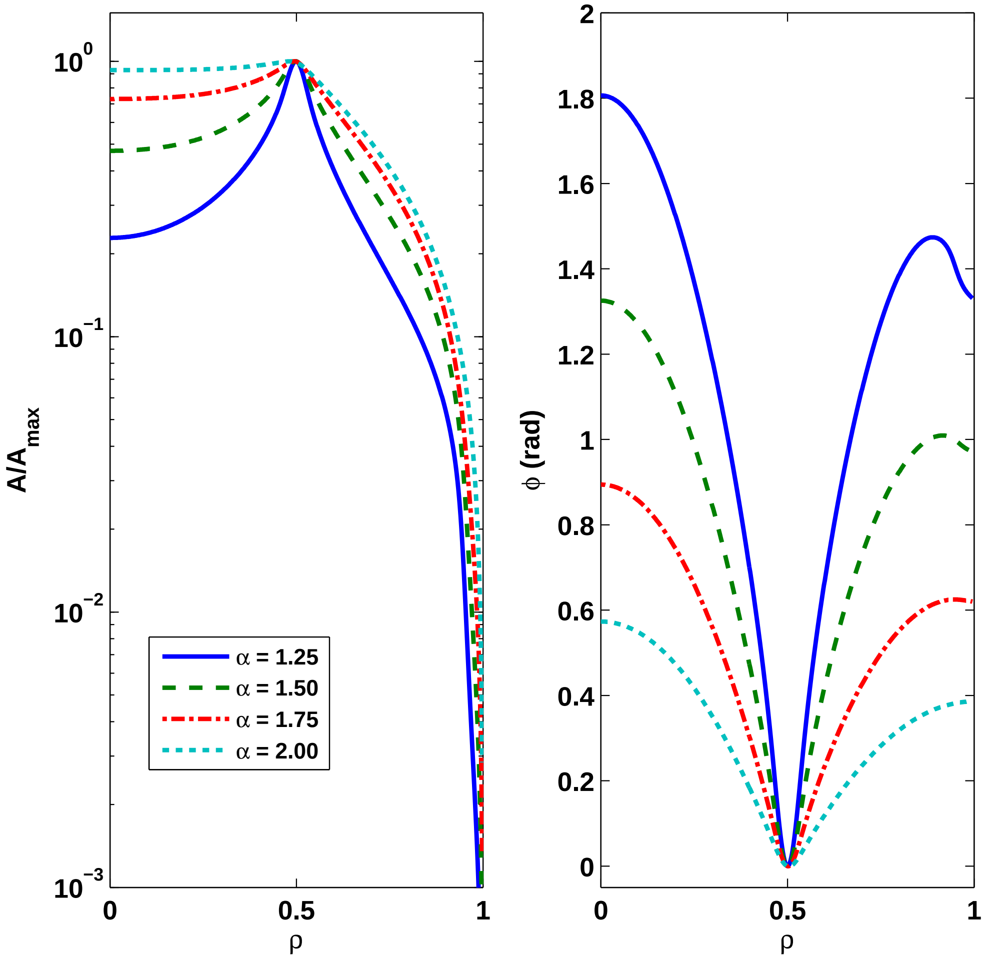

Figure 3.11: Radial profiles of amplitude and phase for fractional thermal waves described by equations (3.73) and (3.75). The plotted amplitudes have been normalized to their peak values. The calculations shown use an angular modulation frequency of $\omega = 10\,\tilde{\chi}_\alpha$ and a source width of $\sigma_S = 0.025$. As α decreases, both the amplitude and phase profiles become narrower.

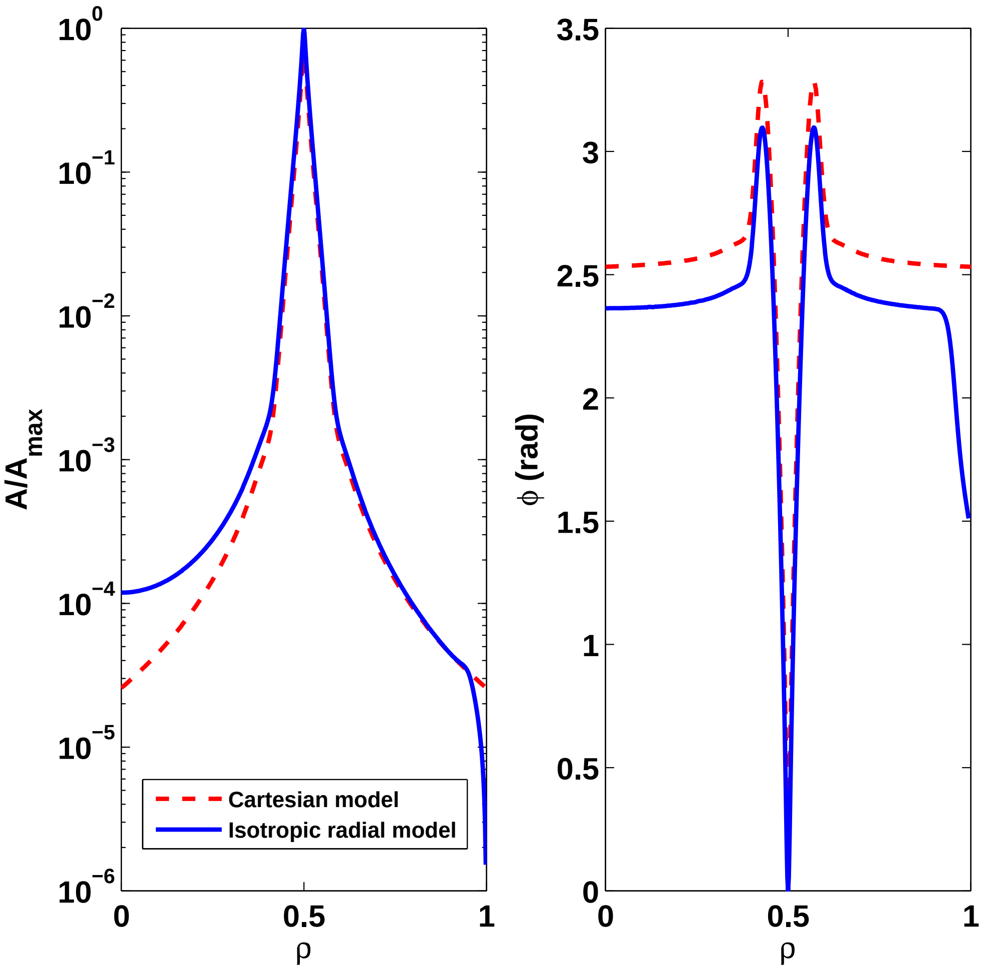

Figure 3.12: Comparison of radial fractional thermal waves to 1D Cartesian thermal waves in an unbounded domain. The radial model calculations use equations (3.73) and (3.75) with a source width of $\sigma_S = 0.0035$. The curves for the 1D profiles come from the exact solution given in equation (4.20). For both models, the amplitudes have been normalized to their peak values, the fractional order is $\alpha = 1.5$, and the power modulation frequency is $\omega = 1000\,\tilde{\chi}_\alpha$. As in the Cartesian model (dashed red line), the phase associated with the radial model (solid blue line) has peaks near the source that indicate the presence of an inwardly traveling component in the radial thermal wave that is interfering with an outwardly traveling component. This inwardly traveling part can be identified as the radial analogue to the 1D anomalous H functions reported in equation (4.21).

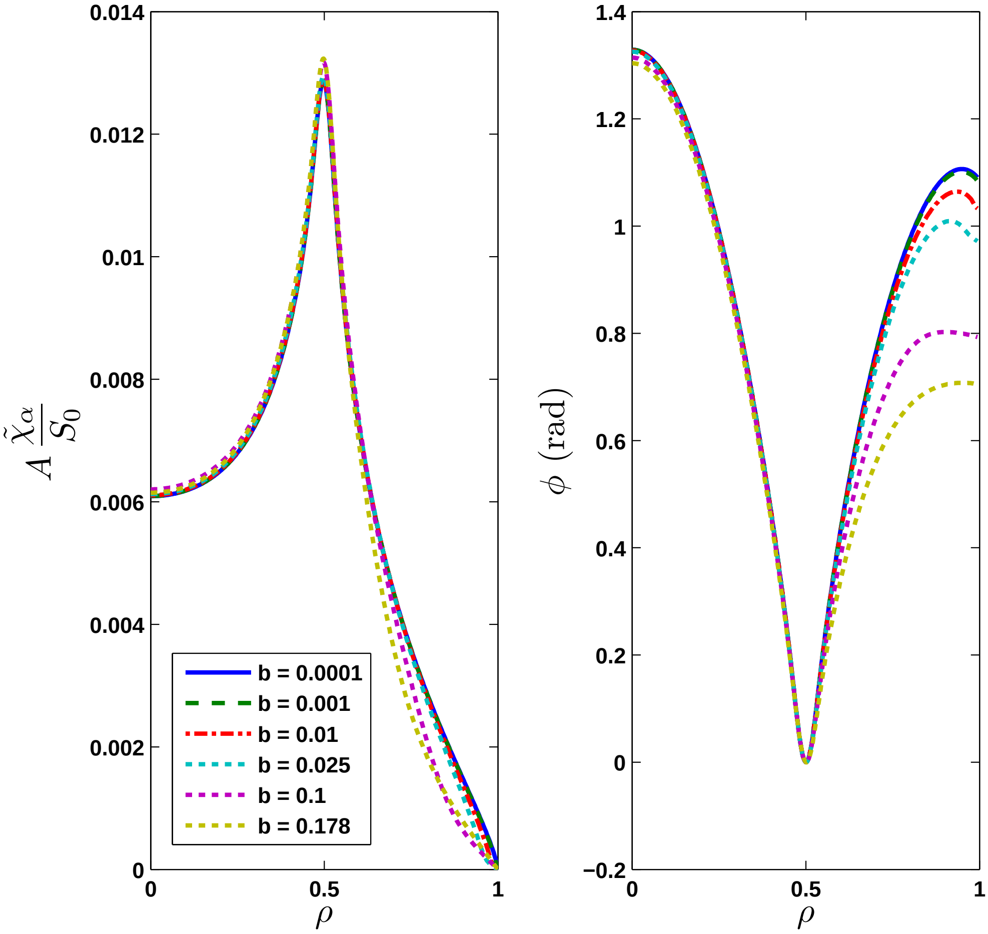

Figure 3.13: Radial profiles of amplitude and phase for different boundary layer widths b. The profiles are found from equations (3.73), (3.75), and (3.76). The parameters used in this calculation are as follows: $\alpha = 1.5$, $\omega = 10\,\tilde{\chi}_\alpha$, $\tilde{\zeta} = 1$, and $\sigma_S = 0.025$. As the boundary layer width b decreases, the amplitude and phase of the thermal waves converge to an asymptotic shape (note that the $b = 10^{-4}$ and $b = 10^{-3}$ curves overlap). For other values of ζ, taking $b \to 0$ produces the same asymptotic amplitude and phase curves shown here.

author's knowledge, no equivalent methodology has been developed that allows the evaluation of important physical systems that exhibit these properties. Prior investigations of fractional transport of such 2D systems have been based on the judicious application of 1D fractional formalisms that utilize an ad-hoc localization to avoid the behavior near the origin and at the outer boundary. The methodology developed in this Chapter should facilitate the investigation of various physical systems of contemporary interest, notably the modeling of non-local, anomalous transport in magnetic confinement devices used in fusion research.

To arrive at a formulation of fractional diffusion that can be applied to actual physical systems, it is necessary to implement a procedure that overcomes an inherent singularity at the boundary. The present work in this Chapter proposes a physically-motivated approach inspired by analogous situations encountered in plasmas, namely the development of a sheath or boundary layer. Since no rigorous theory has yet been developed that obtains the details of such a sheath, or of the general fix for the singularity, a simple Gaussian shape has been used for the mask function. The width and diffusion strength are chosen empirically to result in minimal sensitivity of the results in the interior of the computation domain. Figure 3.4 quantifies the sensitivity of calculated average temperatures on the two parameters that enter into the mask function; it provides guidance for future applications of the procedure.

In Chapter 5, the radial fractional model developed here is applied to steady off-axis heating experiments and power modulation experiments performed in different tokamak devices. In that survey, the hollow profiles associated with the radial fractional model are compared to observed profiles seen in steady off-axis heating experiments performed in the Rijnhuizen Tokamak Project (RTP) [BBH99]. For spatially uniform χ_α, there is good agreement between the fractional model results and the RTP experimental results. In the formulation presented in this Chapter, off-axis heating can produce a peaked temperature profile (as occurs in the time-average temperature profiles observed in the power modulation experiments) when the χ_α acquires certain spatial dependencies.

Following the same line of logic presented here for two dimensions, it is also possible to derive a 3D fractional Laplacian. When this operator is expanded in spherical harmonics, a hierarchy of fractional transport equations in r is again obtained in which the kernels are parametrized in the mode numbers l and m. Solving this set of equations allows one to describe fractional transport in the polar and azimuthal directions. The $l = 0$, $m = 0$ diffusion equation describes the spherically averaged radial fractional transport. In appendix C, the derivation of the 3D operator is briefly described, and the 3D operator and its expansion in spherical harmonics is given. However, no applications of the 3D formalism have yet been explored.

CHAPTER 4

Fractional thermal waves in one dimension

4.1 Introduction

An important topic relating to fractional diffusive transport is the nature of the thermal waves generated from a fractional diffusion process, and the behavior of fractional thermal waves in finite-sized resonator cavities. In the case of conventional diffusion, thermal waves are exponentially damped, or evanescent, with complex wave numbers k that are set by a dispersion relation

$$-i\omega = -\chi_d k^2 \ , \tag{4.1}$$

where χ_d is the conventional diffusivity and ω is the angular frequency of the modulated heat source. When conventional thermal waves are produced in a bounded cavity, resonant frequencies, which maximize some component of the temperature signal, can be found and used to measure the heat diffusivity χ_d of the system (see, e.g., Ref. [SM94]). Such a procedure requires the knowledge of a resonator condition, derived from a dispersion relation and a standing wave resonance condition, that relates the resonance frequency to the diffusivity χ_d.

In this Chapter, exact analytic solutions to the fractional thermal wave problem in the infinite domain are presented. These solutions are obtained from the one-dimensional fractional diffusion equation with Cartesian Riemann-Liouville fractional derivatives on the infinite range. Depending on the asymmetry of the system, it is found that the fractional thermal waves consist of two parts: an evanescent wave-like contribution, with wave numbers k set by a fractional dispersion relation, and an extra algebraically decaying contribution (labeled the H function), with wave-like behavior near the source. The application of these infinite domain solutions to a fractional resonator problem is also briefly discussed.

4.2 Analytic solutions of the fractional thermal wave equation

The investigation of fractional thermal waves in the infinite domain starts with the following equation

$$-i\omega\, T = \chi_\alpha\, \left[l\; {}_{-\infty}D_x^\alpha + r\; {}_xD_\infty^\alpha\right]\, T + \chi_d\, \frac{\partial^2}{\partial x^2}\, T + \delta(x)\ . \tag{4.2}$$

This equation describes the temperature response T of a single Fourier component in time due to an oscillating, localized, heat source at unit strength at the origin. Note that in equation (4.2) the operators ${}_{-\infty}D_x^\alpha$ and ${}_xD_\infty^\alpha$ are the left and right Riemann-Liouville operators, respectively, and that l and r are asymmetry weights given by (cf. (2.6))

$$l = -\frac{1-\theta}{2\cos(\alpha\pi/2)}, \quad r = -\frac{1+\theta}{2\cos(\alpha\pi/2)}\ . \tag{4.3}$$

The fractional thermal wave equation (4.2) can be solved by applying a Fourier transform in x; the resultant expression for T is

$$T(x) = \frac{1}{2\pi}\int_{-\infty}^{\infty} \frac{\exp\,(ikx)}{-i\omega - \Lambda(k)}\,\mathrm{d}k\ , \tag{4.4}$$

where $\Lambda(k)$ is given by

$$\Lambda(k) = \chi_\alpha\, \left[l\,(ik)^\alpha + r\,(-ik)^\alpha\right] - \chi_d\, k^2\ . \tag{4.5}$$

Note that to derive equation (4.4), the following convention for the Fourier transform is used

$$T(x) = \frac{1}{2\pi}\int_{-\infty}^{\infty} \tilde{T}(k)\, \exp(ikx)\,\mathrm{d}k \qquad \tilde{T}(k) = \int_{-\infty}^{\infty} T(x)\, \exp(-ikx)\,\mathrm{d}x\ , \tag{4.6}$$

for which the transforms of the fractional derivatives are

$$\mathcal{F}\left[{}_{-\infty}D_x^\alpha\, T(x)\right] = (ik)^\alpha\, \tilde{T}(k) \qquad \mathcal{F}\left[{}_xD_\infty^\alpha\, T(x)\right] = (-ik)^\alpha\, \tilde{T}(k)\ . \tag{4.7}$$

The above Fourier transforms of the left and right fractional derivatives are complex conjugates of the expressions given in equation (2.4) in Chapter 2, which use the conjugate convention for the transforms.

The integral in equation (4.4) can be performed by carefully applying the residue method. In particular, it must be observed that the function $\Lambda(k)$ is *not analytic* over the entire complex plane, and that evaluating the integral in (4.4) requires splitting the range of integration and applying the method separately to the parts of the integral that lie in the left ($\Re(k) < 0$) and right ($\Re(k) > 0$) half-planes. To understand this point, note that the function $\Lambda(k)$ given in (4.5) is only unambiguously defined for real k, in which case $\Lambda(k)$ must reduce to

$$\Lambda(k) = \chi_\alpha\, \left[l\, \exp(i\alpha\pi\, \mathrm{sign}(k)/2) + r\, \exp(-i\alpha\pi\, \mathrm{sign}(k)/2)\right]\, |k|^\alpha - \chi_d\, k^2\ . \tag{4.8}$$

Any analytic continuation of $\Lambda(k)$ in any part of the complex plane must use branches of the $(\pm ik)^\alpha$ functions that reproduce equation (4.8) on the real axis. For example, it should be observed that the seemingly plausible method of factoring out the common k^α term is *incorrect* (see below):

$$\Lambda(k) \overset{?}{=} \chi_\alpha\, \left[l\, \exp(i\alpha\pi/2) + r\, \exp(-i\alpha\pi/2)\right]\, k^\alpha - \chi_d\, k^2\ , \tag{4.9}$$

Assuming that the branch of k^α used in equation (4.9) takes the value $(-1)^\alpha = \exp(i\alpha\pi)$, equation (4.9) gives the following expression for $\Lambda(k)$ with negative k

$$\Lambda(-|k|) \overset{?}{=} \chi_\alpha\, \left[l\, \exp(3i\alpha\pi/2) + r\, \exp(i\alpha\pi/2)\right]\, |k|^\alpha - \chi_d\, k^2\ . \tag{4.10}$$

This is in disagreement with equation (4.8) since the phase of the l term is off by $\pi\alpha$. Other branches of k^α also fail to reproduce equation (4.8). In order for $(ik)^\alpha = i^\alpha\, k^\alpha = \exp(i\pi\alpha/2)\, k^\alpha$ to reduce to the correct value on the entire real axis, a branch of k^α must be chosen so that for negative real values $k^\alpha = |k|^\alpha\, \exp(-i\alpha\pi)$

and for positive real values $k^\alpha = |k|^\alpha$. This branch would require that the branch cut lie in the *upper half* of the complex plane. In contrast for $(-ik)^\alpha = (-i)^\alpha\, k^\alpha = \exp(-i\pi\alpha/2)\, k^\alpha$ to give the correct values requires that for negative real values $k^\alpha = |k|^\alpha \exp(i\alpha\pi)$ and for positive real values $k^\alpha = |k|^\alpha$. This branch would require that the branch cut lie in the *lower half* of the complex plane. If the following notation is introduced (which makes the complex polar angle θ_b of the branch cut explicit)

$$(z)^\alpha_{\theta_b} = |z|^\alpha \exp(i\alpha\phi_z) \text{ where } \phi_z \equiv \arg(z), \quad \theta_b - 2\pi < \phi_z \leq \theta_b \ , \tag{4.11}$$

then the correct factorization of the terms $(ik)^\alpha$ and $(-ik)^\alpha$, in light of equation (4.8), is as follows

$$l\,(ik)^\alpha + r\,(-ik)^\alpha = l\,(i)^\alpha_\pi\,(k)^\alpha_{\pi/2} + r\,(-i)^\alpha_\pi\,(k)^\alpha_{3\pi/2} \ . \tag{4.12}$$

In this expression, the l term has a branch cut located along the positive imaginary axis and the r term has a branch cut along the negative imaginary axis. When both terms are present there is no analytic continuation of $\Lambda(k)$ that connects the negative and positive real axes. The best that can be hoped for is the analytic continuation of $\Lambda(k)$ given by

$$\begin{aligned}\Lambda(k) &= -\chi_d\, k^2 + \chi_\alpha\,(k)^\alpha_{3\pi/2} \begin{cases} l\ \exp(i\pi\alpha/2) + r\ \exp(-i\pi\alpha/2), & \Re(k) > 0 \\ [l\ \exp(-i\pi\alpha/2) + r\ \exp(i\pi\alpha/2)]\exp(-i\pi\alpha), & \Re(k) < 0 \end{cases} \\ &= \begin{cases} \Lambda_+(k) & \Re(k) > 0 \\ \Lambda_-(k) & \Re(k) < 0 \end{cases} .\end{aligned} \tag{4.13}$$

In this formulation, $\Lambda(k)$ is separately analytic on the left and right half complex planes and has a line of discontinuity along the imaginary complex axis.

Using equation (4.13) as the correct analytic continuation, the integral (4.4) can be evaluated by dividing the integral into two parts

$$\begin{aligned} T(x) &= \int_{-\infty}^{0} g_-(x;k)\,\mathrm{d}k + \int_{0}^{\infty} g_+(x;k)\,\mathrm{d}k \\ &\equiv I_-(x) + I_+(x)\ , \end{aligned} \tag{4.14}$$

where

$$g_\pm(x;k) = \frac{1}{2\pi}\,\frac{\exp(ikx)}{-i\omega - \Lambda_\pm(k)}\ , \tag{4.15}$$

and applying the residue method on the left ($\Re(k) < 0$) and right ($\Re(k) > 0$) halves of the complex plane where $\Lambda(k)$ is separately analytic. When $x > 0$ this gives

$$\begin{aligned} &\int_{\epsilon}^{R} g_+(x;k)\,\mathrm{d}k + \underbrace{\int_{\Gamma_R^{(+)}} g_+(x;k)\,\mathrm{d}k}_{0 \text{ as } R\to\infty} + \int_{\epsilon+iR}^{\epsilon} g_+(x;k)\,\mathrm{d}k \\ &\qquad\qquad = -i\,\frac{\exp(ik_+\,x)}{\Lambda_+'(k_+)}\ , \\ &\int_{-R}^{-\epsilon} g_-(x;k)\,\mathrm{d}k + \underbrace{\int_{\Gamma_R^{(-)}} g_-(x;k)\,\mathrm{d}k}_{0 \text{ as } R\to\infty} + \int_{-\epsilon}^{iR-\epsilon} g_-(x;k)\,\mathrm{d}k \\ &\qquad\qquad = 0\ , \end{aligned} \tag{4.16}$$

for quarter-circle contours located in the upper half plane ($\Im(k) > 0$); see figure 4.1 for the explicit contours used. In obtaining (4.16), note that the dispersion relation $\Lambda_+(k) = -i\omega$ has at most one root which lies in the first quadrant of the complex plane.

In equations (4.16) when $R \to \infty$ and $\epsilon \to 0$ the first pair of terms reduce to $I_+(x)$ and $I_-(x)$, respectively. The second pair of terms, labeled with $\Gamma_R^{(\pm)}$, correspond to integration along a circular chord that connects $\pm R$ and $iR \pm \epsilon$. These terms go to zero due to the factor $\exp(ikx)$ in the integrand which decreases exponentially as $|k| \sim R \to \infty$ when $\Im(k)\,x > 0$. The contours are closed in the upper half plane when $x > 0$ in order to remove the contribution of this part of the contour to the total integral. However the third pair of terms–corresponding

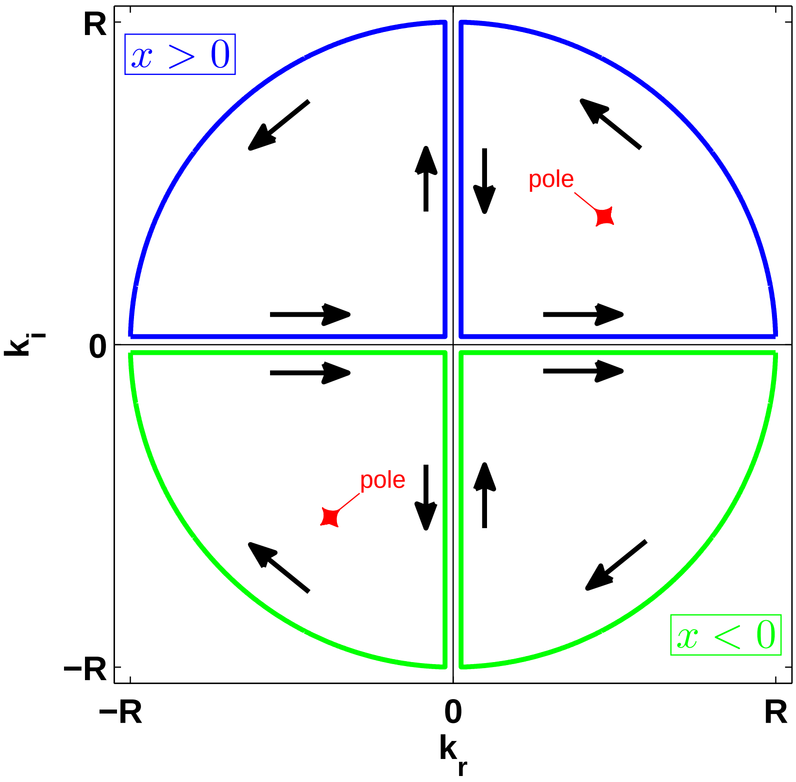

Figure 4.1: Closed contours used with residue method in equation (4.16). When $x > 0$, the blue contours are used and when $x < 0$ the green contours are used. Because of the line of discontinuity in $\Lambda(k)$ that exists along the imaginary axis, the integration is split between the $\Re(k) > 0$ or $\Re(k) < 0$ half-planes and each contour is closed as a quarter circle shape.

to the integration along the imaginary axis–do *not* disappear as $R \to \infty$ or $\epsilon \to 0$. These terms represent an extra and novel contribution to the expected evanescent wave term due wholly to the piecewise analytic topology of the fractional $\Lambda(k)$. When the above discussed limits are taken and the two equations in (4.16) are summed, the following expression for the solution is obtained

$$T(x) = -i\,\frac{\exp(ik_+x)}{\Lambda'_+(k_j)} + H_+(x) \qquad x > 0\ , \tag{4.17}$$

where

$$\begin{aligned} H_+(x) &= \int_0^{i\infty} [g_+(x;k) - g_-(x;k)]\ \mathrm{d}k \\ &= \frac{i}{2\pi}\int_0^{\infty} \exp(-x\,s)\ \left[\frac{1}{-i\omega - \chi_\alpha(l\ \exp(i\pi\alpha) + r)\, s^\alpha - \chi_d s^2} \right. \\ &\qquad \left. - \frac{1}{-i\omega - \chi_\alpha(l\ \exp(-i\pi\alpha) + r)\, s^\alpha - \chi_d s^2}\right] \mathrm{d}s\ . \end{aligned} \tag{4.18}$$

It should be noted that the k_+ that appears in the exponential of equation (4.16) and (4.17) is the root of the fractional dispersion relation

$$-i\omega - \Lambda_+(k_+) = 0\ , \tag{4.19}$$

with positive imaginary part.

A similar analysis can be performed when $x < 0$ by reflecting the contours across the real axis. When this contribution is included, the total solution is found to be

$$T(x) = \begin{cases} -i\,\dfrac{\exp(ik_+x)}{\Lambda'_+(k_+)} + H_+(x) & x > 0 \\ i\,\dfrac{\exp(ik_-x)}{\Lambda'_-(k_-)} + H_-(x) & x < 0\ , \end{cases} \tag{4.20}$$

where

$$\begin{aligned} H_\pm(x) &= \frac{i}{2\pi}\int_0^{\infty} \exp(-|x|s)\ \left[\frac{1}{-i\omega - \chi_\alpha\, c_\pm\, s^\alpha - \chi_d\, s^2} - \frac{1}{-i\omega - \chi_\alpha\, c_\pm^*\, s^\alpha - \chi_d\, s^2}\right] \mathrm{d}s \\ c_+ &= l\ \exp(i\pi\alpha) + r \qquad c_- = l + r\ \exp(i\pi\alpha)\ , \end{aligned} \tag{4.21}$$

and where k_- is the root of the dispersion relation:

$$-i\omega - \Lambda_-(k_-) = 0 \ , \tag{4.22}$$

with negative imaginary part.

For large $|x|$, Watson's lemma can be used to obtain an asymptotic expression for the $H_\pm(x)$ functions:

$$H_\pm(x) \sim \frac{\Im(c_\pm)\,\Gamma(\alpha+1)\,\chi_\alpha}{\pi\,\omega^2\,|x|^{\alpha+1}} + \frac{2i\Im(c_\pm)\,\chi_\alpha}{\pi\,\omega^3}\left[\frac{\Re(c_\pm)\,\Gamma(2\alpha+1)\,\chi_\alpha}{|x|^{2\alpha+1}} + \frac{\chi_d\,\Gamma(\alpha+3)}{|x|^{\alpha+3}}\right] . \tag{4.23}$$

The H functions decay algebraically such that the second moments of the solution are infinite, i.e., $\langle x^2 \rangle > \infty$. This divergence of the second moment is a characteristic of the Lévy statistics that describe fractional diffusion processes, and of the fractional Green's function (cf. [Cas06]). The presence of the H functions in the total solution then is necessary to preserve the infinite second moments associated with fractional diffusion. Figure 4.2 shows the amplitude and phase profiles of the H functions for symmetric ($\theta = 0$) fractional transport with no conventional diffusion ($\chi_d = 0$). The slope of the phase profiles near the source indicate that the H functions represent an inwardly traveling wave; that is, the H functions are a "reflection" from infinity due to the non-local nature of fractional diffusion. These inwardly traveling H functions can interfere with the evanescent part of the total solutions to produce peaks in the phase profiles–see figure 4.3.

Figure 4.3 plots the total solutions for different α's and with $\theta = 0$. The amplitudes of the symmetric thermal waves exhibit exponential decay near the source and then transition into algebraic decay farther away from the source; the crossover between the two regimes occurs around $x(\omega/\chi_\alpha)^{1/\alpha} = 10$. As mentioned earlier, the phase for $\alpha < 2.00$ has hills, or local maximums, as a result of the inwardly traveling H functions that interfere with the outwardly traveling evanescent waves described by the dispersion relation. Figure 4.4 plots the amplitude and phase of the thermal waves for different levels of asymmetry and for the fractional order $\alpha = 1.25$. For the values of $\theta > 0$ chosen, the leftward moving wave has been eliminated and the temperature perturbation to the left of the source is entirely determined by the $H(x)$ function. Note that in these asymmetric cases ($\theta \neq 0$), the $H(x)$ function is outwardly traveling for $x < 0$. As $\theta \to 1$, the magnitude of the $H_+(x)$ contribution on the right side decreases, resulting in a purely exponential solution for $x > 0$ when $\theta = 1$.

4.3 Roots of the dispersion relation

The roots of the dispersion relations (4.19) and (4.22) can be found analytically for the purely fractional case ($\chi_d = 0$). When no conventional diffusion is present, the dispersion relation can have one or two roots depending on the asymmetry θ of the fractional transport and the fractional order α. For large enough θ, asymmetric fractional diffusion can remove one root for low $\alpha < 1.5$ (cf. figure 4.5). Recalling equation (4.13), roots with $\Re(k) > 0$ satisfy the relation

$$\begin{aligned} -i\omega - \chi_\alpha \left[l\, e^{i\pi\alpha/2} + r\, e^{-i\pi\alpha/2} \right] (k)^\alpha_{3\pi/2} &= 0 \\ \Rightarrow (k)^\alpha_{3\pi/2} &= \frac{i\omega}{\chi_\alpha \left[1 - i\theta \, \tan(\alpha\pi/2) \right]} \ . \end{aligned} \tag{4.24}$$

If $\phi = \mathrm{Arg}(1 - i\theta \, \tan(\alpha\pi/2))$, where $|\mathrm{Arg}(z)| \leq \pi$, then equation (4.24) can be rewritten as

$$(k)^\alpha_{3\pi/2} = \frac{\omega}{\chi_\alpha \sqrt{1 + \theta^2 \, \tan^2(\alpha\pi/2)}} \exp(-i\phi + i\,\pi/2) \ . \tag{4.25}$$

Since the branch $(k)^\alpha_{3\pi/2}$ maps the $\Re(k) > 0$ half-plane into a sector of the complex plane that lies between the complex polar angles $[-\alpha\pi/2,\ \alpha\pi/2]$, equation (4.25) only has a root if the complex argument of the right hand side is in $[-\alpha\pi/2,\ \alpha\pi/2]$. In other words, a rightward moving wave ($\Re(k) > 0$) only exists if $-\alpha\pi/2 < -\phi + \pi/2 < \alpha\pi/2$. If this condition is met, then the wave number is

$$k_+ = \left[\frac{\omega}{\chi_\alpha \sqrt{1 + \theta^2 \, \tan^2(\alpha\pi/2)}} \right]^{1/\alpha} \exp\left[-i\phi/\alpha + i\,\pi/(2\alpha) \right] \ . \tag{4.26}$$

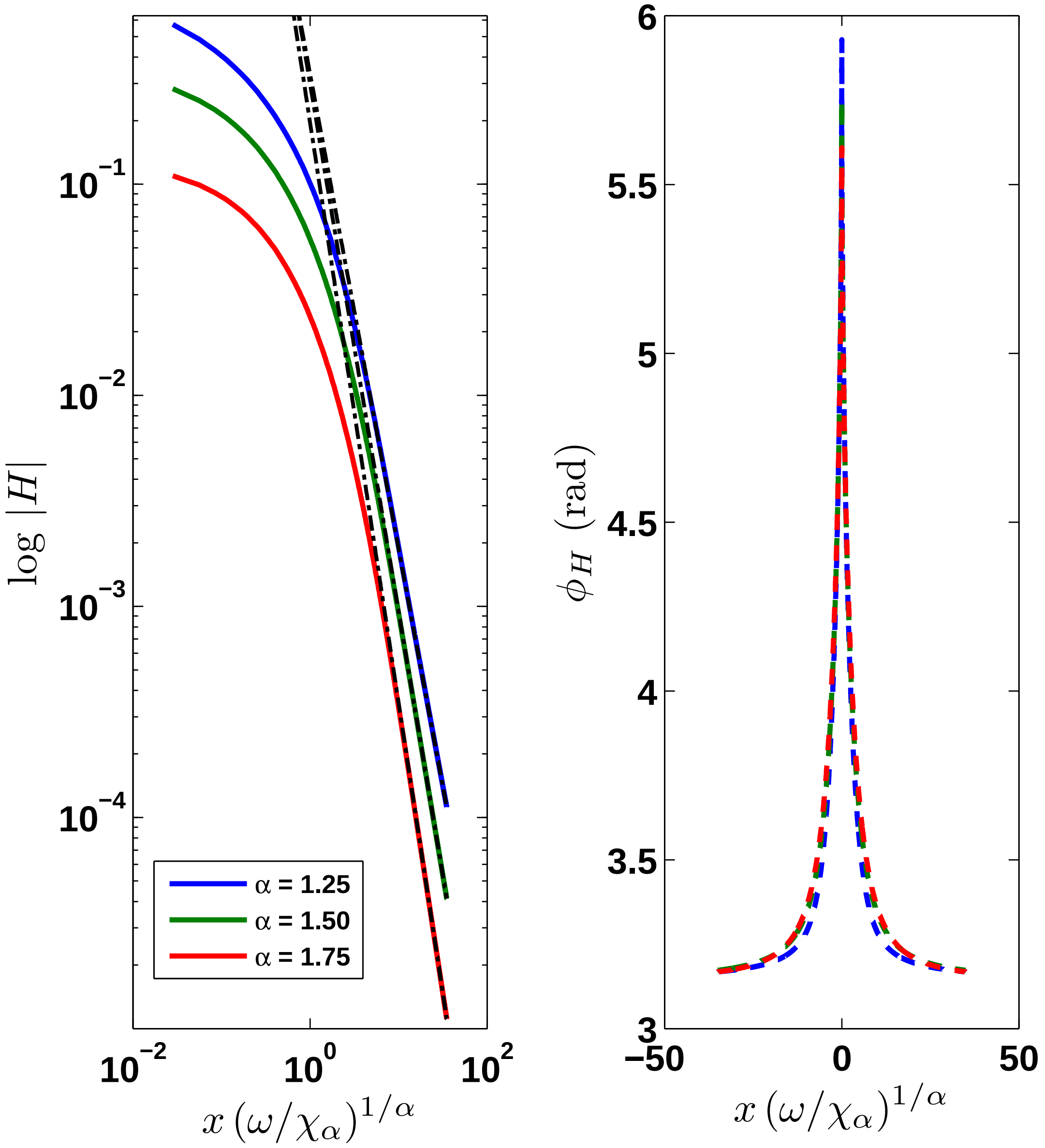

Figure 4.2: Amplitude and phase of the algebraically decaying H functions for $\theta = 0$ and $\chi_d = 0$. The black dashed-dot curves are found from the leading order term of the asymptotic expansion (4.23) for each α. The slope of the phase profiles indicate that near the source the H functions represent inwardly traveling waves.

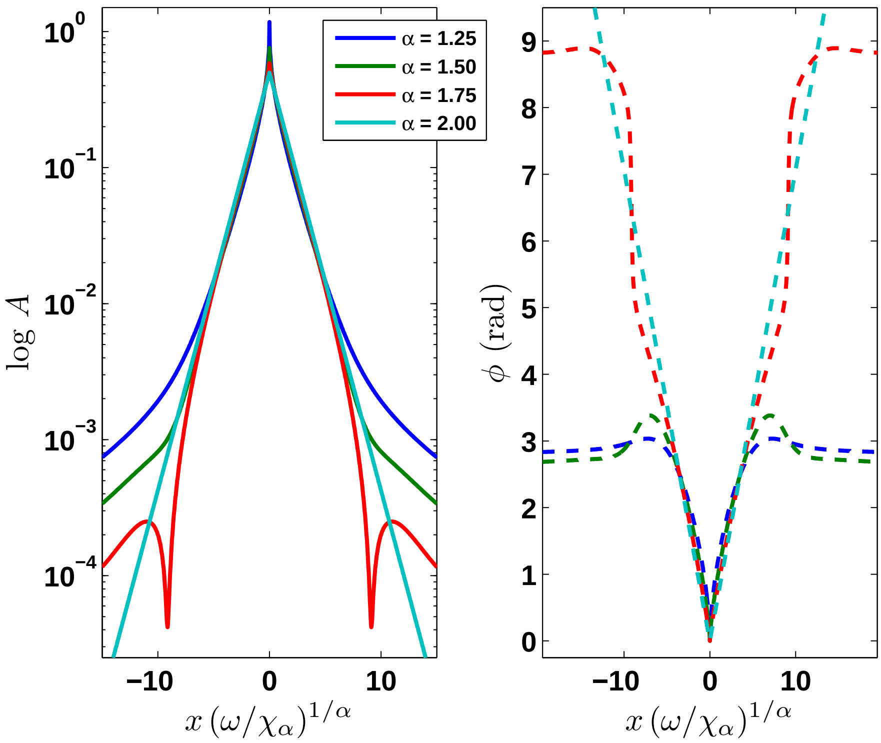

Figure 4.3: Amplitude and phase of fractional thermal waves for $\theta = 0$ and $\chi_d = 0$.

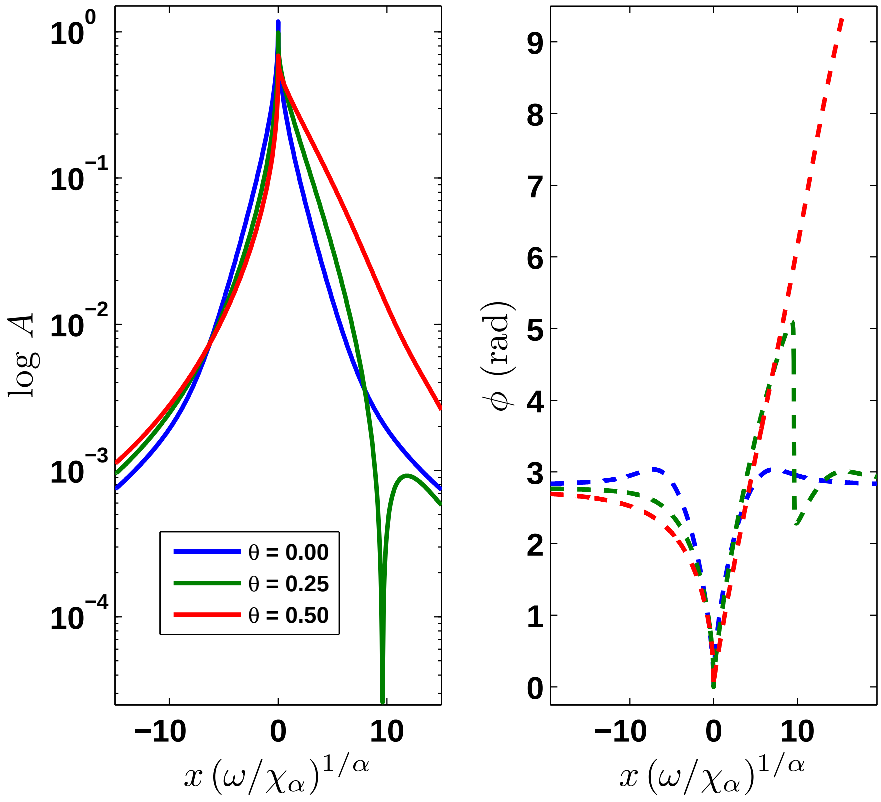

Figure 4.4: Amplitude and phase of fractional thermal waves for $\alpha = 1.25$ and $\chi_d = 0$. For $\theta > 0.172$, the leftward moving wave disappears (cf. figure 4.5). For the $\theta > 0$ cases shown, the temperature perturbation to the left of the source is described solely by the contribution of the $H_-(x)$ function.

Note that this wave number has a positive imaginary part since $|\phi| < \pi/2$ for all θ and α, and is therefore the wave number for the the wave part of the solution that appears to the right of the source.

The $\Re(k) < 0$ root is found from the relation

$$\begin{aligned} -i\omega - \chi_\alpha \left[l\, e^{-i\pi\alpha/2} + r\, e^{i\pi\alpha/2} \right] e^{-i\pi\alpha}\, (k)^\alpha_{3\pi/2} = 0 \ , \\ \Rightarrow (k)^\alpha_{3\pi/2} = \frac{\omega}{\chi_\alpha \sqrt{1+\theta^2\, \tan^2(\alpha\pi/2)}} \exp\left[i(\pi\alpha + \phi + \pi/2)\right] \ , \end{aligned} \tag{4.27}$$

where again $\phi = \mathrm{Arg}\left[1 - i\theta \tan(\alpha\pi/2)\right]$. This root exists if the complex angle of the right-hand side lies in the interval $[\alpha\pi/2,\ 3\alpha\pi/2]$. In other words, the leftward moving wave exists if $\alpha\pi/2 < \alpha\pi + \phi + \pi/2 < 3\alpha\pi/2$. When this condition is met, the leftward wave number is given by

$$k_- = \left[\frac{\omega}{\chi_\alpha \sqrt{1+\theta^2\, \tan^2(\alpha\pi/2)}} \right]^{1/\alpha} \exp\left[i(\pi + \phi/\alpha + \pi/(2\alpha))\right] \ . \tag{4.28}$$

This wave number has a negative imaginary part for all α and θ, and corresponds to the wave number of the solution to the left of the source. When $\theta = 0$ and $\phi = 0$, this root is the negative of the rightward-moving wave number:

$$k_- = -k_+, \quad \text{when} \ \ \theta = 0 \ . \tag{4.29}$$

Figure 4.5 shows the regions in the parameter space of α and θ for which the left and right propagating wave numbers exist. When $\alpha < 1.5$, high asymmetry can remove one of the roots, depending on the sign of θ. Large positive values of θ, for example, eliminates the leftward moving wave number as a root of the dispersion relation.

4.4 Exploration of a fractional thermal wave resonator

One motivation for finding analytic solutions to the fractional thermal wave equation (4.2) is their potential application to a thermal wave resonator situation. In

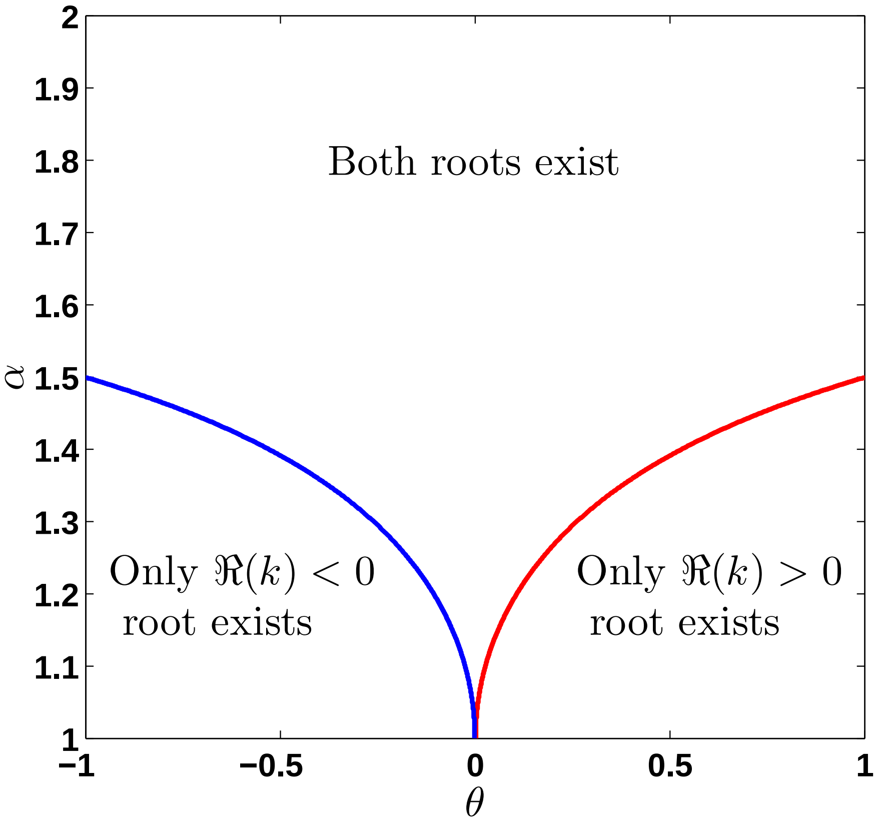

Figure 4.5: Values of α and θ for which the dispersion relation (4.19) has leftward and rightward moving waves. When $\alpha > 1.5$, both wave numbers exist for any θ, and when $\theta = 0$ both waves exist for all α. However as α drops below 1.5, increasing the asymmetry parameter θ removes one of the roots. In the region of parameter space below the red curve, positive values of θ lead to the disappearance of the leftward moving wave ($\Re(k) < 0$). In the region below the blue curve, negative values of θ eliminate the rightward moving wave ($\Re(k) > 0$).

particular it is presumed that knowledge of the infinite domain solutions would allow one to predict, from the fractional dispersion relation, a resonance condition that connects a characteristic resonance frequency with the fractional transport parameters α and χ_α. This relation would allow for development of an experiment that could clearly indicate the presence of fractional transport and also allow for the measurement of α and χ_α. For example, in systems that are described by conventional diffusion, it is possible to measure the heat diffusivity χ_d of a medium in a cavity (e.g. see Ref. [SM94]) by finding either the frequency ω or the cavity length L that maximizes the quadrature signal of the thermal wave at the end of the cavity. The diffusivity χ_d is found from ω and L from the resonance condition

$$\omega = 2\chi_d \left(\frac{\pi n}{L}\right)^2 \quad n = 1, 2, 3, \dots\ , \tag{4.30}$$

which corresponds to fitting an integral number of half-wavelengths in the cavity length L.

Exploration of several different fractional thermal resonator models has found that the resonance response depends strongly on the finite domain model of fractional transport considered and on the handling of the boundary conditions. Moreover, when these boundary effects dominate, it is difficult to connect the infinite domain solutions, and the fractional dispersion relation (4.19) to the fractional thermal wave solutions in a finite domain. For example, one model of a fractional resonator can be formed by considering a finite region of space in which transport is described by Caputo fractional derivatives and which impinges on a region of purely conventional diffusion. For boundary conditions that assume that the temperature of the modulations and the heat flux are continuous across the interface, it is found that the thermal wave amplitude at the media interface (i.e., the end of the cavity) is *larger* than at the modulated power source when the fractional diffusivity χ_α is large. This response is unphysical, and is dominated by a spurious boundary flux term that appears in the definition of the Caputo fractional derivative.

Another model of a 1D fractional thermal resonator, which avoids unphysical large amplitudes at the cavity edge, can be formed using Riemann-Liouville fractional derivatives. In this model, the singularities associated with the Riemann-Liouville operators in a finite domain are removed with mask functions and diffusivities χ_α that go to zero at the boundaries. For a given mask function, it is found that the quadrature part of the fractional thermal wave, at the cavity edge, has a maximum amplitude at a characteristic resonance frequency. The resonance frequency defined in this way has an asymptotic dependence the boundary layer parameters; that is, as the strength of the boundary layer diffusion decreases and the boundary layer width decreases, the resonance frequency approaches an asymptotic value (this is a result of the fact that the thermal wave amplitude and phase profiles approach asymptotic curves for each ω as the boundary layer parameters are reduced–see, for example, figure 3.13). However, this resonance frequency cannot be predicted from considerations of the fractional dispersion relation and a standing wave resonance condition. Moreover, the dependence of the fractional quadrature signal on the driving modulation frequency ω is qualitatively similar to the dependence exhibited by a conventional diffusive system. This makes it impossible to distinguish, from the quadrature signal at a single point, between a system described by fractional diffusive transport and one described by conventional diffusive transport.

4.5 Conclusion

This Chapter describes the analytic expression for fractional thermal waves in the infinite domain. These waves are solutions of the one dimensional fractional diffusion equation with Riemann-Liouville fractional derivatives. From these solutions it is learned that fractional thermal waves are composed of two parts: an evanescent wave-like component and an algebraically decaying component. The wave-like component has complex wave numbers determined by a fractional dispersion relation. For symmetric diffusion, both left and rightward moving wave numbers are present. For asymmetric diffusion with $\alpha < 1.5$, either the left or right root of the dispersion relation can disappear, depending on the sign and magnitude of the asymmetry parameter θ. The second component of the total solution–the H function–decays algebraically so that the second moment of the thermal wave solution diverges. This divergence of the moments is a characteristic of the Lévy statistics that describe fractional diffusion, and the presence of the H function reflects this aspect of fractional diffusion.

The infinite domain fractional thermal wave solutions have limited application to a fractional resonator situation. Fractional thermal waves in a finite-size cavity are strongly influenced by which bounded domain model of fractional diffusion is chosen. When a masked Reimann-Liouville model is used, the resonance frequencies asymptotically approach a constant value as the boundary layer width, and boundary diffusion strength go to zero. However, as of yet, no analytic condition for a fractional thermal resonance has been found that allows for the clear identification of fractional transport and the measurement of the parameters α or χ_α.

CHAPTER 5

Comparison of the 2D fractional transport model to tokamak experiments

5.1 Introduction

The main goal of this Chapter is to compare results obtained from the radial fractional model to experimental results from several different tokamak devices. In particular this survey focuses on experimental results from the following devices: Rijnhuizen Tokamak Project (RTP), ASDEX-Upgrade, JET, and DIII-D.

These comparisons are made with the pure fractional model; that is, it should be emphasized that the philosophy of the present study consists of isolating, in its purest form, the results of a radial fractional transport model and comparing them against expectations based solely on a Fick's law transport model. This approach is to be contrasted to a modeling exercise in which best fits to experimental observations are obtained by judicious mixtures of fractional transport and Fick's law transport at different radial positions.

In RTP steady-state temperature profiles have been observed that exhibit a centrally hollow shape similar to profiles that are an intrinsic feature of the radial fractional model. Thus, it is pertinent to explore if the radial fractional model can adequately reproduce these measured hollow profiles. With regards to ASDEX-Upgrade, JET, and DIII-D, this survey applies the fractional model to off-axis power modulation experiments performed in those devices. These devices are chosen because the equilibrium temperature profiles for each specific modulation experiment are readily available in the literature. These equilibrium profiles are needed to obtain the fractional diffusivities used in solving the fractional model numerically.

5.2 Experimental comparison

This section explores applications of the radial fractional model to experiments performed in several different tokamak devices. The choice of specific devices for study is determined by the availability of sufficiently detailed information in the open literature, since the data used for comparisons is digitally extracted [HS12] from published graphs. Based on this criterion, comparisons are made to steady off-axis heating experiments performed in RTP [BBH99], and to off-axis power modulation experiments performed in ASDEX-Upgrade [IRG01], JET [MCG08], and DIII-D [DPW12, HDP13].

The following discussion focuses on the numerical solutions found from the bounded domain transport equation that is formed when the fractional flux expression

$$q_\alpha(r) = -n_e(r)\,\chi_\alpha(r)\left[\frac{\partial}{\partial r}\int_0^a r'\,K_\alpha(r,r')\,H_\alpha(r')\,T(r')\,\mathrm{d}r' + \zeta\,\left(1 - H_\alpha(r)\right)\frac{\partial}{\partial r}T(r)\right], \tag{5.1}$$

is substituted into a continuity equation (cf. equation 3.48). As in Chapter 3, the mask function used in the calculations presented here is given by

$$H_\alpha(r) = 1 - \exp\left[-\left(\frac{r-a}{b}\right)^2\right]. \tag{5.2}$$

Also note that in (5.1) and in this Chapter the fractional diffusivity $\chi_\alpha(r)$ is allowed to vary spatially; in Chapter 3, $\chi_\alpha(r)$ is assumed constant.

When the bounded domain flux given by equation (5.1) is inserted into a fluid-like continuity equation, the resulting transport equation for the electron temperature T is,

$$\frac{3}{2}\frac{\partial}{\partial t}\left(n_e(r)\,T(r,t)\right) = \frac{1}{r}\frac{\partial}{\partial r}\left[r\,n_e(r)\,\chi_\alpha(r)\left(\frac{\partial}{\partial r}\int_0^a r'\,K_\alpha(r,r')\,H_\alpha(r')\,T(r',t)\,\mathrm{d}r' \right.\right.$$
$$\left.\left. +\zeta\,\left(1-H_\alpha(r)\right)\frac{\partial}{\partial r}T(r,t)\right)\right] + S(r,t)\ , \tag{5.3}$$

where n_e is the electron density and $S(r,t)$ is the power density associated with the heating source. The radial fractional diffusion equation given in (5.3) can be solved numerically using a discretization scheme for the radial fractional operator given in appendix B. In the following sections, numerical solutions of equation (5.3) are compared to experimental measurements from various tokamak devices. It is to be noted that no explicit terms are included to describe radiation losses nor energy exchange with ions which are common features of these devices. Also, convective heat fluxes, or heat pinch effects, are not included. Finally, throughout this work, the electron plasma density is normalized to a characteristic value $\bar{n}_e$ and is written $n_e(\rho) = \bar{n}_e\,N(\rho)$. For some calculations $N(\rho) = 1$; otherwise, appropriate density profiles are taken from the reported literature.

In the power modulation experiments of interest, the input power is a square wave modulated at a fixed frequency, f_{mod}, so that it is convenient to write the time dependent temperature as a Fourier series,

$$T(r,t) = \sum_{m=-\infty}^{\infty} \exp\left(-i\omega m t\right)\,T^{(m)}(r)\ , \tag{5.4}$$

where $\omega = 2\pi f_{mod}$ is the angular modulation frequency. Also, to facilitate the comparison to experiment, the following normalized variables are introduced,

$$\begin{gathered}\rho = \frac{r}{a}, \qquad \tilde{\chi}_\alpha(\rho) = \frac{\chi_\alpha(\rho)}{a^\alpha}, \qquad \tilde{\zeta} = \frac{\zeta}{a^{2-\alpha}}\ , \\ \tilde{S}_m(\rho) = \frac{\omega}{2\pi}\int_0^{2\pi/\omega} \exp\left(i\omega m t\right)\frac{S(\rho,t)}{\bar{n}_e}\,\mathrm{d}t\ .\end{gathered} \tag{5.5}$$

In this scaling, ω and $\tilde{\chi}_\alpha$ have units of Hz, $T^{(m)}$ has units of keV, and $\tilde{S}_m$ has units of keV/sec. Recall that $\bar{n}_e$ refers to the characteristic magnitude of the electron density. In terms of scaled variables, (5.3) becomes an equation for the m-th frequency harmonic

$$\begin{aligned}-\frac{3}{2}i\omega m N(\rho)\,T^{(m)}(\rho) = \frac{1}{\rho}\frac{\partial}{\partial\rho}\Bigg[\rho\,N(\rho)\,\tilde{\chi}_\alpha(\rho)\,\bigg(\frac{\partial}{\partial\rho}\int_0^1 \rho'\,K_\alpha(\rho,\rho')\,H_\alpha(\rho')\,T^{(m)}(\rho')\,\mathrm{d}\rho' \\ +\tilde{\zeta}\,\left(1-H_\alpha(\rho)\right)\frac{\partial}{\partial\rho}T^{(m)}\bigg)\Bigg] + \tilde{S}_m(\rho)\ .\end{aligned} \tag{5.6}$$

The steady-state temperature profile (the case in which $\frac{\partial}{\partial t}T = 0$) is then the $m = 0$ component of the series in (5.4), $T^{(0)}$. In the comparisons presented in the next section, the results for conventional diffusion are also presented and labeled as $\alpha = 2.0$. In practice, these solutions are obtained using

$$-\frac{3}{2}\,i\,\omega\,m\,N(\rho)\,T^{(m)}(\rho) = \frac{1}{\rho}\frac{\partial}{\partial\rho}\left[\rho\,N(\rho)\,\tilde{\chi}_2(\rho)\frac{\partial}{\partial\rho}\,T^{(m)}\right] + \tilde{S}_m(\rho) \quad \text{when } \alpha = 2.0\ . \tag{5.7}$$

When it is necessary to obtain an explicit functional form of the fractional diffusivity $\tilde{\chi}_\alpha$, it is obtained from the steady-state profile and the corresponding (normalized) steady-state heat flux $\tilde{q} = q/(a\,\bar{n}_e)$ (which is measured in keV/sec),

$$\begin{aligned}\tilde{\chi}_\alpha(\rho) = -\frac{\tilde{q}(\rho)}{N(\rho)} \times \bigg[\frac{\partial}{\partial\rho}\int_0^1 \rho'\,K_\alpha(\rho,\rho')\,H_\alpha(\rho')\,T^{(0)}(\rho')\,\mathrm{d}\rho' \\ +\zeta\,\left(1-H_\alpha(\rho)\right)\frac{\partial}{\partial\rho}T^{(0)}(\rho)\bigg]^{-1}\ .\end{aligned} \tag{5.8}$$

The normalized heat flux is found for each particular device by either integrating an assumed steady-state source profile, i.e.,

$$\tilde{q} = \frac{1}{\rho}\int_0^\rho \rho'\,\tilde{S}_0(\rho')\mathrm{d}\rho'\ , \tag{5.9}$$

or by using the heat flux reported in the literature associated with the specific experiment.

In RTP, steady-state electron temperature profiles have been measured that exhibit the type of hollow profiles naturally associated with the radial fractional model, as shown in figure 3.6. Thus, the results of RTP are compared to model temperature profiles obtained using equation (5.6) with $m = 0$, and a constant value of χ_α, while the order of the fractional derivative, α is varied. The value of the temperature at the boundary ($\rho = 1$) is always the same, $T(1) = 0.2$ keV.

The radial fractional model is also compared to the amplitude and phase of temperature fluctuations produced by off-axis power modulation in the tokamak devices ASDEX-Upgrade, JET, and DIII-D. These particular devices are selected because the time-averaged equilibrium temperature profile for each power modulation experiment is readily available in the literature. This equilibrium temperature profile is needed to determine the steady-state fractional diffusivity, $\tilde{\chi}_\alpha(\rho)$, for each choice of fractional order α, from (5.8) and the normalized heat flux specific to each device and experimental arrangement. The effective fractional diffusivities are then used in (5.6) to find the complex values of the fluctuating temperature. For comparison to data, the complex functions $T^{(m)}(\rho)$ are decomposed into the harmonic amplitude A_m and phase ϕ_m via the relation

$$T^{(m)}(\rho) = A_m(\rho)\, \exp(i\, \phi_m(\rho)) \ . \tag{5.10}$$

The Dirichlet boundary condition $T^{(m)}(1)$ for each m is set by extrapolating the measured amplitude and phase data to the boundary.

In the power modulation calculations, a spatially varying electron density is also used; figure 5.1 displays the density shape functions $N(\rho)$ used in the calculations. These profiles are extracted from published figures of the measured electron density for the individual experiment assessed or, in the case of ASDEX-Upgrade, from density profiles measured under similar experimental conditions[APG04]. For the steady RTP calculations, it is assumed that $N(\rho) = 1$, and that $\bar{n}_e$ does not vary significantly with deposition radii.

In all the calculations reported here, the mask function boundary layer parameter (refer to (5.2)), $b = 0.025\,a$ and the boundary layer diffusion strength parameter (refer to (5.5)), $\tilde{\zeta} = 1$. Also, the radial fractional model assumes that the tokamak device is a torus with circular cross-section with minor radius a and

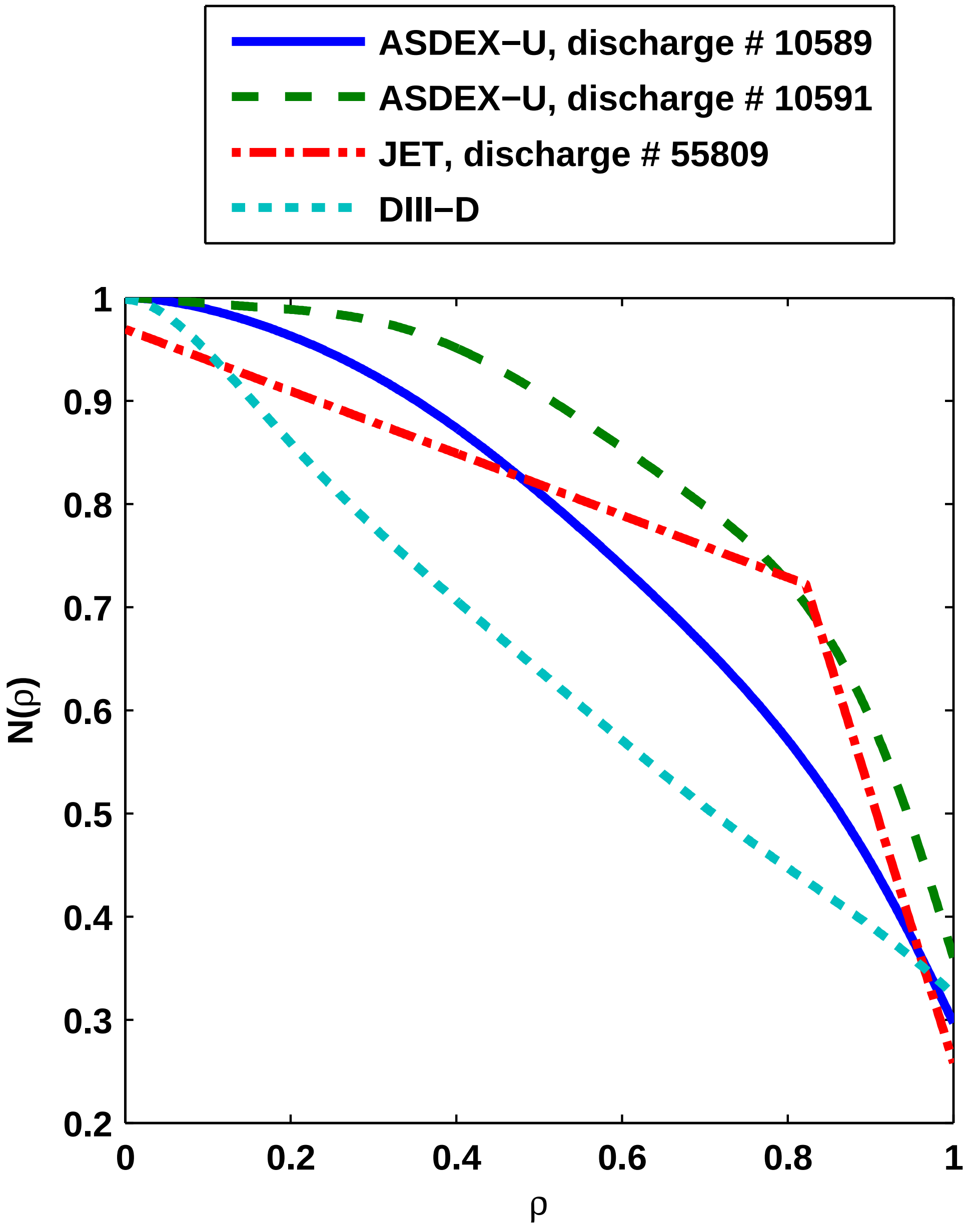

Figure 5.1: Electron density shape functions used in fractional power modulation calculations.

machine	minor radius, a (cm)	major radius, R_0 (cm)
ASDEX-Upgrade	50	165
DIII-D	60	170
JET	125	296
RTP	16.4	72

Table 5.1: Effective major and minor tokamak radii

major radius R_0. Table 5.1 lists the effective minor and major radii used for each device in the calculations.

5.2.1 RTP

Steady off-axis ECH experiments performed in RTP have found hollow electron temperature profiles [BBH99, HCB98], or profiles with temperature peaks away from the origin. These steady temperature profiles are reminiscent of the hollow profiles predicted by the radial fractional model (cf. figures 3.6 and 3.7 in Chapter 3.3) when χ_α is held constant. In these ECH experiments, the ECH source location, or deposition radius ρ_{dep}, is varied and for each ρ_{dep} the resultant steady temperature profile is measured. The core temperature $T(0)$ is found to depend on ρ_{dep} such that $T(0)$ exhibits several plateaus in which $T(0)$ remains constant over a range of ρ_{dep} (see figure 7 in Ref. [BBH99]). The transition between different plateaus occurs over changes in ρ_{dep} sharper than the ECH deposition width. These plateaus and the sharp transition regions between plateaus are taken, among other things, as evidence of electron transport barriers (ETB) by de Baar et al. [BBH99], who explain the experimental results using an ETB model with transport barriers located at the rational safety factor surfaces, and an outward convective heat flux. These transport barriers are modeled in a conventional diffusion model as narrow valleys in the diffusivity which itself is constant outside the ETB. The outward heat flux is needed to produce a hollow temperature profile as emphasized by Hogeweij et al. in Ref. [HCB98].

The hollow RTP profiles have also been modeled by March et al. in Ref. [MCD04] using a simple sandpile model. The results of this model share similar qualitative features with the experimentally measured profiles, such as the hollow shape of the profiles, the presence of ears or sharp peaks at the power source, and consistency in the outboard profile regardless of deposition radius. However, in Ref. [MCD04] direct quantitative comparisons are not made between the model results and experimental profiles, and so these results are not included in figure 5.4.

Although the radial fractional model cannot reproduce the plateaus observed in $T(0)$ when χ_α is strictly constant over the domain, the fractional model does predict hollow profiles for uniform χ_α that are in good agreement with the profiles measured in RTP. These calculations achieve good agreement with the data using a heat source of the form

$$\tilde{S}(\rho) = \frac{1}{4\pi^2\, a^2\, R_0\, \bar{n}_e} \left[\frac{P_{ohm}(\rho_{dep})}{M_{ohm}} \frac{\Theta(\rho; 0, 0.9)}{1 + (\rho/0.5)^2} + \frac{P_{ech}}{M_{ech}} \exp\left[- \left(\frac{\rho - \rho_{dep}}{0.0431} \right)^2 \right] \right], \tag{5.11}$$

and a value of χ_α that is chosen separately for each α to minimize the error between calculation profile and measured data. It should be noted that the Cauchy function chosen for the Ohmic source term is an ansatz; the shape of the Gaussian ECH source term is obtained from figure 7 in Ref. [BBH99]. In the source given by equation (5.11), P_{ohm} and P_{ech} are the total integrated power due to ohmic heating and the off-axis ECH heating respectively. For all calculations, $P_{ech} = 0.35$ MW. The Ohmic heating power P_{ohm} depends on ρ_{dep}, since the Ohmic dissipation near the core is reduced when the ECH heating moves closer to the center and increases the conductivity. As reported by de Baar et al. [BBH99]: “During ECH this [Ohmic dissipation] reduces to 50 kW for centrally heated discharges and 100 kW for off-axis heated discharges at $\rho_{dep} = 0.5$”. In the fractional model

	Plateaus				
	A	B	C	D	E
ρ_{dep}	0.15	0.32	0.38	0.44	0.55
$\bar{n}_e$	$2.7 \times 10^{13} \quad \text{cm}^{-3}$				

Table 5.2: Deposition radii used in RTP comparison

calculations, this dependence is modeled with the following expression for the total Ohmic input power

$$P_{ohm}(\mu) = 0.05 + \begin{cases} 0.1\,\mu & 0 \leq \mu < 0.5 \\ 0.05 & 0.5 \leq \mu \leq 1 \end{cases} \quad (\text{MW}) \ . \tag{5.12}$$

Also note that the constants M_{ohm} and M_{ECH} are integration constants chosen so that the volume integrals of the Ohmic and ECH terms equal the total powers P_{ohm} and P_{ECH} respectively. Also note that $\Theta(\rho; a, b)$ is the top-hat function defined as

$$\Theta(\rho; a, b) = \begin{cases} 1 & \text{if } \rho \in [a,\ b] \\ 0 & \text{otherwise} \end{cases} \ . \tag{5.13}$$

Table 5.2 gives the deposition radii ρ_{dep} and characteristic electron density $\bar{n}_e$ used in the fractional model calculations performed for each plateau profile.

Figure 5.2 shows the results of the fractional model calculations for several values of α for the plateau temperature profile labeled “B” in Ref. [BBH99]. The central valley in the data is well fit by the highly non-local value of $\alpha = 1.25$ and overall the best fit–in the least squares sense–is achieved with $\alpha = 1.5$. When $\alpha = 2.0$, no off-axis peaks can occur with constant χ_α and the calculation temperature profile over-estimates the temperature in the core.

Figure 5.3 reproduces the measured temperature profiles for five of the plateaus along with the fractional calculation profiles for the α that best fits the corresponding plateau profile. The trend in α appears to favor higher αs when the

ECH source is near the core and a lower, more non-local, α when the source location is near the outer edge of the domain. This trend could indicate that the ECH location changes the overall transport in the system and thus α changes globally when ρ_{dep} is moved, or alternatively, that the system is best described by an $\alpha(\rho)$ that changes throughout the domain.

Figure 5.4 shows the temperature profile for a transitional deposition radius located between different plateaus and the calculation profiles for the ETB model proposed by de Baar et al. [BBH99] and the fractional model. The fractional order α is chosen, again, to best fit the data. For the value $\alpha = 1.20$, the fractional calculation fits the measured data better than the ETB model. However it should be noted that the constant χ_α fractional model does not reproduce the plateaus in $T(0)$ vs ρ_{dep} as the ETB model by de Baar et al. [BBH99] does (see figure 7 in Ref. [BBH99]).

5.2.2 ASDEX-Upgrade

Power modulation experiments provide another method of assessing the results of the radial fractional transport model. In this subsection, the fractional model is applied to off-axis ECH modulation experiments performed in ASDEX-Upgrade for various steady-heating schemes. In particular, this subsection focuses on experimental results reported in Ref. [IRG01], which includes the measured amplitude and phase for the $m = 0, 1$ harmonics for several different discharges. That manuscript emphasized a critical gradient transport (CGT) model in which the (conventional) diffusivity χ_d depends non-trivially on the scale lengths of the temperature gradients. The predictions of the CGT model reported in [IRG01] are compared to the radial fractional model.

To explore conditions under which the fractional model might be valid, the radial fractional model is applied to two discharges, each with different heating

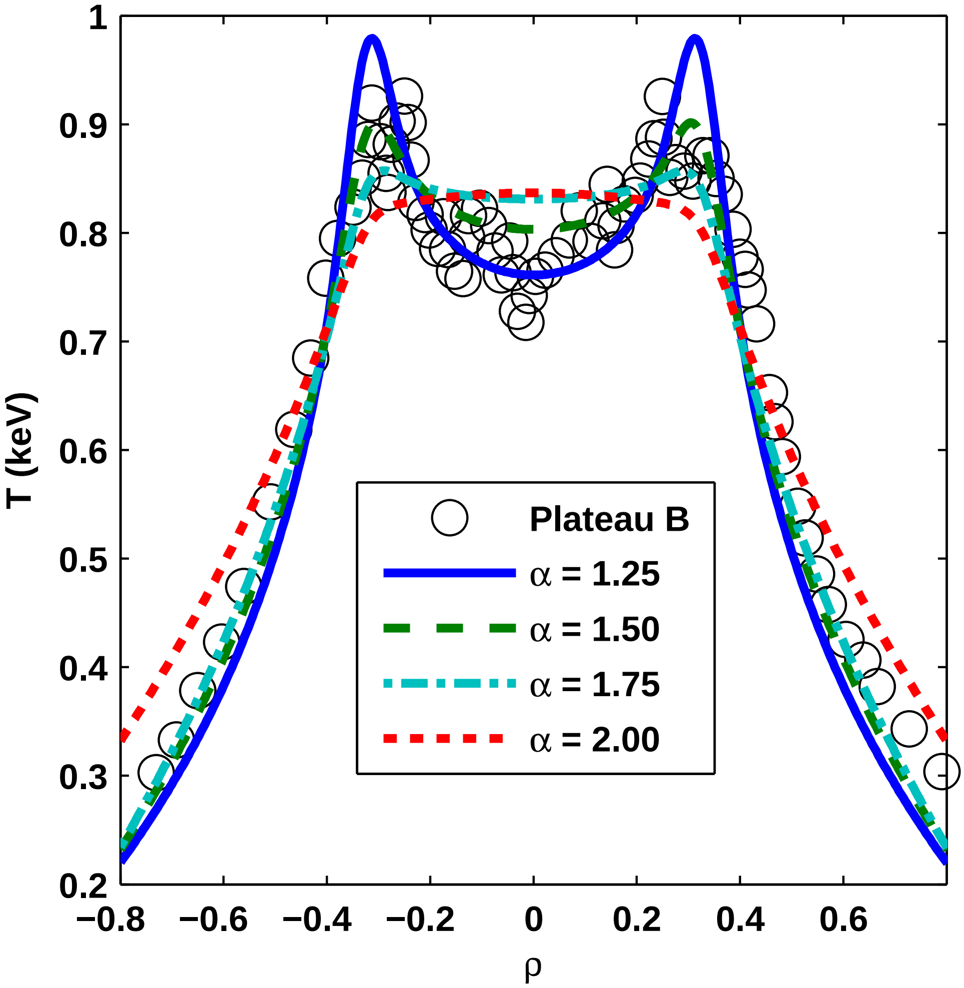

Figure 5.2: Steady-state temperature profile in RTP device for the plateau in core temperature labeled “B” in Ref. [BBH99]. Black circles are experimental temperature measurements. Curves are results from equation (5.6) for different values of the fractional order α.

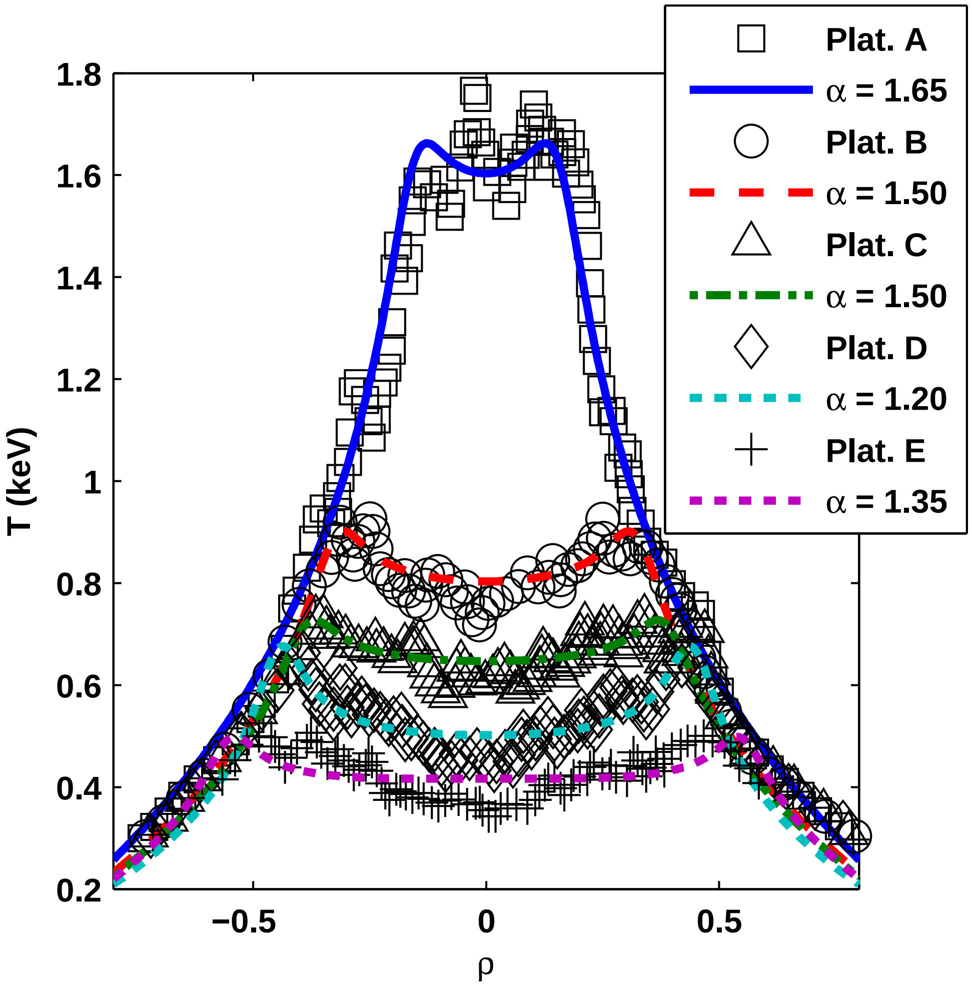

Figure 5.3: Steady-state temperature profiles in RTP device for different off-axis locations of heating source (ECH). Individual dark symbols are experimental temperature measurements. Curves are results from equation (5.6) using a value for the fractional order α that gives best agreement for each location of heating source. It shows that sources closer to the plasma edge cause greater departure from Fick's law.

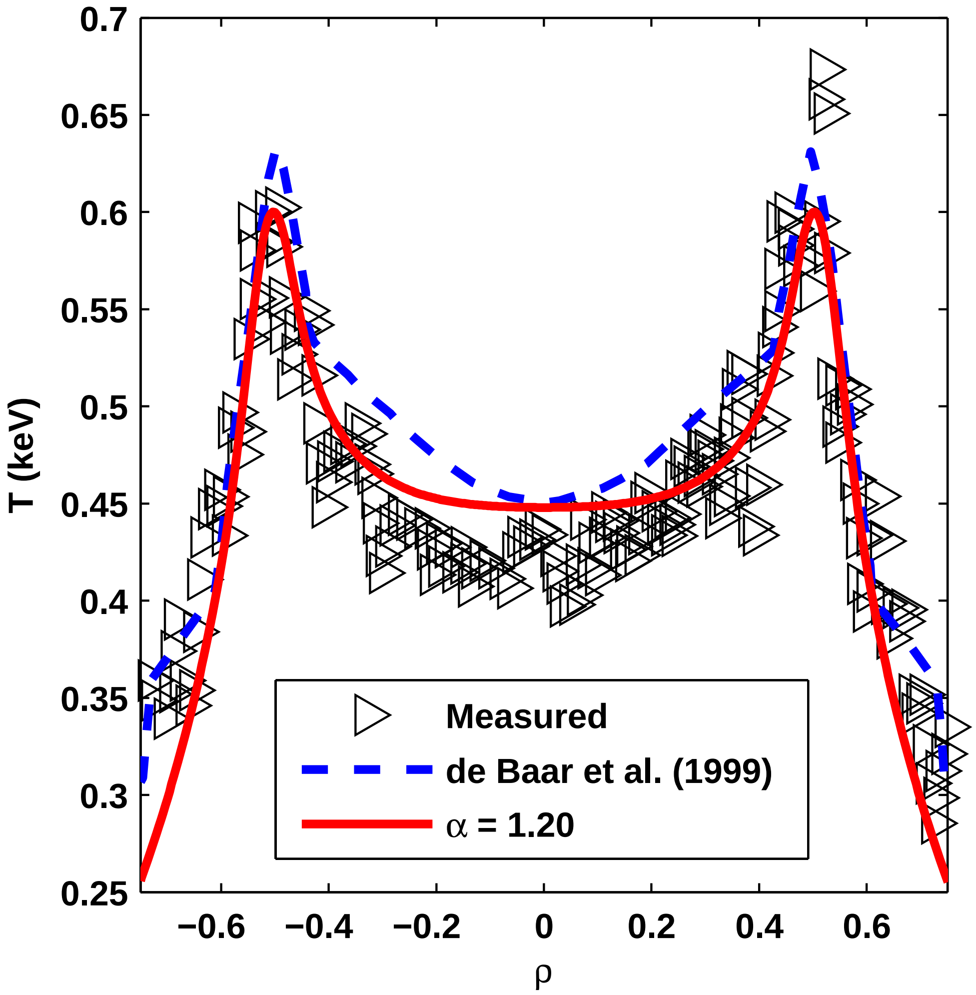

Figure 5.4: Comparison of radial fractional model (continuous red curve) to internal transport barrier model (dashed blue curve) presented in Ref. [BBH99] for off-axis ECH experiment in RTP device. Black triangles are experimental temperature measurements.

and system parameters. Discharge #10589 included steady Ohmic heating, a dominant modulated ECH source, and a higher modulation frequency of 100 Hz, while discharge #10591 included steady ECH heating and steady Ohmic heating, a weaker perturbative modulated ECH source, and a lower modulation frequency of 30 Hz. Table 5.3 summarizes the system parameters used to represent these two discharges in the fractional calculations.

discharge	f_{mod} (Hz)	$\bar{n}_e$ ($\times 10^{13}$ cm^{-3})	P_{ohm} (MW)	P_{ech} (MW)	P_{mod} (MW)	μ_{ech}	σ_{ech}	μ_{mod}	σ_{mod}
# 10589	100	4.4	0.5	0	0.7	n/a	n/a	0.5	0.038
# 10591	30	3.4	0.5	0.58	0.17	0.5	0.0234	0.5	0.025

Table 5.3: Physical parameters used in modeling power modulation experiments in ASDEX-Upgrade device using equations (5.14) and (5.17).

For each discharge, the fractional calculation uses an effective diffusivity $\chi_\alpha(\rho)$ that is obtained from a power balance analysis using equations (5.8) and (5.9), the electron density shape function $N(\rho)$ shown in figure 5.1, the time averaged $m = 0$ temperature profile $T_0 = \langle T(\rho, t)\rangle$, and the following form for the steady sources

$$\begin{aligned}\tilde{S}_0(\rho) = \frac{1}{4\pi^2\, a^2\, R_0\, \bar{n}_e} & \left[\frac{P_{ohm}}{M_{ohm}}\, \Theta(\rho; 0, 0.9) + \frac{P_{ech}}{M_{ech}}\, \exp\left[-\left(\frac{\rho - \mu_{ech}}{\sigma_{ech}} \right)^2 \right] \right] \\ & + \langle \tilde{S}_{mod}(t, \rho) \rangle_{m=0}\ . \end{aligned} \tag{5.14}$$

Note that in equation (5.14), P_{ohm} and P_{ech} are the total input power for the steady Ohmic and ECH heating, respectively, and M_{ohm} and M_{ech} are integration constants defined by

$$\frac{1}{M_{ohm}} \int_0^1 \rho\, \Theta(\rho; 0, 0.9)\, \mathrm{d}\rho = 1\ , \qquad \frac{1}{M_{ech}} \int_0^1 \rho\, \exp\left[-\left(\frac{\rho - \mu_{ech}}{\sigma_{ech}} \right)^2 \right] \mathrm{d}\rho = 1\ . \tag{5.15}$$

The function $\Theta(\rho; a, b)$ is defined in equation (5.13) and $\langle \tilde{S}_{mod}(t, \rho) \rangle_{m=0}$ is the time

		δ	
	α	$\lvert\delta\rvert$	ϕ_δ (rad)
ASDEX-Upgrade, #10589	1.25	0.74	-0.55
	1.50	0.84	-0.44
	1.75	0.97	-0.22
	2.00	1.13	-0.19
ASDEX-Upgrade, #10591	1.25	0.56	-0.37
	1.50	0.70	-0.41
	1.75	0.85	-0.28
	2.00	1.01	-0.21
JET, #55809	1.25	1.24	-0.15
	1.50	1.35	-0.12
	1.75	1.48	-0.11
	2.00	1.60	-0.11

Table 5.4: Source fitting parameter δ for ASDEX-Upgrade and JET power modulation calculations.

averaged $m = 0$ component of the modulated ECH heating, given by

$$\langle \tilde{S}_{mod}(t,\rho)\rangle_{m=0} = \frac{1}{2}\,\frac{1}{4\pi^2\, a^2\, R_0\, \bar{n}_e}\,\frac{P_{mod}}{M_{mod}}\,\exp\left[-\left(\frac{\rho-\mu_{mod}}{\sigma_{mod}}\right)^2\right] \quad . \tag{5.16}$$

Note that the functional form of the steady and modulated ECH sources, i.e., the widths and peak locations of the ECH Gaussians, are extracted from the figures of the ECH sources reported in Ref. [IRG01]. The nearly constant form for the Ohmic source is a simplifying ansatz. Figures 5.5 and 5.6 show the effective fractional diffusivities calculated using the steady source (5.14).

The fractional calculations also use electron density shapes $N(\rho)$ taken from figure 2 in Ref. [APG04]. In Ref. [APG04], electron density profiles for ASDEX-Upgrade in L-mode are given for a purely Ohmic discharge (the downward pointing arrows in figure 2 of Ref. [APG04]) and for a discharge with steady ECH heating (the square symbols in figure 2). The extracted densities are normalized to the peak density values reported in Ref. [IRG01] for the power modulation experiments, and used in the calculations for ASDEX-Upgrade discharges # 10589 and # 10591, respectively.

The calculation of the different m-modes of the thermal waves excited use equation (5.6) with a modulation source with a duty cycle of 50%, giving a mode source $\tilde{S}_m(\rho)$ of the form

$$\tilde{S}_m(\rho) = \delta\,\frac{1-(-1)^m}{2\pi m}\,\frac{1}{4\pi^2\, a^2\, R_0\, \bar{n}_e}\,\frac{P_{mod}}{M_{mod}}\,\exp\left[-\left(\frac{\rho-\mu_{mod}}{\sigma_{mod}}\right)^2\right] \quad , \tag{5.17}$$

where δ is a complex fitting constant whose amplitude and phase is chosen so that the calculation amplitude and phase matches the measured values at the deposition radius μ_{mod}. The values of δ used in Figs. 5.7-5.9 are given in table 5.4. It should be noted that in practice, modulations in electron temperature T can induce modulations in the Ohmic power source, collisional electron-ion energy exchange and radiation which can have damping effects on the T modulations. However, these effects are not included in equation (5.17) and the fractional calculations considered here.

Figure 5.7 compares the results of the fractional calculation for discharge # 10589 to the measured amplitude and phase data of the $m = 1$ mode of the thermal wave. For this discharge, good agreement with the data is observed for $\alpha = 1.75$ on the right side of the modulated source location. On the left, the $\alpha = 1.75$ amplitude and phase profiles have flattened shapes near the origin which is suggestive of the measured amplitude and phase profiles. However, quantitatively, the fractional model yields an amplitude near the center that is several orders of magnitude smaller than the measured amplitude. The flattened amplitude and phase profile of the $\alpha = 1.75$ calculation and the zero in amplitude near $\rho = 0.23$ indicates the presence of a resonant standing wave and is a feature of the fractional model when $\alpha \approx 1.75$; see for example the $\alpha = 1.75$ fractional calculation in figure 5.8. However, it should be noted that saw-teeth are present in the experimental data, with the inversion radius located at $\rho \approx 0.3$, which may have distorted the amplitude and phase data near the origin [IRG01].

Next, figure 5.9 reproduces the data in figure 5.7 but includes now the published predictions of the CGT model proposed by Imbeaux et al. in Ref. [IRG01]. The CGT result is in about as good agreement with the data as the $\alpha = 1.75$ fractional calculation, although the CGT model follows the measured amplitude on the left side more closely.

Figure 5.8 compares the fractional results for discharge # 10591 to the measured amplitude and phase data. In this discharge the modulation frequency is smaller and the modulation source is small compared to the amount of steady heating power. Also the off-axis steady ECH heating has produced a large gradient in the $m = 0$ temperature profile at the modulation power location μ_{mod}. For this discharge none of the fractional calculations are in good agreement with the measured amplitude and phase data. However, for the power balance diffusivities $\chi_\alpha(\rho)$ used, the best agreement is observed for the conventional diffusion case with $\alpha = 2.0$. As $\alpha \to 1$ the calculation amplitude and phase profiles become increasingly narrow, which is a recurring feature of the fractional model results of power modulation experiments.

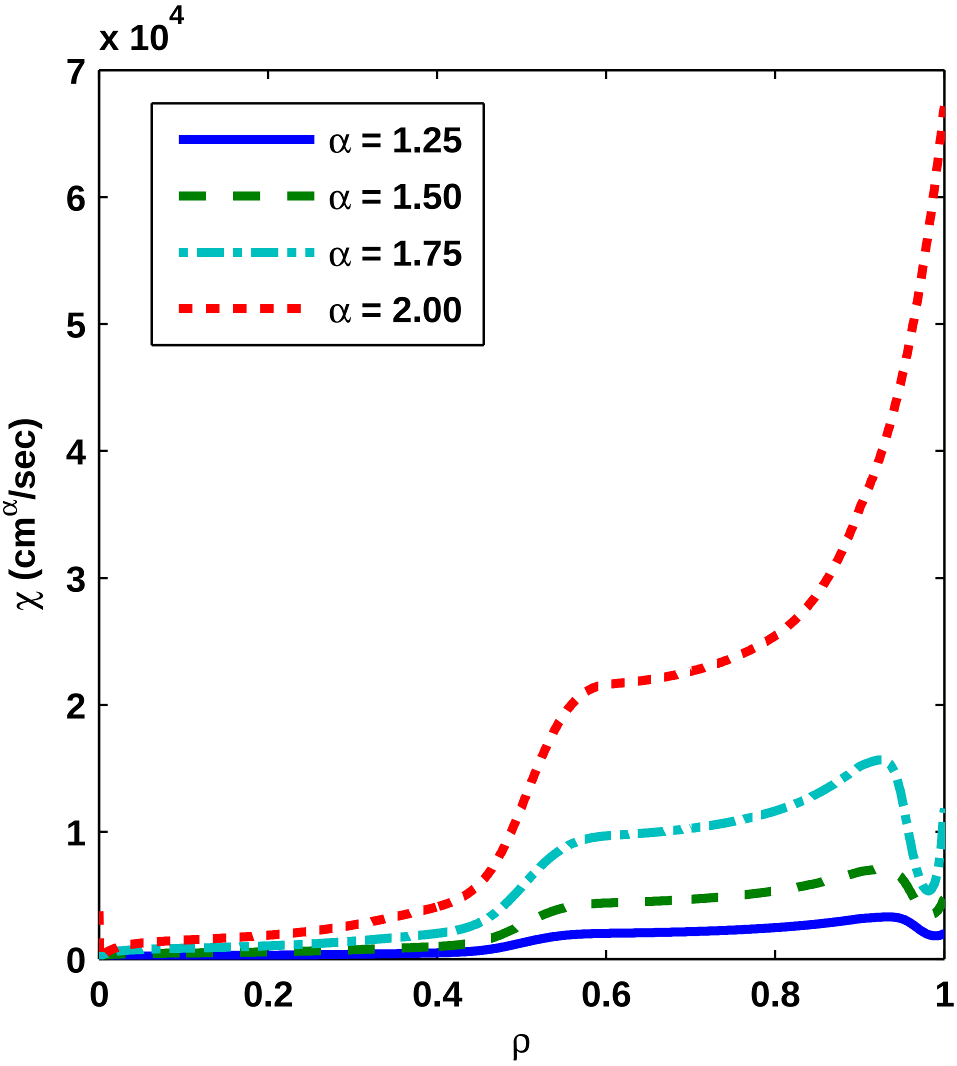

Figure 5.5: Effective fractional diffusivities for ASDEX-Upgrade discharge # 10589 extracted from power balance analysis using equations (5.8) and (5.9), the time averaged temperature, the electron density shape $N(\rho)$ given in figure 5.1, and the steady source in equation (5.14). The time averaged temperature profile is found by integrating the gradient profile reported in figure 5 of Ref. [IRG01] and then stipulating a peak value of 1.5 keV. Note the α-scaling used in the units for the corresponding dimensional values.

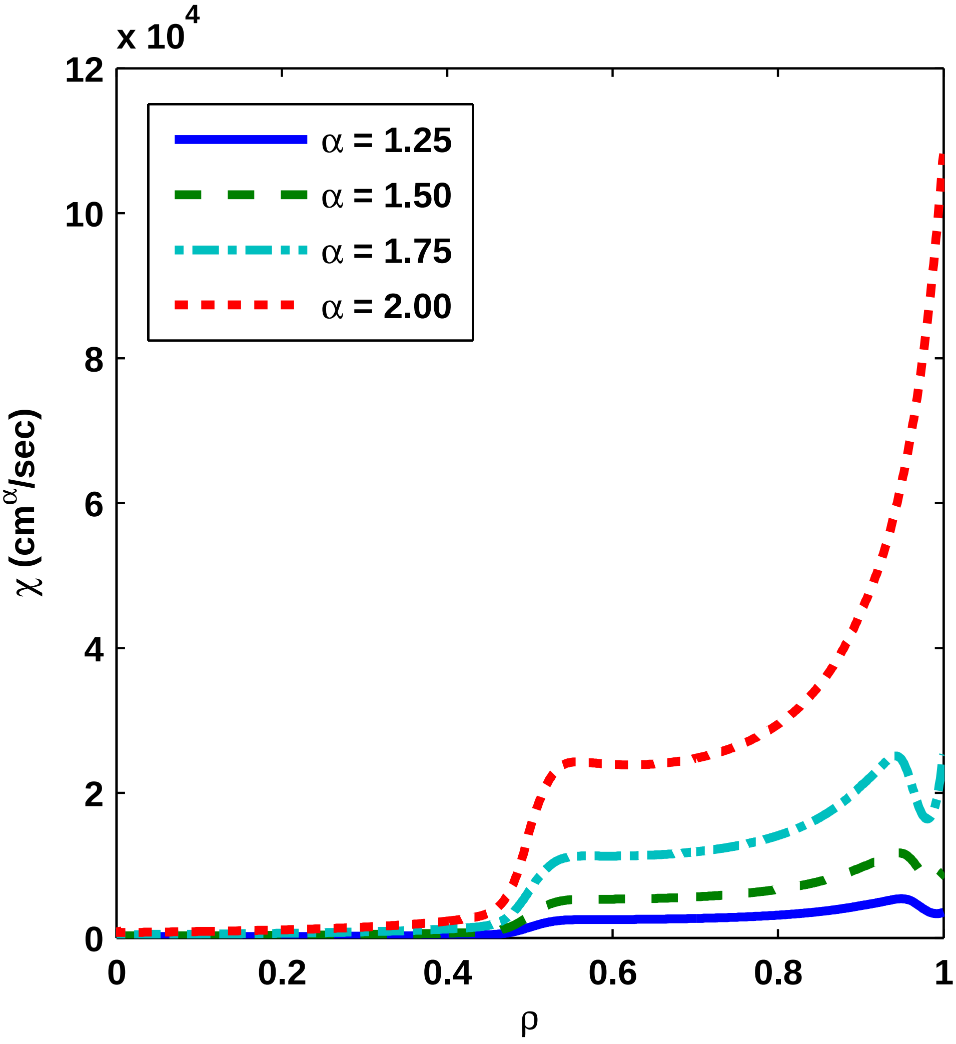

Figure 5.6: Effective fractional diffusivities for ASDEX-Upgrade discharge # 10591 extracted from power balance analysis using equations (5.8) and (5.9), the time averaged temperature reported in figure 11 of Ref. [IRG01], the electron density shape $N(\rho)$ given in figure 5.1, and the steady source in equation (5.14). Note the α-scaling used in the units for the corresponding dimensional values.

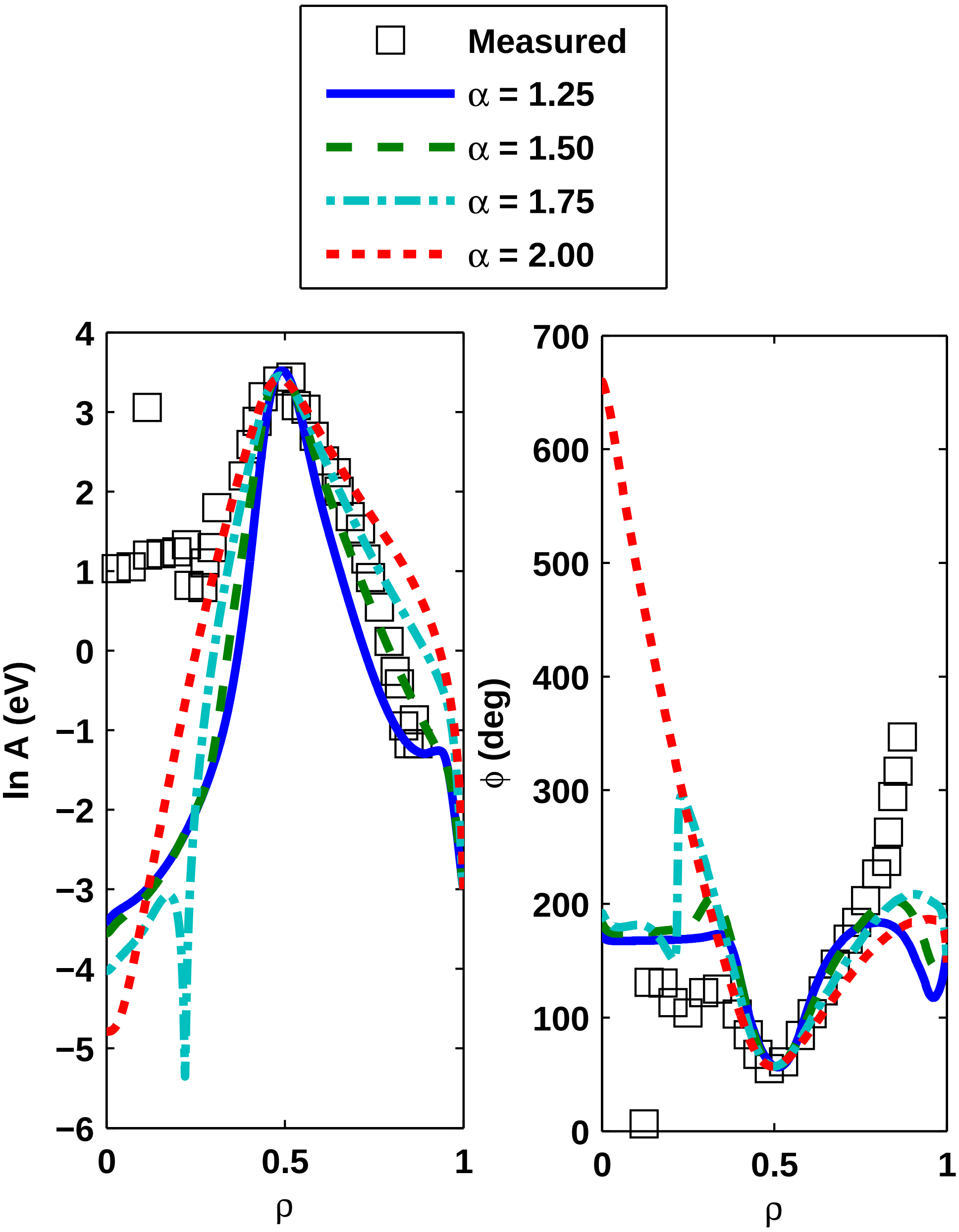

Figure 5.7: Radial profiles of amplitude (left panel) and phase (right panel) of thermal waves excited in ASDEX-Upgrade discharge # 10589. Open squares are measured values extracted from figure 4 of Ref. [IRG01]. Curves are calculated from radial fractional model using the modulation source in equation (5.17) and the χ_α shown in figure 5.5.

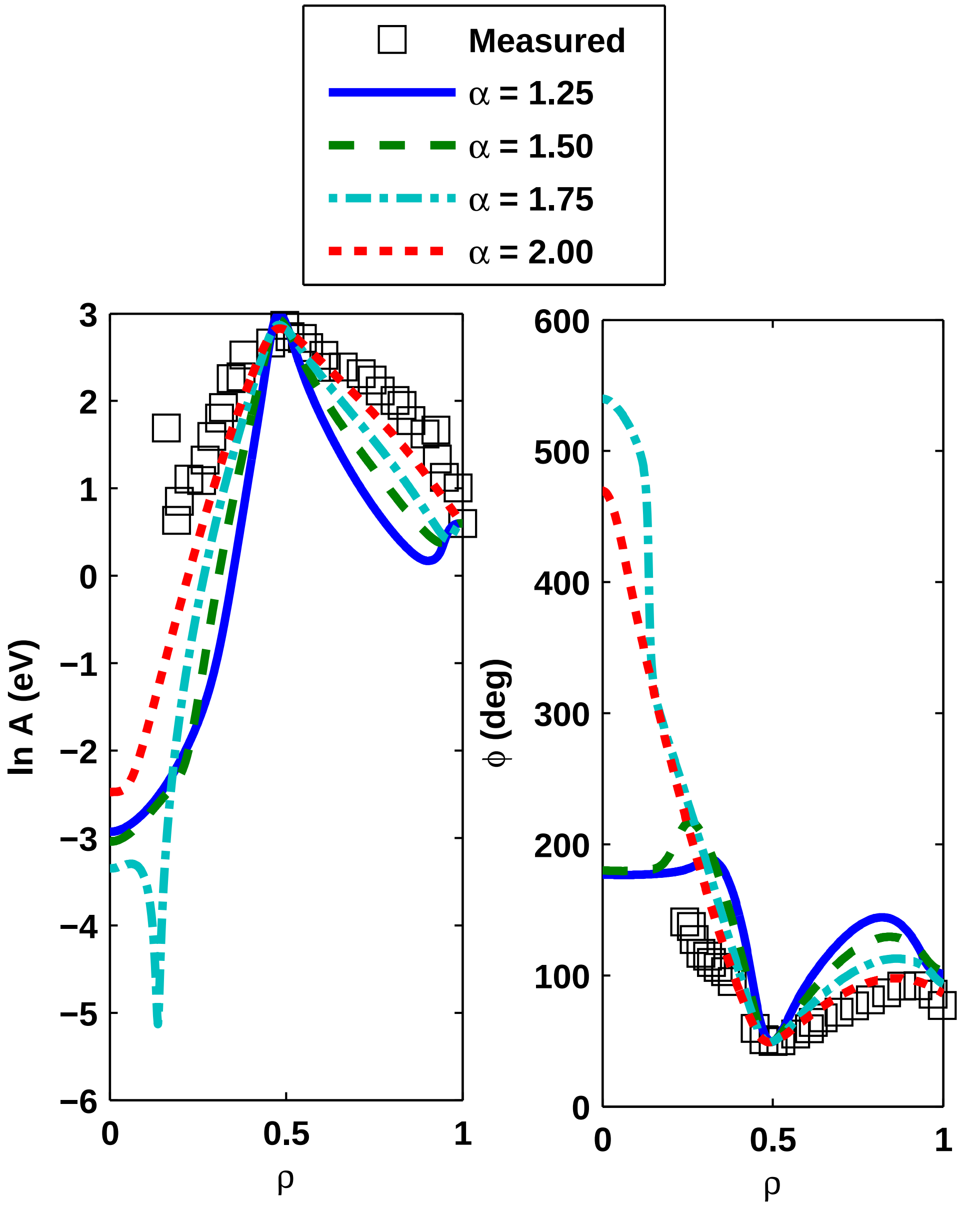

Figure 5.8: Radial profiles of amplitude and phase of thermal waves excited in ASDEX-Upgrade discharge # 10591. Open squares are measured values extracted from figure 9 of Ref. [IRG01]. Curves are calculated from radial fractional model using the modulation source in equation (5.17) and the χ_α shown in figure 5.6.

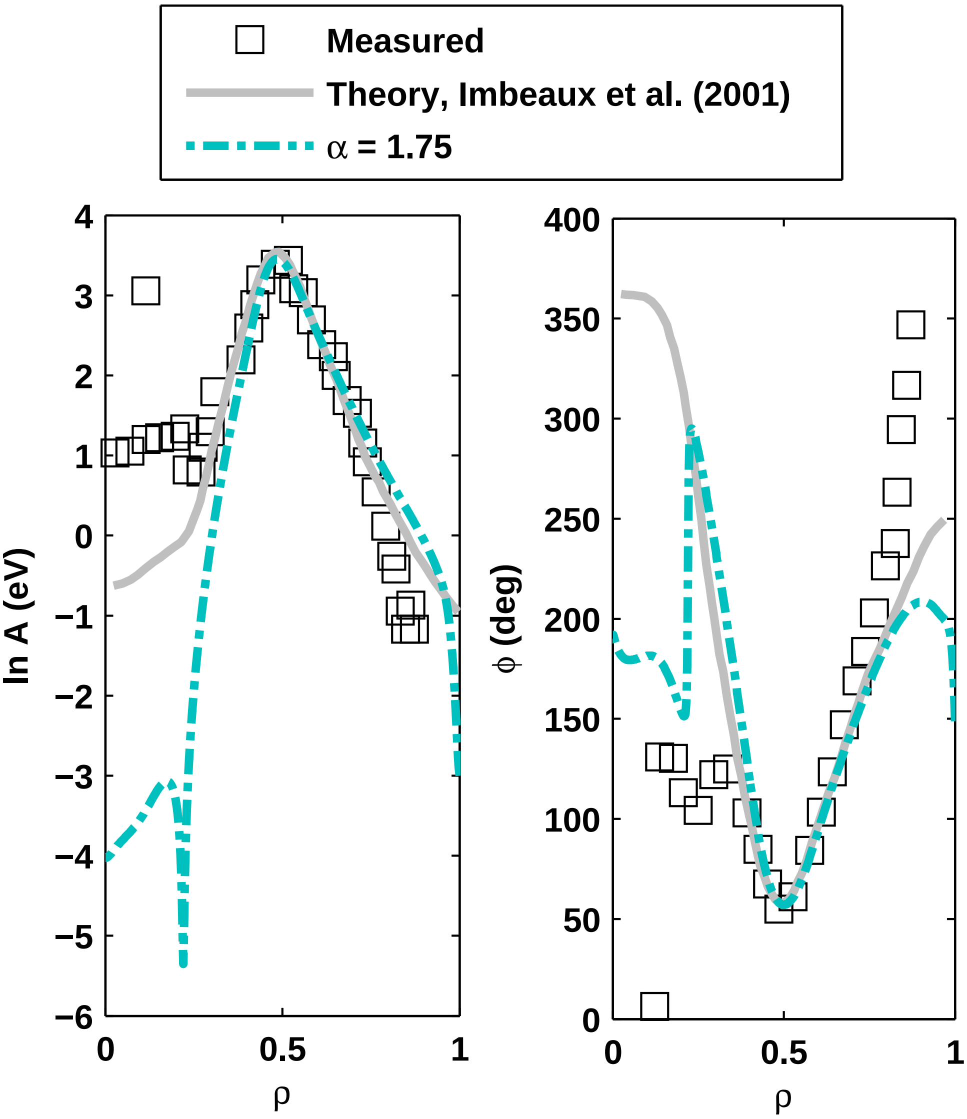

Figure 5.9: Comparison of radial fractional model to critical gradient model (CGT) presented in Ref. [IRG01] for ASDEX-Upgrade discharge # 10589. Same as figure 5.7, but with gray curve showing the predictions of the CGT model and only the $\alpha = 1.75$ result (cyan dashed curve).

5.2.3 JET

In this subsection the radial fractional model is applied to power modulation experiments performed in JET. These experiments use ion cyclotron resonance heating (ICRH) to heat the electrons and achieve the modulation in electron temperature. In what follows, the discussion focuses on experimental results reported by Mantica et al. in Ref. [MCG08]. These experiments have been the subject of several proposed transport models. In [MCG08] the results of a CGT model are reported. Also, in Ref. [CMN08], del-Castillo-Negrete et al. apply a Cartesian 1D fractional transport model to the JET experiments. In figure 5.12 the results of the the 1D Cartesian fractional model, the CGT model reported in [MCG08], and the radial fractional model are compared with experimental results.

The radial fractional calculations use effective diffusivities $\chi_\alpha(\rho)$ that are obtained from equation (5.8) using the measured steady temperature profile, electron heat flux, and electron density reported in figures 6, 7, and 16 respectively, of Ref. [MCG08]. Note that the reported heat flux is produced by Mantica et al. with the transport code ASTRA by finding the power deposition profiles that best fit the measured data. Figure 5.10 shows the effective fractional diffusivities.

The radial fractional calculations also use the experimental modulation duty cycle of 50% for which the even m harmonics of the source are eliminated. For the odd harmonics, the modulated mode source is

$$\tilde{S}_m(\rho) = \delta \, \frac{1-(-1)^m}{2} \, \frac{S_{mod}}{2\pi \, m \, \bar{n}_e} \, \exp\left[-0.5 \left(\frac{\rho - \mu_{mod}}{\sigma_{mod}} \right)^2 \right] , \tag{5.18}$$

where δ is a complex fitting constant whose amplitude and phase are chosen so that the calculation amplitude and phase matches with the measured data at the modulated source location. The values of δ used here are given in table 5.4. The values used for the source amplitude S_{mod}, source location μ_{mod}, and source width σ_{mod} are reported in table 5.5; these values are extracted from the power deposition profile reported in figure 6 of Ref. [MCG08].

f_{mod} (Hz)	15
$\bar{n}_e$ ($\times 10^{13}\,\mathrm{cm}^{-3}$)	3.0
S_{mod} $\left(\frac{\mathrm{W}}{\mathrm{cm}^3}\right)$	0.17
μ_{mod}	0.34
σ_{mod}	0.085

Table 5.5: Physical parameters used in modeling power modulation experiments in JET device using equation (5.18).

Figure 5.11 shows the amplitude and phase of the first two harmonics ($m = 1, 3$) of the fractional calculations. As was observed in the ASDEX-Upgrade discharge #10591, the amplitude and phase of the fractional model become increasingly narrow as $\alpha \to 1$. In this case the best agreement between the model results and the experimental data occurs for $\alpha = 2.0$; however, none of the calculation amplitudes or phases agree well with the measured experimental values.

For the same discharge, figure 5.12 compares the amplitude and phase calculations from different models–namely, the Cartesian fractional model of Ref. [CMN08], the critical gradient theory (CGT) model of Ref. [MCG08], and the radial fractional model discussed here. To understand the comparison between the models, it should be noted that the Cartesian fractional model consisted of a mixture of fractional diffusion and conventional Fick's law diffusion. In particular, the diffusivities used in that model are as follows

$$\begin{aligned} \chi_\alpha(x) &= \tanh\left(\frac{x-0.1}{0.025}\right) + \tanh\left(\frac{0.1}{0.025}\right) \quad \left(\mathrm{m}^\alpha \mathrm{s}^{-1}\right) \ , \\ \chi_2(x) &= 0.75 + 6x \quad \left(\mathrm{m}^2\mathrm{s}^{-1}\right) \ . \end{aligned} \tag{5.19}$$

In the radial fractional model, no conventional diffusion is included in the interior of the domain (away from the boundary layer at the edge), in part because it is not possible to determine the diffusivities for both fractional and conventional diffusion from the steady state profile alone. Both the CGT model and the Cartesian fractional model fit the experimental data better than the radial fractional model.

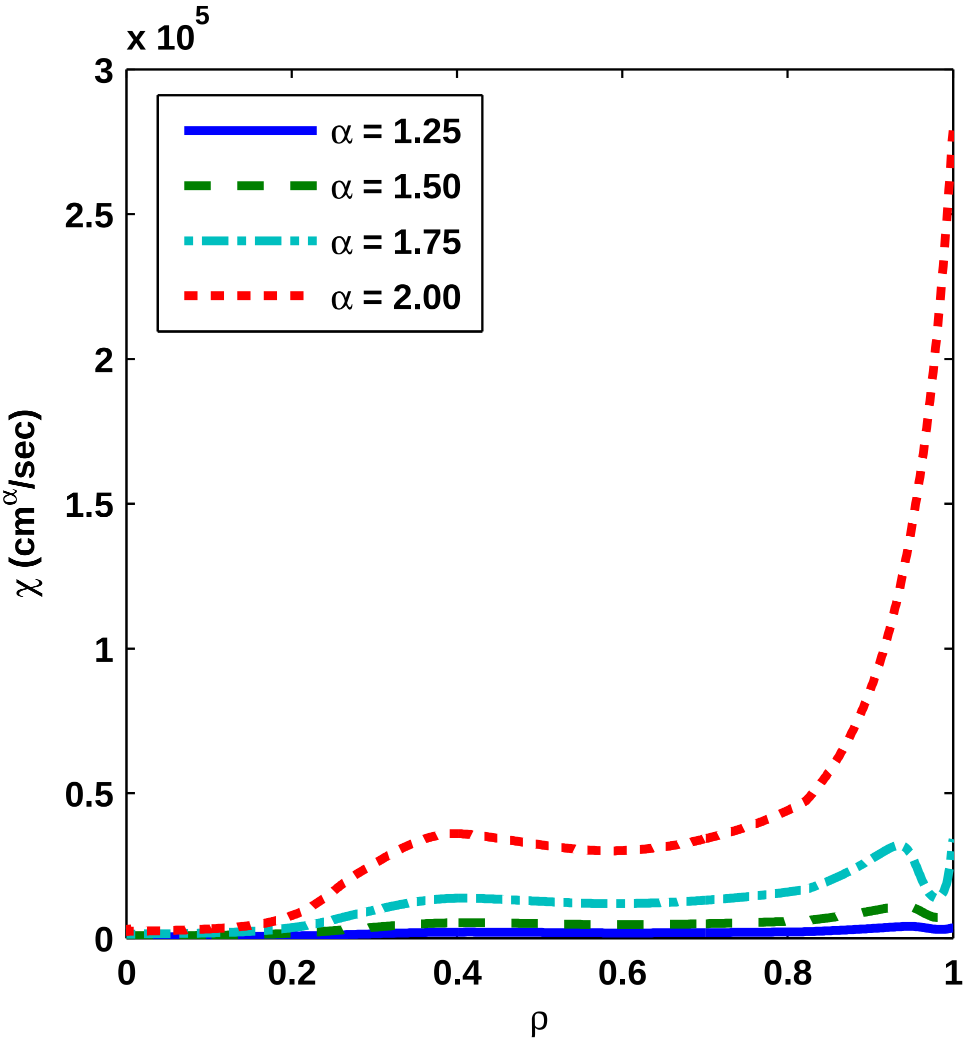

Figure 5.10: Effective fractional diffusivities for JET discharge # 55809 extracted from power balance analysis using equation (5.8) and the measured steady-state temperature, electron density (cf. figure 5.1), and fitted electron heat flux reported in Ref. [MCG08]. Note the α-scaling used in the units for the corresponding dimensional values.

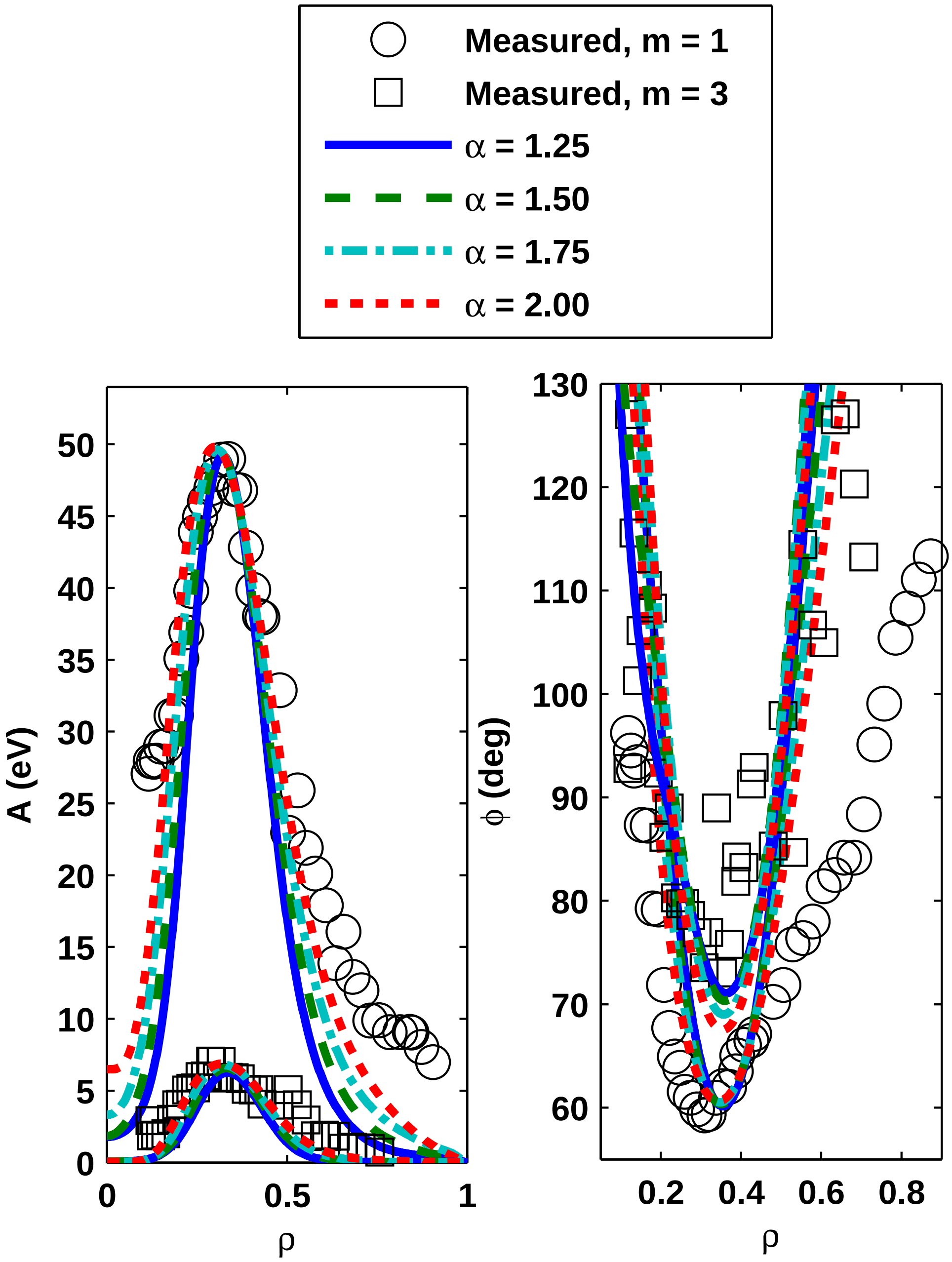

Figure 5.11: Radial profiles of amplitude (left panel) and phase (right panel) of thermal waves excited in JET discharge # 55809. Black circles and boxes correspond to the measured $m = 1$ and $m = 3$ modes, respectively, as reported in Ref. [MCG08]. Curves are calculated from radial fractional model using the modulation source in equation (5.18) and the χ_α shown in figure 5.10.

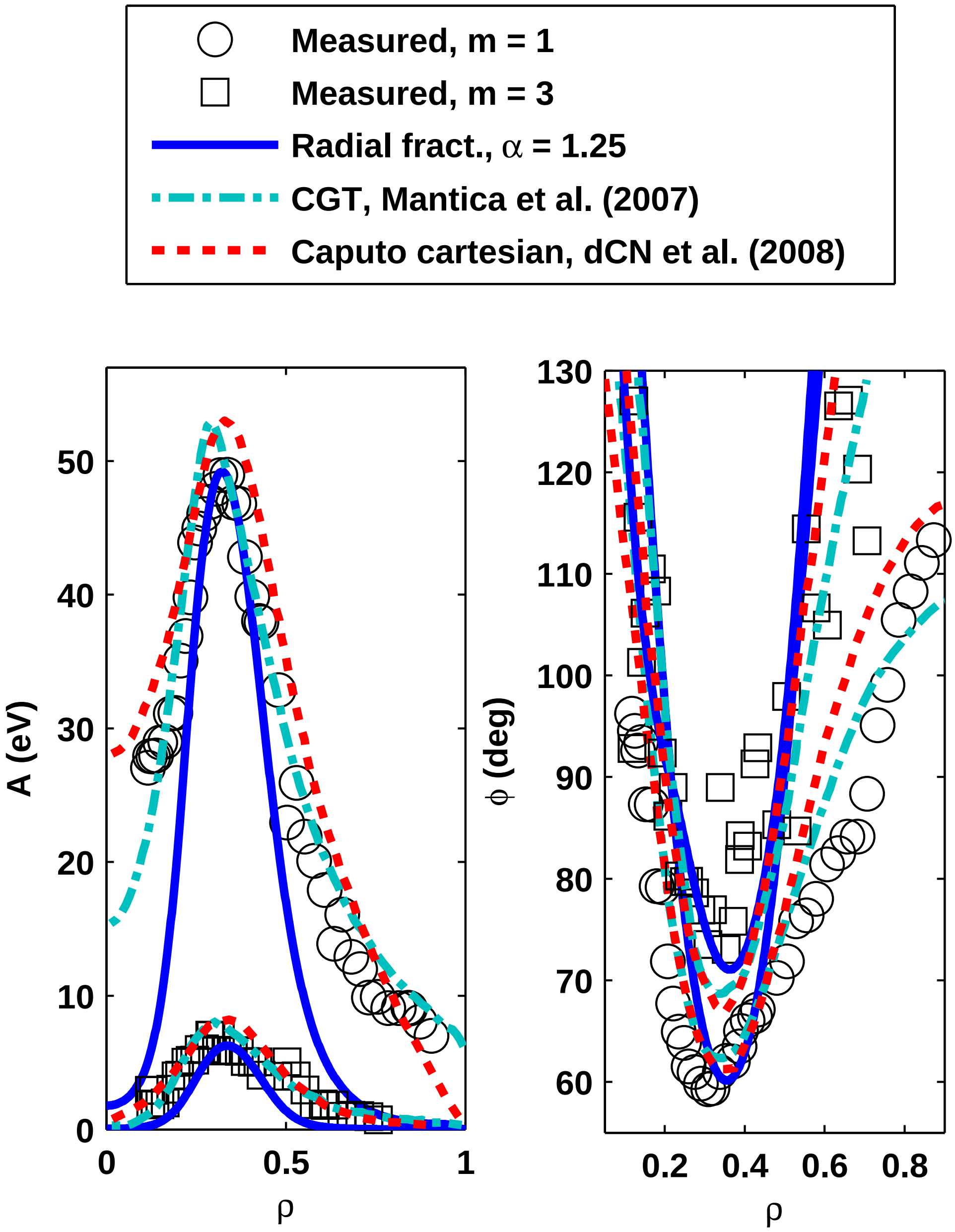

Figure 5.12: Comparison of radial fractional model (blue solid line) to Cartesian fractional model (red dashed curve) of Ref. [CMN08], and to the critical gradient model (CGT, dot-dashed cyan curve) of Ref. [MCG08] for the same JET experiment of figure 5.11.

5.2.4 DIII-D

Results of an ECH power modulation experiment in DIII-D have been reported in Refs. [DPW12, HDP13]. In this subsection the radial fractional model is applied to the data presented in the figures shown in Ref. [DPW12].

In this case the fractional model is implemented using a postulated Gaussian radial shape for the ECH power source with parameters adjusted to minimize the deviations between the numerical results and the measurements. This is done to assess the dependence of the fractional model on the power deposition profile. Thus, the modulated source takes the form

$$\tilde{S}_m(\rho) = \frac{S_{mod}(\alpha)}{m\,\pi\,\bar{n}_e} \exp\left[-\left(\frac{\rho - \mu_{mod}(\alpha)}{\sigma_{mod}(\alpha)}\right)^2\right] . \tag{5.20}$$

For each α-numerical result presented, the values of $S_{mod}(\alpha)$, $\mu_{mod}(\alpha)$, and $\sigma_{mod}(\alpha)$ are chosen to give the best agreement. Table 5.6 gives the optimal parameters used. The effective fractional diffusivities are obtained from equation (5.8), and the measured steady-state profiles, electron density profiles, and heat fluxes reported in Ref. [DPW12] for the $(1, 4.5)$ ECH heating scheme. Figure 5.13 shows the resultant effective fractional diffusivities.

α	S_{mod} $\left(\frac{\mathrm{W}}{\mathrm{cm}^3}\right)$	μ_{mod}	σ_{mod}	$\bar{n}_e$ ($\times 10^{13}$ cm^{-3})	f_{mod} (Hz)
1.75	0.055	0.618	0.148	3.0	28
2.00	0.086	0.625	0.102		

Table 5.6: Source and physical parameters used in modeling DIII-D power modulation experiments.

Figure 5.14 displays the amplitude (left panel) and phase (right panel) of the thermal waves excited in DIII-D. The dark squares are the data of Ref. [DPW12] for mode $m = 1$, the results of the radial fractional calculation for a non-local $\alpha = 1.75$ are given by the blue curve, and the classical prediction, i.e., $\alpha = 2.0$

corresponds to the red curve. Note that the spatial shape of the power source (shown on the lower part of the right panel) is different for the fractional and the conventional cases. It is seen that both diffusion models can fit the observations rather well, i.e., the phenomena being sampled is more sensitive to the source shape than the details of the transport mechanism. However, the wider source required for the fractional model is not realistic.

5.3 Conclusions

This comparative study surveys applications of a new, and more realistic, fractional diffusion model to off-axis heating experiments performed in the RTP, ASDEX-Upgrade, JET, and DIII-D tokamak devices. Although it may well be possible to more accurately fit individual experimental results by using a judicious mixture of fractional transport and Fick's law transport at different radial positions, this procedure has not been pursued in the present study. Rather, this study directly compares the effects of purely fractional diffusion models to Fick's law diffusion, and thus provides an initial assessment of the presence of fractional transport phenomena in magnetic confinement experiments.

For the steady-state heating experiments in RTP, the radial fractional model, with spatially uniform diffusivity χ_α, predicts hollow electron temperature profiles that are in good agreement with the measured temperature profiles. The results of the fractional model provide a fit as good as, or slightly better, to the data, than the electron transport barrier (ETB) model investigated by de Baar et al. [BBH99]. Moreover, it is found that the best fits to the experimental profiles are obtained when the order of the fractional diffusion parameter α decreases as the location of the off-axis power deposition moves outward. This behavior suggests that in this experiment the fractional transport may not be described by a single global α, but instead may require an $\alpha(\rho)$ that depends on spatial

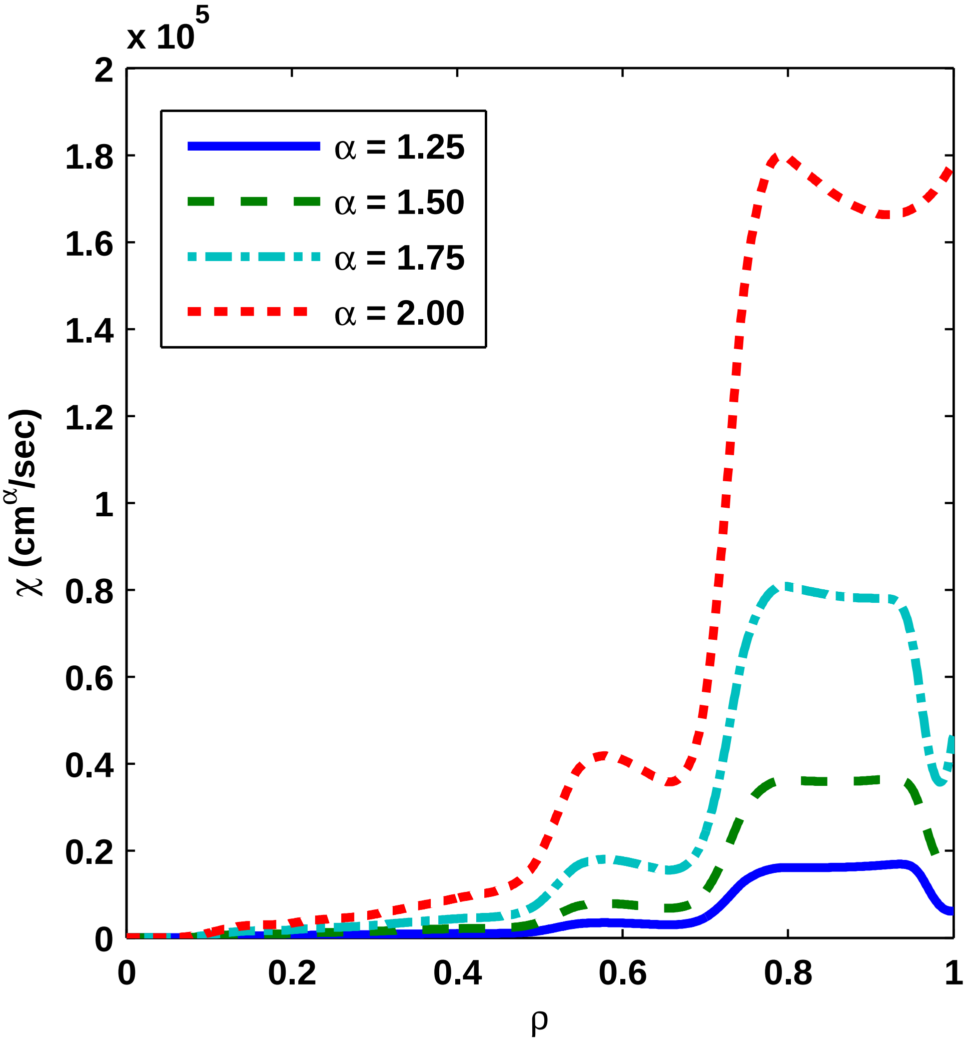

Figure 5.13: Effective fractional diffusivities for the DIII-D power modulation experiment. Values are extracted from the steady-state temperature, electron density profiles (cf. figure 5.1), and electron heat flux profiles given in Ref. [DPW12] for the (1, 4.5) ECH heating scheme. Note the α-scaling used in the units for the corresponding dimensional values.

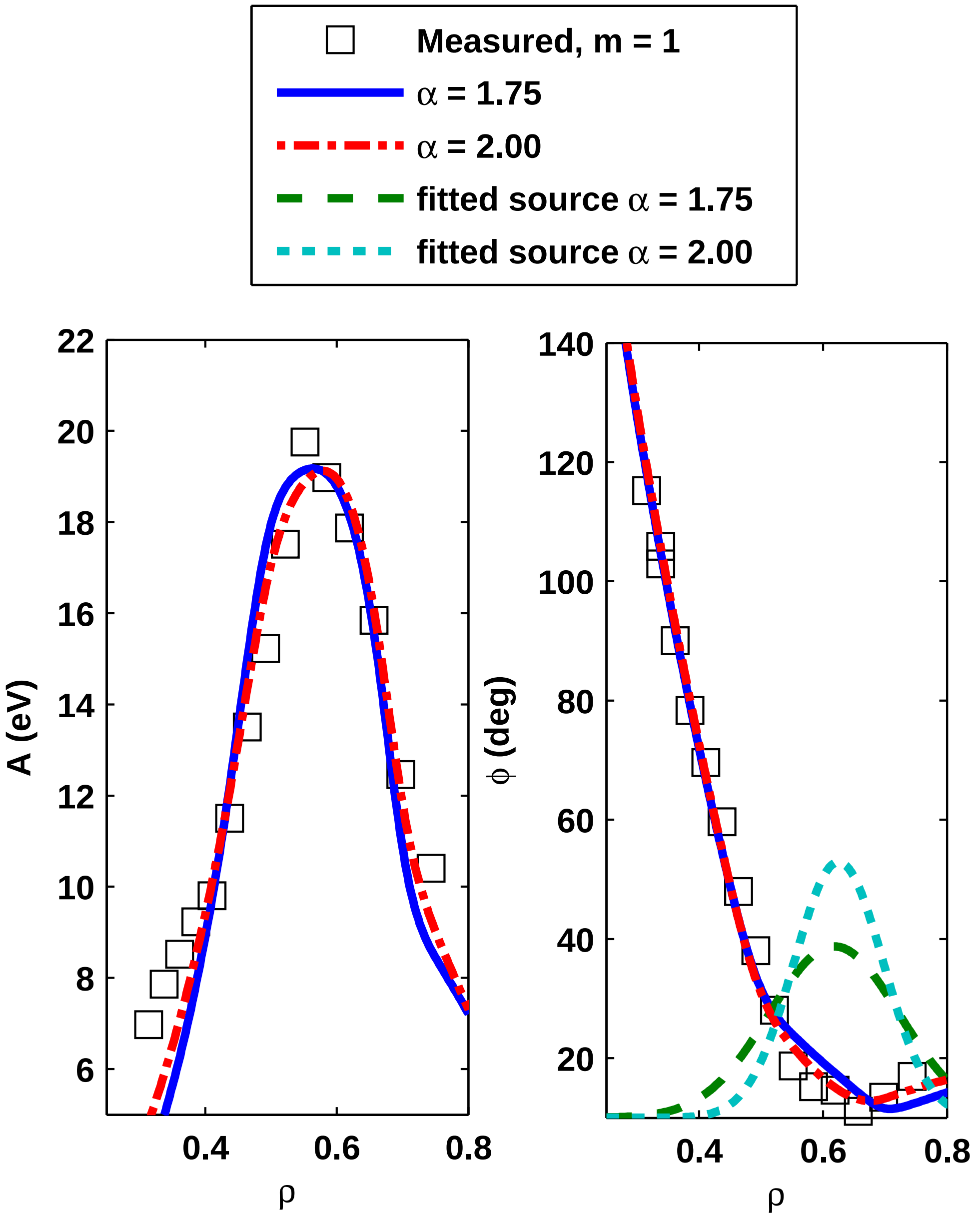

Figure 5.14: Radial profiles of amplitude (left panel) and phase (right panel) of thermal waves excited in DIII-D power modulation experiment. Black squares are measurements reported in Ref. [DPW12]. Blue curve is the result of the radial fractional model for $\alpha = 1.75$ and the red curve corresponds to Fick's law. Different sources (shown in right panel) are used for each model to obtain best fits to the data.

position. In particular the value of α is found to decrease as the source approaches the plasma edge. Physically this implies that the turbulent edge environment has a larger departure from Fick's law than the plasma interior. This perspective is also supported by the comparison to the heat wave propagation in discharge #10589 in ASDEX-Upgrade. In the region between the modulation source and the plasma edge, the best fit to the data is obtained for $\alpha = 1.75$, while the interior side of the plasma column $\alpha = 2.0$ does better.

In the power modulation experiments, the fractional model only achieves good agreement with the measurements for the high-frequency modulation in the purely Ohmic discharge #10589 in ASDEX-Upgrade. For the low-frequency modulation represented by discharges #10591 in ASDEX-Upgrade and #55809 in JET, the fractional model predicts amplitude and phase profiles that are narrower than is observed. For both discharges, the CGT model fits the data better than the radial fractional model.

In modeling the recent DIII-D power modulation experiments, it is possible to reproduce quite well the amplitude and phase of the heat wave by choosing an appropriate profile for the modulation source. However, equally good fits can be obtained both with the fractional model, for $\alpha = 1.75$, and with conventional diffusion. Since the larger source width required for the fractional fit is not realistic, it is suggestive that the transport in this experiment may correspond to Fick's law.

CHAPTER 6

Conclusions

Several useful perspectives can be gained from the research presented in this thesis. One such perspective relates to the subtle manner in which the λ-tempered fractional model acts as an intermediate model between the local conventional diffusion model and the highly non-local fractional diffusion model. More specifically, the λ-tempered fractional model retains many of the anomalous features associated with fractional transport for finite λ and only obtains the local classical result in the $\lambda \to \infty$ limit; this is in contrast to the expectation that classical results might be obtained in the long-time limit. Moreover the tempered model, in the presence of an asymmetry in the underlying stochastic Lévy process, can also exhibit novel behavior that is not present in either the local conventional diffusion model or the highly non-local fractional diffusion model. The mechanism for this behavior is related to the strongly asymmetric tails that appear in the distributions and which are attenuated by increasing the tempering λ. These observations are supported by the parameter study presented in Chapter 2 that focuses on λ-tempered fractional diffusion in external harmonic potentials and periodic potentials with broken spatial symmetry. In the case of harmonic potentials, it is found that while the steady state PDF solutions do approach the Boltzmann distribution in the limit $\lambda \to \infty$, for finite λ the long-time steady-state solutions differ non-trivially from the classical Boltzmann distributions that are predicted by the conventional ($\alpha = 2.0$) Fokker-Planck model. In the case of (asymmetric) periodic potentials, the survey finds that for many system parameters, the presence of tempering acts mainly to reduce the magnitude of the current relative to the untempered case, without significantly altering the qualitative dependencies of the current on the system parameters (cf. figures 2.7, 2.12, 2.13, and 2.16). However, an important exception occurs when there is an asymmetry in the truncated fractional diffusion operator, i.e., for $\theta \neq 0$ (see figure 2.15). In this case, the inclusion of tempering can change the direction of the current when the asymmetry θ in the Lévy noise is strong enough (in the $\lambda = 0$ case) to drive the current in the direction opposite to that favored by the ratchet asymmetry.

As λ-tempered fractional models represent a more physically plausible description of non-local transport, future work with 1D fractional thermal waves and with 2D fractional diffusion will almost necessarily require the eventual inclusion of tempering effects. In that case, the observations given above can guide expectations; in particular, one can expect that a finite λ level of tempering will not, in the long-time limit, remove anomalous features present in the untempered case. For example, with respect to 1D fractional thermal waves, it is reasonable to speculate that the H functions present in the total thermal wave solution will still be retained in some form for finite λ, and will only be removed in the limit $\lambda \to \infty$. With respect to the hollow temperature profiles associated with the 2D radial fractional model with off-axis heating, it is reasonable to speculate that the inclusion of a finite level of tempering will mainly reduce depth of the indentation in center, and that in the limit $\lambda \to \infty$ the upward concavity of the hollow profiles will be flattened.

A large number of fractional transport models are based on 1D Cartesian fractional derivatives that cannot accurately describe the radial transport near the origin of a 2D cylindrical system and which require an ad-hoc condition on the fractional diffusivity to enforce zero flux at the origin. The work presented in Chapter 3 derives a fully 2D isotropic fractional Laplacian from a generalized random walk model that assumes the presence of Lévy flights. In cylindrical geometry this 2D operator can be expanded into a poloidal Fourier series that allows for the description of both radial fractional transport and poloidal fractional transport. The $n = 0$ fractional operator forms a model of radial fractional transport that is appropriate for azimuthally averaged systems. This model correctly describes radial transport near the origin and naturally enforces a zero flux condition at the origin when $\partial_r T(0) = 0$. The higher $n > 0$ terms can be included to describe fractional transport in the poloidal direction. Although the (average) radial component of transport is of primary interest in fusion plasma applications, there may be cases where including the poloidal component of fractional transport is appropriate. For example, the study of a model that includes a zonal shear flow, i.e., a convective flow in the θ-direction, and heat sources or initial conditions with θ dependence requires the higher $n > 0$ terms. Such a model would assess the interaction of the shear flow with the fractional diffusion and the effect of the shear flow layer as a transport barrier with respect to the radial propagation of cold pulses and thermal waves.

The method of deriving the 2D fractional Laplacian can also be generalized to derive a 3D fractional operator. Although no detailed study of this 3D operator has yet been performed, appendix C gives the expression for an isotropic 3D fractional Laplacian that is derived from the CTRW model that includes the presence of Lévy flights. The 3D fractional Laplacian can be expanded into spherical harmonics; the $l = 0$, $m = 0$ operator describes the radial transport in a spherically averaged system. This 3D radial fractional model could have applications in describing non-local transport in stellar interiors and compressed targets in laser fusion.

Additionally the research presented in Chapter 3 illuminates the the differences, near the origin, between the radial fractional model and the Cartesian fractional model. Figure 3.2, for example, compares the functional shape of the radial Green's function at different times to the self-similar shape of the Cartesian

Green's function. From this figure, it is learned that the slab approximation is valid–i.e., the Cartesian and radial Green's functions match–for small times only; once the pulse reaches the core there are significant discrepancies between the two functions. Figures 3.5 and 3.6 display the steady state temperature for the cases: no heating, and constant heating with strong off-axis heating, respectively. In both figures, the temperature profiles exhibit upward concavity near the core suggesting that the radial model strongly favors transporting material away from the core of the system. This is in contrast to the predictions of the Cartesian fractional model with zero fractional diffusivity $\chi_\alpha(x)$ at the origin; figure 3.7–which compares the steady state temperature profiles found from the radial and Cartesian fractional models for an off-axis heating situation–shows that the Cartesian profile is peaked or enhanced at the origin, unlike the hollow profiles of the radial model.

Another impression that is suggested by the research presented here is the need for a more physical model of bounded-domain fractional transport. The bounded-domain model of radial fractional transport presented in section 3.2.4 is based on an unbounded fractional operator that is modified extempore until a plausible operator is obtained. In detail, the steps taken are: the Riemann-Liouville type of operator is used to avoid a spurious flux term in the Caputo formulation, the range of integration of the unbounded domain operator is limited to a finite domain, the kernel is modified with a mask function H_α that removes the mathematical singularities associated with the boundary, and a judicious amount of conventional diffusion is included inside the boundary layer where H_α drops to zero. Although this technique is motivated in part by physical considerations–namely the analogous development of sheath or boundary layers that can occur in plasmas–and the results of the model can be made relatively insensitive to the boundary layer parameters, more sophisticated applications of fractional transport concepts to bounded systems will require a bounded domain model in which all the model boundary parameters are predicted from the physical characteristics of the system. For example, such a sophisticated bounded domain model is almost certainly needed for the development of a fractional resonator model that can be used to design an experimental procedure for finding the α and χ_α of a physical system (cf. the discussion in section 4.4).

This manuscript also advances current understanding of fractional transport as it relates to the nature of fractional thermal waves in the unbounded domain and in the bounded domain or resonator cavity. In Chapter 4, the exact analytic expression for the fractional thermal wave in an unbounded domain is derived for one dimension. To the author's knowledge there is no such analytic expression given in the literature for fractional thermal waves. These solutions were sought in the hope of finding a distinctive feature of fractional transport that could conclusively identify the presence of non-local fractional transport. In the expression for the fractional thermal waves given in equation (4.20), such a distinctive feature can be found in the anomalous H functions. These functions are algebraically decaying and, for symmetric fractional diffusion ($\theta = 0$), inwardly traveling such that they interfere with the outwardly traveling evanescent waves present in equation (4.20). A signature, then, of fractional transport is the appearance of interference peaks near the oscillating source in a homogeneous system.

With regards to the fractional thermal resonator, it has been found that the behavior of fractional thermal waves in a bounded resonator-like domain depends strongly on the bounded domain model of fractional transport. For example, a bounded domain model of fractional transport can be formed with the Caputo fractional derivatives and, in this model, the magnitude of the temperature modulation at the end of the cavity can be larger than at the source location. This unphysical super-resonance effect is due to a contribution in the fractional flux that regularizes the Caputo derivative at the boundary. In the masked Riemann-Liouville model of bounded fractional transport, resonances can be found in the quadrature component of the temperature signal; however, these resonant peaks cannot be related to any resonance condition formed from the unbounded domain dispersion relation and a standing wave resonance condition.

Another outlook gained by the research presented here is that some physical model of fractional transport is still needed to make a truer comparison between fractional transport models and experimental results. In the applications of the fractional model to power modulation experiments discussed in Chapter 5, the conventional diffusivity is set to zero and the fractional diffusivity χ_α is fitted to the experimental time averaged equilibrium temperature profiles. Although this procedure still allows for a partial assessment of the presence of fractional phenomena through the comparison of the model thermal wave results with the time dependent experimental data, a physical model of fractional transport would allow the a priori prediction of the fractional order α and the fractional diffusivity χ_α from the physical characteristics of the system. These derived parameters could then be used in producing steady state temperature profiles and oscillating thermal wave profiles from the fractional model that could be compared with experiment. Moreover a physical fractional model would allow one to predict the correct mixture of fractional diffusion and conventional diffusion at each point in the domain.

A possible avenue of developing a physical model of fractional transport might be found in homogenization theories that average convective features to obtain approximate effective diffusive and non-diffusive transport models. See for example Chapter 13 in Ref. [PS08] in which periodic convective rolls in a convection diffusion model are averaged to produce an effective Fick's law diffusion model with a diffusivity that is enhanced beyond the initial level of "molecular diffusivity" present in the original convection-diffusion equation. In Ref. [Tar89] convective features are averaged to produce non-local non-diffusive effective transport models; however, these non-diffusive models do not correspond with fractional transport, and it remains to be seen if the averaging process described in Ref. [Tar89] can be connected to fractional transport concepts.

In Chapter 5 the radial fractional model developed in Chapter 3 is applied to transport experiments performed in the following tokamak devices: Rijnhuizen Tokamak Project (RTP), ASDEX-Upgrade, JET, and DIII-D. This survey directly compares the effects of purely fractional diffusion models to conventional Fick's law diffusion, and thus provides an initial assessment of the presence of fractional transport phenomena in magnetic confinement experiments. For the steady-state heating experiments in RTP, the radial fractional model, with spatially uniform diffusivity χ_α, predicts hollow electron temperature profiles that are in good agreement with the measured temperature profiles. Moreover, it is found that the best fits to the experimental profiles are obtained when the order of the fractional diffusion parameter α decreases as the location of the off-axis power deposition moves outward.

In the power modulation experiments, the fractional model only achieves good agreement with the measurements for the high-frequency modulation in the purely Ohmic discharge #10589 in ASDEX-Upgrade for $\alpha = 1.75$. This disagreement suggests that fractional transport does not play a major part in determining the thermal waves excited in power modulation experiments. For the low-frequency modulation represented by discharges #10591 in ASDEX Upgrade and #55809 in JET, the fractional model predicts amplitude and phase profiles that are narrower than is observed. For both discharges, the critical gradient theory model fits the data better than the radial fractional model.

In modeling the recent DIII-D power modulation experiments, it is possible to reproduce quite well the amplitude and phase of the heat wave by choosing an appropriate profile for the modulation source. However, equally good fits can be obtained both with the fractional model, for $\alpha = 1.75$, and with conventional diffusion. However the larger source width required for the fractional fit is not realistic and suggests that the transport in this experiment may correspond to Fick's law.

APPENDIX A

Analytic details of the two dimensional isotropic operator

A.1 Asymptotic expansion of $\hat{\eta}$

In this appendix the leading order term of $\hat{\eta}(\epsilon\,|\vec{k}|) - 1$, in the limit $\epsilon \to 0$, is derived. This term depends only on the nature of the tails of $\eta(|\vec{x}|)$ in the limit $|\vec{x}| \to \infty$, or only on the assumption that

$$\frac{1}{\epsilon^2}\eta\left(|\vec{x}|/\epsilon\right) \sim \epsilon^{\alpha}/|\vec{x}|^{\alpha+2} \quad \text{as} \quad \epsilon \to 0 \ . \tag{A.1}$$

Starting with the Fourier transform of $\eta(|\vec{x}|)$

$$\begin{aligned}\hat{\eta}(\epsilon\,|\vec{k}|) &= \frac{1}{\epsilon^2}\int\int \eta(|\vec{x}|/\epsilon)\, e^{i\vec{k}\cdot\vec{x}}\,\mathrm{d}\vec{x} \\ &= \frac{1}{\epsilon^2}\int_0^{\infty}\int_0^{2\pi} re^{i|\vec{k}|rcos(\theta)}\,\eta(r/\epsilon)\,\mathrm{d}\theta\,\mathrm{d}r \ ,\end{aligned} \tag{A.2}$$

where $r = |\vec{x}|$ and using a coordinate system for the integration variable such that $\vec{k}\cdot\vec{x} = |\vec{k}|rcos(\theta)$, equation (A.2) can be rewritten as

$$\hat{\eta}(\epsilon|\vec{k}|) = 1 + \frac{1}{\epsilon^2}\int_0^{2\pi}\mathrm{d}\theta\int_0^{\infty} r\,\mathrm{d}r\ \eta(r/\epsilon)\left(e^{i|\vec{k}|\,r\,cos(\theta)} - 1 - i|\vec{k}|\,r\,cos(\theta)\right) \ , \tag{A.3}$$

using the two identities:

$$\begin{aligned}&\frac{1}{\epsilon^2}\int_0^{2\pi}\mathrm{d}\theta\int_0^{\infty} r\,\mathrm{d}r\ \eta(r/\epsilon) = 1 \\ &\int_0^{2\pi}\mathrm{d}\theta\int_0^{\infty} r\,\mathrm{d}r\ r|\vec{k}|\,cos(\theta)\,\eta(r/\epsilon) = 0 \ .\end{aligned} \tag{A.4}$$

Changing variables and dividing the range of integration gives

$$\begin{aligned}\hat{\eta}(\epsilon|\vec{k}|) - 1 = |\vec{k}|^{-2} \Bigg[&\int_0^{2\pi} \mathrm{d}\theta \int_0^{\delta} \mathrm{d}r \; r \; \epsilon^{-2} \eta\left(\frac{r}{\epsilon|\vec{k}|}\right) \left(e^{ir\,cos(\theta)} - 1 - ir\,cos(\theta)\right) \\ &+ \int_0^{2\pi} \mathrm{d}\theta \int_{\delta}^{\infty} \mathrm{d}r \; r \; \epsilon^{-2} \eta\left(\frac{r}{\epsilon|\vec{k}|}\right) \left(e^{ir\,cos(\theta)} - 1 - ir\,cos(\theta)\right) \Bigg] \; , \end{aligned} \tag{A.5}$$

where δ is a small parameter defined to obey the asymptotic relation:

$$\epsilon << \delta << 1 \; . \tag{A.6}$$

In the limit $\delta, \epsilon \to 0$, *while keeping* $\epsilon << \delta << 1$, the algebraic tail of η becomes the dominant contribution to the second integral of (A.5). The leading order behavior of this integral can be found by substituting (A.1) for η in its integrand. This substitution is valid since in the range of integration $r \in [\delta, \infty]$ the argument r/ϵ of η is always large, viz.,

$$\frac{r}{\epsilon} > \frac{\delta}{\epsilon} >> 1 \text{ for all } r \in [\delta, \infty] \; . \tag{A.7}$$

Substituting (A.1) into the second integral of (A.5) gives

$$\begin{aligned} |\vec{k}|^{-2} &\int_0^{2\pi} \mathrm{d}\theta \int_{\delta}^{\infty} \mathrm{d}r \; r \; \epsilon^{-2} \eta\left(\frac{r}{\epsilon|\vec{k}|}\right) \left(e^{ir\,cos(\theta)} - 1 - ir\,cos(\theta)\right) \\ &= \epsilon^{\alpha} \, |\vec{k}|^{\alpha} \int_0^{2\pi} \mathrm{d}\theta \int_{\delta}^{\infty} \mathrm{d}r \; r^{-1-\alpha} \left(e^{ir\,cos(\theta)} - 1 - ir\,cos(\theta)\right) \\ &= \epsilon^{\alpha} \, |\vec{k}|^{\alpha} \int_0^{2\pi} \mathrm{d}\theta \int_0^{\infty} \mathrm{d}r \; r^{-1-\alpha} \left(e^{ir\,cos(\theta)} - 1 - ir\,cos(\theta)\right) + \mathcal{O}(\epsilon^{\alpha}\,\delta^{2-\alpha}) \\ &\sim -\chi_{\alpha}\,\tau \; |\vec{k}|^{\alpha} \quad \text{as} \quad \delta, \epsilon \to 0 \; , \end{aligned} \tag{A.8}$$

where

$$\begin{aligned} \chi_{\alpha} &= \frac{\epsilon^{\alpha}}{\tau} \int_0^{2\pi} \mathrm{d}\theta \int_0^{\infty} \mathrm{d}r \; r^{-1-\alpha} \left(1 + ir\,cos(\theta) - e^{ir\,cos(\theta)}\right) \\ &= \frac{2\pi\,\epsilon^{\alpha}}{\tau} \int_0^{\infty} \mathrm{d}r \; r^{-1-\alpha} \left[1 - J_0(r)\right] \; . \end{aligned} \tag{A.9}$$

All that remains is to find the leading order behavior of the first integral in (A.5). In the limit $\delta, \epsilon \to 0$, this integral can be approximated by replacing the expression in the parentheses with the leading order term in its Taylor expansion about $\rho = 0$:

$$\begin{aligned}
&|\vec{k}|^{-2} \int_0^{2\pi} \mathrm{d}\theta \int_0^{\delta} \mathrm{d}r\ r\,\epsilon^{-2}\eta\left(\frac{r}{\epsilon|\vec{k}|}\right) \left(e^{ir\,cos(\theta)} - 1 - ir\ \cos(\theta)\right) \\
&\sim -\frac{(\epsilon|\vec{k}|)^{-2}}{2} \int_0^{2\pi} \mathrm{d}\theta\ \cos^2(\theta) \int_0^{\delta} \mathrm{d}r\ r^3\,\eta\left(\frac{r}{\epsilon|\vec{k}|}\right) \\
&\sim -\frac{(\epsilon|\vec{k}|)^{2}}{2} \int_0^{2\pi} \mathrm{d}\theta\ \cos^2(\theta) \int_0^{\delta/\epsilon|\vec{k}|} \mathrm{d}s\ s^3\,\eta\,(s)\ ,
\end{aligned} \tag{A.10}$$

where in the last line the change of variables $s = r/\epsilon|\vec{k}|$ is made. The leading order behavior of the s integral can be found by $\eta(s)$ with its asymptotic behavior (A.1). Integrating gives

$$\begin{aligned}
&|\vec{k}|^{-2} \int_0^{2\pi} \mathrm{d}\theta \int_0^{\delta} \mathrm{d}r\ r\,\epsilon^{-2}\eta\left(\frac{r}{\epsilon|\vec{k}|}\right) \left(e^{ir\,cos(\theta)} - 1 - ir\ \cos(\theta)\right) \\
&\sim -\frac{(\epsilon|\vec{k}|)^{2}}{2} \int_0^{2\pi} \mathrm{d}\theta\ \cos^2(\theta) \int^{\delta/\epsilon|\vec{k}|} \mathrm{d}s\ s^3\,s^{-\alpha-2} \\
&\sim -\frac{|\vec{k}|^{\alpha}}{2}\,\frac{\pi}{2-\alpha}\,\delta^{2-\alpha}\,\epsilon^{\alpha}
\end{aligned} \tag{A.11}$$

This contribution to the total Fourier transform can be neglected in the limit $\delta, \epsilon \to 0$, since $\delta^{2-\alpha} \to 0$, making this term asymptotically smaller than the contribution $-\epsilon^{\alpha}\,|\vec{k}|^{\alpha}$ that arises from the integration on $[\delta\ \infty]$. In conclusion, the leading order term is

$$\hat{\eta}(\epsilon|\vec{k}|) \sim 1 - \chi_{\alpha}\,\tau\,|\vec{k}|^{\alpha} \quad \text{as } \epsilon \to 0\ . \tag{A.12}$$

A.2 Inverse Fourier transform of $|\vec{k}|^{2-\alpha}$

The quantities $|\vec{k}|^{2-\alpha}$ and $|\vec{x}|^{-\alpha}$ form a Fourier transformation pair. Note:

$$\begin{aligned}
\mathcal{F}\left\{|\vec{x}|^{-\alpha}\right\} &= \int\int \; e^{i\vec{k}\cdot\vec{x}}\, |\vec{x}|^{-\alpha}\, \mathrm{d}\vec{x} \\
&= \int_0^{\infty} \; r\mathrm{d}r \int_0^{2\pi} \mathrm{d}\theta \; e^{i|\vec{k}|rcos(\theta)}\, r^{-\alpha} \\
&= |\vec{k}|^{\alpha-2} \int_0^{\infty} \; r\mathrm{d}r \int_0^{2\pi} \mathrm{d}\theta \; e^{ircos(\theta)}\, r^{-\alpha} \\
&= \gamma_\alpha\, |\vec{k}|^{\alpha-2} \; ,
\end{aligned} \tag{A.13}$$

where

$$\begin{aligned}
\gamma_\alpha &= \int_0^{\infty} \; r\mathrm{d}r \int_0^{2\pi} \mathrm{d}\theta \; e^{ircos(\theta)}\, r^{-\alpha} \\
&= 2\pi \int_0^{\infty} \; \mathrm{d}r\, r^{1-\alpha}\, J_0(r) \\
&= \pi\, 2^{2-\alpha}\, \frac{\Gamma(1-\alpha/2)}{\Gamma(\alpha/2)} \; .
\end{aligned} \tag{A.14}$$

A.3 Behavior of radial flux near the origin

The following appendix derives an asymptotic expansion of the flux for small r near the origin. The derivation starts with the intermediate finite domain quantity

$$I(r) = \int_0^{L} \mathrm{d}r'\, r'\, K_\alpha(r,r')\, P(r') \; , \tag{A.15}$$

where $K_\alpha(r,r')$ is the zeroth order kernel given in equation (3.23). For a bounded domain, the derivative of this expression is the negative of the flux for the masked Riemann-Liouville fractional operator for a suitably chosen $P(r)$; see (3.49). Taking the limit $L \to \infty$, equation (A.15) is also related to the unbounded domain flux (3.24).

Implementing a Taylor expansion $P(r)$ about $r = 0$,

$$I(r) = \sum_{m=0}^{\infty} \frac{P^{(m)}(0)}{m!} \int_0^L \mathrm{d}r'\, r'^{m+1}\, K_\alpha(r, r') \tag{A.16}$$

$$= \sum_{m=0}^{\infty} \frac{2\pi\, P^{(m)}(0)}{\gamma_\alpha m!} \left(I_m^{(1)} + I_m^{(2)} \right) , \tag{A.17}$$

where

$$I_m^{(1)} = \int_0^r \mathrm{d}r'\, \frac{r'^{1+m}}{r^\alpha}\, F\left(\frac{\alpha}{2}, \frac{\alpha}{2}; 1; \left(\frac{r'}{r} \right)^2 \right)$$

$$I_m^{(2)} = \int_r^L \mathrm{d}r'\, r'^{1-\alpha+m}\, F\left(\frac{\alpha}{2}, \frac{\alpha}{2}; 1; \left(\frac{r}{r'} \right)^2 \right) . \tag{A.18}$$

The integrals $I_m^{(1)}$ and $I_m^{(2)}$ can be found by using the Taylor series of the hypergeometric function and integrating term by term:

$$\begin{aligned} I_m^{(1)} &= \frac{1}{\Gamma(\alpha/2)^2} \sum_{j=0}^{\infty} \frac{\Gamma(\alpha/2 + j)^2}{(j!)^2} \int_0^r \frac{r'^{2j+m+1}}{r^{2j+\alpha}}\, \mathrm{d}r' \\ &= C_m\, r^{m+2-\alpha} , \end{aligned} \tag{A.19}$$

where

$$C_m = \frac{1}{\Gamma(\alpha/2)^2} \sum_{j=0}^{\infty} \frac{\Gamma(\alpha/2 + j)^2}{(j!)^2} \frac{1}{2j + m + 2} . \tag{A.20}$$

Also:

$$\begin{aligned} I_m^{(2)} &= \frac{1}{\Gamma(\alpha/2)^2} \sum_{j=0}^{\infty} \frac{\Gamma(\alpha/2 + j)^2}{(j!)^2} \int_r^L r'^{1-\alpha+m} \left(\frac{r}{r'} \right)^{2j} \mathrm{d}r' \\ &= \frac{L^{m+2-\alpha}}{\Gamma(\alpha/2)^2} \sum_{j=0}^{\infty} \frac{\Gamma(\alpha/2 + j)^2}{(j!)^2} \frac{1}{m + 2 - \alpha - 2j} \left(\frac{r}{L} \right)^{2j} - D_m\, r^{m+2-\alpha} , \end{aligned} \tag{A.21}$$

where

$$D_m \equiv \frac{1}{\Gamma(\alpha/2)^2} \sum_{j=0}^{\infty} \frac{\Gamma(\alpha/2 + j)^2}{(j!)^2} \frac{1}{m + 2 - \alpha - 2j} . \tag{A.22}$$

Combining these expressions in (A.17) gives:

$$\begin{aligned} I(r) = \sum_{m=0}^{\infty} & \frac{2\pi P^{(m)}(0)}{\gamma_\alpha\, m!} \left(C_m - D_m \right) r^{m+2-\alpha} \\ & + \sum_{m=0}^{\infty} \sum_{j=0}^{\infty} \frac{2\pi P^{(m)}(0)}{\gamma_\alpha\, m!} \frac{L^{m+2-\alpha}}{\Gamma(\alpha/2)^2} \frac{\Gamma(\alpha/2 + j)^2}{(j!)^2} \frac{1}{m + 2 - \alpha - 2j} \left(\frac{r}{L} \right)^{2j} . \end{aligned} \tag{A.23}$$

It should be noted that the infinite sums in the expressions for C_j and D_j converge for $\alpha < 2$, but not for $\alpha = 2$. For large j, the ratio of the gamma function and factorial in both sums becomes

$$\frac{\Gamma(j+\alpha/2)}{j!} = \frac{\Gamma(j+\alpha/2)}{\Gamma(j+1)} \sim j^{\alpha/2-1} \quad , \tag{A.24}$$

so that the magnitude of the terms decrease like $\sim j^{-p}$ with $p = 3 - \alpha > 1$, for $\alpha < 2$. When $p > 1$ the series converge. When $\alpha = 2$, $p = 1$ and both series diverge. Note that D_0 and C_0 are the Taylor expansions of hypergeometric functions evaluated at 1 and are equal to each other.

Commuting the order of summation in the final term results in

$$I(r) = \sum_{m=1}^{\infty} \frac{2\pi P^{(m)}(0)}{\gamma_\alpha\, m!} \left(C_m - D_m\right) r^{m+2-\alpha} + \sum_{j=0}^{\infty} \frac{2\pi}{\gamma_\alpha} G_j\, r^{2j} \ , \tag{A.25}$$

where

$$\begin{aligned} G_j &\equiv \frac{1}{\Gamma(\alpha/2)^2} \frac{\Gamma(\alpha/2+j)^2}{(j!)^2} \sum_{m=0}^{\infty} \frac{L^{m+2-\alpha-2j}}{m+2-\alpha-2j} \frac{P^{(m)}(0)}{m!} \\ &= \frac{1}{\Gamma(\alpha/2)^2} \frac{\Gamma(\alpha/2+j)^2}{(j!)^2} \left[\sum_{m=0}^{2j-1} \frac{L^{m+2-\alpha-2j}}{m+2-\alpha-2j} \frac{P^{(m)}(0)}{m!} \right. \\ &\qquad \left. + \int_0^L r^{1-\alpha-2j} \left(P(r) - \sum_{m=0}^{2j-1} \frac{P^{(m)}(0)}{m!} r^m \right) \mathrm{d}r \right] \ . \end{aligned} \tag{A.26}$$

The G_j are the only quantities that depend on L. In the limit $L \to \infty$ they reduce to

$$G_j = \frac{1}{\Gamma(\alpha/2)^2} \frac{\Gamma(\alpha/2+j)^2}{(j!)^2} \int_0^\infty r^{1-\alpha-2j} \left(P(r) - \sum_{m=0}^{2j-1} \frac{P^{(m)}(0)}{m!} r^m \right) \mathrm{d}r \ . \tag{A.27}$$

If $P(r)$ is integrable on the infinite domain, then the G_j's are finite; the singularity near the origin is integrable and at infinity the integrand scales as $\sim r^{-\alpha}$.

Finally, taking the negative of the derivative of (A.25) yields the behavior of the flux near the origin:

$$q(r) = -\frac{2\pi}{\gamma_\alpha} \sum_{m=1}^{\infty} \frac{P^{(m)}(0)}{m!} \left(C_m - D_m\right)(m+2-\alpha)\, r^{m+1-\alpha} - \frac{2\pi}{\gamma_\alpha} \sum_{m=1}^{\infty} 2mG_m\, r^{2m-1}$$
$$= \sum_{m=1}^{\infty} P^{(m)}(0)\, A_m\, r^{m+1-\alpha} + \sum_{m=1}^{\infty} B_m\, r^{2m-1} \ , \qquad \text{(A.28)}$$

where A_m and B_m are constants with respect to r.

A.4 Singular behavior of finite domain fractional Laplacian near boundary

This appendix extracts the leading order *singular* behavior near $r = L$ for the Riemann-Liouville fractional Laplacian in a finite domain (cf. expression (3.42))

$$^{R}\Delta_{r,L}^{\alpha/2} P(r) = \frac{1}{r}\frac{\partial}{\partial r}\left[r\,\frac{\partial}{\partial r}\int_0^L \mathrm{d}r'\, r' K_\alpha(r,r')\, P(r')\right] \ , \qquad \text{(A.29)}$$

which appears in Chapter 3.2.4. Only the singular terms of the expansion of (A.29) near L are calculated; the full asymptotic expansion is too tedious to work out completely. To find these singular terms, the intermediate quantity

$$I(r) \equiv \int_0^L \mathrm{d}r'\, r'\, K_\alpha(r,r')\, P(r') \ , \qquad \text{(A.30)}$$

is expanded about $r = L$ to obtain the leading order, non-analytic terms whose derivatives are singular at $r = L$. To that end, the integral $I(r)$ is divided into two pieces:

$$I(r) = \frac{2\pi}{\gamma_\alpha}\left[I_1(r) + I_2(r)\right] \ ,$$

where

$$I_1(r) \equiv \int_0^r \mathrm{d}r'\, \frac{r'}{r^\alpha}\, F\left(\frac{\alpha}{2},\frac{\alpha}{2};1;\left(\frac{r'}{r}\right)^2\right) P(r')$$
$$I_2(r) \equiv \int_r^L \mathrm{d}r'\, r'^{1-\alpha}\, F\left(\frac{\alpha}{2},\frac{\alpha}{2};1;\left(\frac{r}{r'}\right)^2\right) P(r') \ .$$

In the first integral, the change of variables

$$s = \frac{L}{r}\, r'$$

yields:

$$I_1(r) = \frac{r^{2-\alpha}}{L^2} \int_0^L \mathrm{d}s\, s\, F\left(\frac{\alpha}{2}, \frac{\alpha}{2}; 1; \left(\frac{s}{L}\right)^2\right) P\left(\frac{rs}{L}\right) \ . \tag{A.31}$$

Replacing the r in the argument of P with $r = r - L + L$, and expanding in the small parameter $r - L$ obtains

$$I_1(r) = \frac{r^{2-\alpha}}{L^2} \sum_{m=0}^{\infty} \frac{1}{m!} \left(\frac{r-L}{L}\right)^m \int_0^L \mathrm{d}s\, s\, F\left(\frac{\alpha}{2}, \frac{\alpha}{2}; 1; \left(\frac{s}{L}\right)^2\right) P^{(m)}(s) \ . \tag{A.32}$$

From this expression for $I_1(r)$, it can be concluded that $I_1(r)$ is analytic at $r = L$ and that all derivatives of $I_1(r)$ are non-singular.

In the second integral, the following change of variables is made,

$$s = \left(\frac{r}{r'}\right)^2 \ , \tag{A.33}$$

giving,

$$I_2(r) = \frac{1}{2}\, r^{2-\alpha} \int_{(r/L)^2}^{1} \mathrm{d}s\, s^{\alpha/2-2}\, F\left(\frac{\alpha}{2}, \frac{\alpha}{2}; 1; s\right) P\left(\frac{r}{\sqrt{s}}\right) \ . \tag{A.34}$$

When $(r - L)/L << 1$, the interval $[(r/L)^2, 1]$ is small and thus the terms in the integrands can be approximated by expansions around $s = 1$:

$$s^{\alpha/2-2}\, P\left(\frac{r}{\sqrt{s}}\right) = P(r) + \left[\left(\frac{\alpha}{2} - 2\right) P(r) - \frac{1}{2}\, r\, P'(r)\right] (s-1) + \sum_{m=2}^{\infty} p_m\, (s-1)^m \ ,$$

$$F\left(\frac{\alpha}{2}, \frac{\alpha}{2}; 1; s\right) = \sum_{m=0}^{\infty} a_m\, (1-s)^m + b_m\, (1-s)^{m+1-\alpha} \ ,$$

where

$$\begin{aligned}
a_m &= \frac{1}{m!} \frac{\Gamma(1-\alpha)}{\Gamma(1-\alpha/2)^2} \frac{\Gamma(\alpha)}{\Gamma(\alpha/2)^2} \frac{\Gamma(\alpha/2+m)^2}{\Gamma(\alpha+m)} \\
b_m &= \frac{1}{m!} \frac{\Gamma(\alpha-1)}{\Gamma(\alpha/2)^2} \frac{\Gamma(2-\alpha)}{\Gamma(1-\alpha/2)^2} \frac{\Gamma(1-\alpha/2+m)^2}{\Gamma(2-\alpha+m)} \\
p_m &= \frac{1}{m!} \frac{d^m}{ds^m}\, s^{\alpha/2-2}\, P\left(\frac{r}{\sqrt{s}}\right)\Bigg|_{s=1} \ .
\end{aligned}$$

Substituting these expansions into the equation for I_2, gives

$$I_2(r) = \frac{1}{2}\, r^{2-\alpha}\, \left[f_1(r)\, P(r) - f_2(r)\, \left(\left(\frac{\alpha}{2} - 2 \right)\, P(r) - \frac{1}{2} r\, P'(r) \right) + f_3(r) \right] \;,$$

where

$$\begin{aligned} f_1(r) &= \sum_{m=0}^{\infty}\, \frac{a_m}{m+1}\, \left(1 - \frac{r^2}{L^2}\right)^{m+1} + \frac{b_m}{m+2-\alpha}\, \left(1 - \frac{r^2}{L^2}\right)^{m+2-\alpha} \;, \\ f_2(r) &= \sum_{m=0}^{\infty}\, \frac{a_m}{m+2}\, \left(1 - \frac{r^2}{L^2}\right)^{m+2} + \frac{b_m}{m+3-\alpha}\, \left(1 - \frac{r^2}{L^2}\right)^{3+m-\alpha} \;, \\ f_3(r) &= \sum_{j=0}^{\infty}\, \sum_{m=2}^{\infty}\, (-1)^m\, p_m\, \left(\frac{a_j}{j+m+1}\, \left(1 - \frac{r^2}{L^2}\right)^{j+m+1} \right. \\ &\qquad\qquad \left. + \frac{b_j}{j+m+2-\alpha}\, \left(1 - \frac{r^2}{L^2}\right)^{j+m+2-\alpha} \right) \;. \end{aligned}$$

The leading order terms of the above expansion that become singular after differentiation are as follows:

$$\begin{aligned} I_2(r) &= \frac{1}{2}\left(\frac{r}{L}\right)^{2-\alpha}\, \left[\frac{b_0}{2-\alpha} P(r) \left(1 + \frac{r}{L}\right)^{2-\alpha}\, (L-r)^{2-\alpha} + \frac{1}{L}\, \frac{1}{3-\alpha} \times \right. \\ &\quad \left. \left[\left[b_1 - \left(\frac{\alpha}{2} - 2\right)\, b_0 \right]\, P(r) + \frac{1}{2} b_0 r P'(r) \right]\, \left(1 + \frac{r}{L}\right)^{3-\alpha}\, (L-r)^{3-\alpha} \right] + \ldots \\ &\sim c_1\, P(L)\, (L-r)^{2-\alpha} + \left[c_2\, P(L) + c_3\, P'(L)\right]\, (L-r)^{3-\alpha} + o\left[(r-L)^{3-\alpha}\right] \;, \end{aligned}$$

where in the second line the functions multiplying $(L-r)^{2-\alpha}$ and $(L-r)^{3-\alpha}$ have been expanded about $r = L$, and where the c_i's are constants (not shown). From this equation the leading order singular expansion of (A.29) is

$$\begin{aligned} &{}^{R}\Delta_{r,L}^{\alpha/2} P(r) \sim \\ &\frac{2\pi}{\gamma_\alpha}\, \left(-\frac{1}{L}\, (2-\alpha)\, c_1\, P(L) + (2-\alpha)\, (3-\alpha)\, \left[c_2\, P(L) + c_3\, P'(L)\right] \right)\, (L-r)^{1-\alpha} \\ &\qquad + \frac{2\pi}{\gamma_\alpha}\, (2-\alpha)\, (1-\alpha)\, c_1\, P(L)\, (L-r)^{-\alpha} + \ldots \;. \end{aligned} \tag{A.35}$$

APPENDIX B

Numerical Method

In this section a discretization scheme is developed for the masked Riemann-Liouville operator that is part of the bounded domain fractional operator (3.48). The scheme can be used to obtain numerical solutions of the bounded domain fractional diffusion equation (3.52). The method allows for a spatially varying fractional diffusivity $\chi_\alpha(r)$ and is based on separating the Riemann-Liouville operator into its two constituent operators: the conventional Laplacian and the *(radial) Riesz fractional integration operator* [SKM93]. In particular, the method requires appropriately discretizing the Riesz integral operator. The starting point is

$$\frac{1}{r}\frac{\partial}{\partial r}\left[r\,\chi_\alpha(r)\,\frac{\partial}{\partial r}\int_0^L r' K_\alpha(r,r')\,H_\alpha(r')\,P(r')\,\mathrm{d}r'\right] = \Delta_{r,\chi}\,I^{2-\alpha}_{Riesz}\,H_\alpha(r)P(r)\ , \tag{B.1}$$

where the Riesz fractional integration is defined as

$$I^{2-\alpha}_{Riesz}\,P(r) \equiv \int_0^L \mathrm{d}r'\,r'\ K_\alpha(r,r')\,P(r')\ , \tag{B.2}$$

and where

$$\Delta_{r,\chi}\,P(r) = \frac{1}{r}\frac{\partial}{\partial r}\,r\chi_\alpha(r)\,\frac{\partial}{\partial r}\,P(r)\ . \tag{B.3}$$

On a mesh of $N+1$ points with grid spacing $h = L/N$, the fractional Riesz integral operator can be approximated as

$$\begin{aligned}
\left[I^{2-\alpha}_{Riesz}\, H_\alpha(r)\, P(r)\right]_k = & \sum_{n=1}^{N-1} \int_{hn-h/2}^{hn+h/2} r'\, K_\alpha(hk, r')\, H_\alpha(r')\, P(r')\, \mathrm{d}r' \\
& + \int_0^{h/2} r'\, K_\alpha(hk, r')\, H_\alpha(r')\, P(r')\, \mathrm{d}r' \\
& + \int_{L-h/2}^{L} r'\, K_\alpha(hk, r')\, H_\alpha(r')\, P(r')\, \mathrm{d}r' \\
\approx & \; h^{2-\alpha} \sum_{n=1}^{N-1} M_{kn}\, P_n + h^{2-\alpha}\, V_k^{(0)}\, P_0 \ ,
\end{aligned} \tag{B.4}$$

where P_n is the value of P at the grid point $r = hn$, and the arrays M_{kn} and $V_k^{(0)}$ are defined as

$$\begin{aligned}
M_{kn} &\equiv H_\alpha(hn) \int_{n-1/2}^{n+1/2} s\, K_\alpha(k, s)\, \mathrm{d}s \ , \\
V_k^{(0)} &= H_\alpha(0) \int_0^{1/2} s\, K_\alpha(k, s)\, \mathrm{d}s \ .
\end{aligned} \tag{B.5}$$

The integral term with limits $[L - h/2,\, L]$ is dropped since $H_\alpha(L) = H'_\alpha(L) = 0$. The integrals in the expressions for the weights M_{kn} and $V_k^{(0)}$ can be performed exactly:

$$\begin{aligned}
M_{kn} &= \frac{H_\alpha(hn)}{\gamma_\alpha} \begin{cases} \dfrac{2\pi}{2-\alpha}\, s^{2-\alpha}\, F\left[\dfrac{\alpha}{2}, \dfrac{\alpha}{2} - 1; 1; \left(\dfrac{k}{s}\right)^2\right] \Bigg|_{s=n-1/2}^{s=n+1/2} & k < n \\ \dfrac{2\pi}{2-\alpha}\, (k+1/2)^{2-\alpha}\, F\left[\dfrac{\alpha}{2}, \dfrac{\alpha}{2} - 1; 1; \left(\dfrac{k}{k+1/2}\right)^2\right] \dots & \\ \qquad \dots - \dfrac{\pi}{k^\alpha}\, (k-1/2)^2\, F\left[\dfrac{\alpha}{2}, \dfrac{\alpha}{2}; 2; \left(\dfrac{k-1/2}{k}\right)^2\right] & k = n \\ \dfrac{\pi}{k^\alpha}\, s^2\, F\left[\dfrac{\alpha}{2}, \dfrac{\alpha}{2}; 2; \left(\dfrac{s}{k}\right)^2\right] \Bigg|_{s=n-1/2}^{s=n+1/2} & k > n \end{cases} \\
V_k^{(0)} &= \frac{H_\alpha(0)}{\gamma_\alpha}\, \frac{\pi}{k^\alpha}\, s^2\, F\left[\frac{\alpha}{2}, \frac{\alpha}{2}; 2; \left(\frac{s}{k}\right)^2\right] \Bigg|_{s=0}^{s=1/2} \qquad k > 0 \ .
\end{aligned} \tag{B.6}$$

The outer conventional Laplacian part of the operator can be approximated using the standard central differencing scheme. The Riemann-Liouville operator can be approximated at a grid point $r = hk$ as

$$\begin{aligned}\left[\Delta_{r,\chi}\, I^{2-\alpha}_{Riesz}\, H_\alpha(r)P(r)\right]_k = &\sum_{n=1}^{N-1} \frac{1}{h^2}\, L_{kn}\, \left[I^{2-\alpha}_{Riesz}\, H_\alpha(r)\, P(r)\right]_n \\ &+ \frac{1}{2}\,\frac{1}{h^2}\,\chi_{1/2}\, \left[I^{2-\alpha}_{Riesz}\, H_\alpha(r)\, P(r)\right]_0 \delta_{k,1} \\ &+ \frac{1}{h^2}\,\frac{N-1/2}{N-1}\,\chi_{N-1/2}\, \left[I^{2-\alpha}_{Riesz}\, H_\alpha(r)\, P(r)\right]_N \delta_{k,N-1}\ ,\end{aligned} \tag{B.7}$$

where the array L_{kn} is defined as

$$\begin{aligned}L_{kn} \equiv &\frac{k+1/2}{k}\,\chi_{k+1/2}\,\delta_{k+1,n} - \left[\frac{k+1/2}{k}\,\chi_{k+1/2} + \frac{k-1/2}{k}\,\chi_{k-1/2}\right]\delta_{k,n} \\ &+ \frac{k-1/2}{k}\,\chi_{k-1/2}\,\delta_{k-1,n}\ ,\end{aligned} \tag{B.8}$$

and where $\chi_k \equiv \chi_\alpha(hk)$. Note that $\delta_{k,n}$ are Kronecker-delta functions. The boundary condition

$$\left.\frac{\partial}{\partial r}P(r)\right|_0 = 0\ , \tag{B.9}$$

requires that $P_0 = P_1$. The previous expressions can be succinctly rewritten as the product of matrices

$$\left[\Delta_{r,\chi}\, I^{2-\alpha}_{Riesz}\, H_\alpha(r)P(r)\right]_k = h^{-\alpha}\, \left[(\mathcal{L}\,\mathcal{M} + \mathcal{B}_1 + \mathcal{B}_2)\ P\right]_k\ , \tag{B.10}$$

where $\mathcal{M}$ and $\mathcal{L}$ are matrices of the arrays M_{nk} and L_{nk}, respectively, on the index range $n, k = 1 \ldots N-1$, and where $\mathcal{B}_1$ and $\mathcal{B}_2$ are boundary matrices defined as

$$\mathcal{B}_1 \equiv \begin{pmatrix} C_0\, M_{0,1} & C_0\, M_{0,2} & \ldots & C_0\, M_{0,N-2} & C_0\, M_{0,N-1} \\ 0 & 0 & \ldots & 0 & 0 \\ 0 & 0 & \ldots & 0 & 0 \\ \vdots & \vdots & \text{(zeros)} & \vdots & \vdots \\ 0 & 0 & \ldots & 0 & 0 \\ 0 & 0 & \ldots & 0 & 0 \\ C_N\, M_{N,1} & C_N\, M_{N,2} & \ldots & C_N\, M_{N,N-2} & C_N\, M_{N,N-1} \end{pmatrix}\ ,$$

and

$$\mathcal{B}_2 \equiv \begin{pmatrix} \sum_{n=1}^{N-1} L_{1,n} V_n^{(0)} + \frac{1}{2}\,\chi_{1/2}\,V_0^{(0)}, & 0 & 0 & \dots & 0 \\ \sum_{n=1}^{N-1} L_{2,n} V_n^{(0)}, & 0 & 0 & \dots & 0 \\ \vdots & \vdots & \vdots & \ddots & \vdots \\ \sum_{n=1}^{N-1} L_{N-2,n} V_n^{(0)}, & 0 & 0 & \dots & 0 \\ \sum_{n=1}^{N-1} L_{N-1,n} V_n^{(0)} + \frac{N-1/2}{N-1}\,\chi_{N-1/2}\,V_N^{(0)}, & 0 & 0 & \dots & 0 \end{pmatrix} .$$

The first boundary matrix $\mathcal{B}_1$ is zero except for the first and last rows; this matrix accounts for the last two terms in (B.7). The constants that appear in the expression for $\mathcal{B}_1$ are defined as

$$C_0 = \frac{1}{2}\,\chi_{1/2}\ , \quad C_N = \frac{N-1/2}{N-1}\,\chi_{N-1/2}\ . \tag{B.11}$$

The second boundary matrix $\mathcal{B}_2$ is nonzero only for the first column; this first column is the vector $\sum_{n=1}^{N-1} L_{k,n} V_n^{(0)}$ plus two extra terms that appear on the first and last row only. The matrix $\mathcal{B}_2$ enforces the boundary condition (B.9).

Equation (B.10) approximates the masked Riemann-Liouville operator that is part of the fractional Laplacian defined in (3.48). When the boundary layer diffusion operator is included, the complete scheme takes the form

$$\left[\Delta_{r,L}^{\alpha/2} P(r)\right]_k = [\mathcal{F} P]_k + P_N\,\mathcal{V}_k\ , \tag{B.12}$$

where the vector $\mathcal{V}_k$ represents the contribution to the approximation due to the Dirichlet boundary condition at $r = L$ and where the matrix $\mathcal{F}$ is given by

$$\mathcal{F} = h^{-\alpha}\,[\mathcal{L}\ \mathcal{M} + \mathcal{B}_1 + \mathcal{B}_2] + \zeta\,h^{-2}\,\mathcal{H}_{boundary}\ , \tag{B.13}$$

where $\mathcal{H}_{boundary}$ is a matrix representation of the central differencing scheme that approximates the boundary layer diffusion operator. The time dependent diffusion equation can be solved using a fully time-implicit scheme, i.e., the solution is advanced to time $t_{m+1} = \Delta t\,(m+1)$ via the matrix equation

$$\frac{P_k^{m+1} - P_k^m}{\Delta t} = [\mathcal{F}\,P]_k^{m+1} + P_N\,\mathcal{V}_k\ . \tag{B.14}$$

Solving for P_k^{m+1} results in

$$P_k^{m+1} = [1 - \Delta t\, \mathcal{F}]^{-1}\ [P_k^m + \Delta t\, P_N\, \mathcal{V}_k]\ . \tag{B.15}$$

APPENDIX C

Isotropic fractional diffusion in three dimensions

In this section, the derivation of a 3D fractional Laplacian is briefly sketched and the resulting operator and its expansion into spherical harmonics is given. This derivation follows the same line of reasoning presented in Chapter 3, although the mathematical details are not shown. No applications of this 3D formalism have yet been explored.

The derivation starts with the Montroll-Wiess master equation associated with the CTRW model in three dimensions:

$$\frac{\partial}{\partial t} P(\vec{x}, t) = \frac{1}{\tau} \int\int\int_{\Re^3} \eta(\vec{x} - \vec{x}')\, P(\vec{x}', t)\, \mathrm{d}V - \frac{1}{\tau}\, P(\vec{x}, t) \ . \tag{C.1}$$

This equation describes Markovian transport in terms of a general jump or displacement PDF $\eta(\vec{x})$ and average waiting time τ. As in the 2D derivation, two assumptions are made concerning the PDF $\eta(\vec{x})$: first, the displacements are isotropic, i.e., $\eta(\vec{x}) = \eta(|\vec{x}|)$ and second $\eta(|\vec{x}|)$ has algebraically decaying tails such that the second and higher moments diverge, i.e.,

$$\eta(|\vec{x}|) \sim \frac{1}{|\vec{x}|^{\alpha+3}} \ . \tag{C.2}$$

When equation (C.1) is transformed into Fourier space, it can be shown that the long wavelength fluid limit of $\epsilon^{-3}\eta(|\vec{x}|/\epsilon)$, with tails (C.2), is given by

$$\hat{\eta}(\epsilon\, |\vec{k}|) \sim 1 - \chi_\alpha\, \tau\, |\vec{k}|^\alpha \quad \text{as } \epsilon\, |\vec{k}| \to 0 \ , \tag{C.3}$$

and the fluid limit of the master equation in Fourier space becomes

$$\frac{\partial}{\partial t} \hat{P}(\vec{k}, t) = -\chi_\alpha\, |\vec{k}|^\alpha\, \hat{P}(\vec{k}, t) \ . \tag{C.4}$$

The expression on the right hand side of (C.4) is the Fourier transform of the 3D fractional Laplacian:

$$\mathcal{F}\left\{\Delta^{\alpha/2}\,P\right\} = -|\vec{k}|^{\alpha}\,\hat{P}\ . \tag{C.5}$$

When (C.5) is inverted back to configuration space, the following expression for the 3D fractional Laplacian is obtained

$$\begin{aligned}\Delta^{\alpha/2}\,P(\vec{x}) &= \Delta\int\int\int_{\Re^3}\frac{1}{\gamma_\alpha}\,\frac{P(\vec{x}')}{|\vec{x}-\vec{x}'|^{\alpha+1}}\,\mathrm{d}\vec{x}' \\ &= \int\int\int_{\Re^3}\frac{1}{\gamma_\alpha}\,\frac{\Delta'\,P(\vec{x}')}{|\vec{x}-\vec{x}'|^{\alpha+1}}\,\mathrm{d}\vec{x}'\ ,\end{aligned} \tag{C.6}$$

where

$$\gamma_\alpha = (2\pi)^{3/2}\,2^{1/2-\alpha}\,\frac{\Gamma\left(\frac{2-\alpha}{2}\right)}{\Gamma\left(\frac{1+\alpha}{2}\right)}\ . \tag{C.7}$$

It should be noted that in the infinite domain both expressions given in (C.6) are equivalent.

The 3D fractional Laplacian operator in (C.6) can be expanded into spherical harmonics $Y_{lm}(\theta,\phi)$[Jac99]:

$$\begin{aligned}\Delta^{\alpha/2}\,P(r,\theta,\phi) = \Delta\sum_{l=0}^{\infty}\sum_{m=-l}^{l}&\frac{2\pi}{\gamma_\alpha}\,\frac{\Gamma\left(\frac{1}{2}\right)\,\Gamma\left(l+\frac{\alpha+1}{2}\right)}{\Gamma\left(\frac{\alpha+1}{2}\right)\,\Gamma\left(l+\frac{3}{2}\right)} \\ &\left\{\int_0^\infty \mathrm{d}r'\,\frac{r'^2}{r_>^{\alpha+1}}\,\rho^l\,F\left[\frac{\alpha}{2},\frac{\alpha+1}{2};l+\frac{3}{2};\rho^2\right]\,P_{lm}(r')\right\}\,Y_{lm}(\theta,\phi)\ ,\end{aligned} \tag{C.8}$$

where $r_< = \min\{r,r'\}$, $r_> = \max\{r,r'\}$, and $\rho = \frac{r_<}{r_>}$. In (C.8) the function $F(a,b;c,z)$ is Gauss' hypergeometric function[AS72], and P_{lm} is given by

$$P_{lm}(r) = \int \mathrm{d}\Omega\,Y^*_{lm}(\theta,\phi)\,P(r,\theta,\phi)\ . \tag{C.9}$$

REFERENCES

[APG04] C. Angioni, A.G. Peeters, X. Garbet, A. Manini, F. Ryter, and ASDEX Upgrade Team. "Density response to central electron heating: theoretical investigations and experimental observations in ASDEX Upgrade." *Nuclear Fusion*, **44**(8):827, 2004.

[AS72] M. Abramowitz and I. Stegun. *Handbook of Mathematical Functions.* Dover, 1972.

[BBH99] M. R. de Baar, M. N. A. Beurskens, G. M. D. Hogeweij, and N. J. Lopes Cardozo. "Tokamak plasmas with dominant electron cyclotron heating; evidence for electron thermal transport barriers." *Phys. Plasmas*, **6**(12):4645–4657, 1999.

[BMM00] A. T. Burke, J. E. Maggs, and G. J. Morales. "Experimental study of fluctuations excited by a narrow temperature filament in a magnetized plasma." *Phys. Plasmas*, **7**(5):1397–1407, 2000.

[BSC04] R. Bruno, L. Sorriso-Valvo, V. Carbone, and B. Bavassano. "A possible truncated-Lévy-flight statistics recovered from interplanetary solar-wind velocity and magnetic-field fluctuations." *EPL (Europhysics Letters)*, **66**(1):146, 2004.

[Cas] D. del Castillo-Negrete. *Anomalous Transport in the Presence of Truncated Lévy Flights*, chapter 6, pp. 129–157.

[Cas98] D. del Castillo-Negrete. "Asymmetric transport and non-Gaussian statistics of passive scalars in vortices in shear." *Physics of Fluids*, **10**(3):576–594, 1998.

[Cas06] D. del Castillo-Negrete. "Fractional diffusion models of nonlocal transport." *Phys. Plasmas*, **13**(8):082308, 2006.

[Cas08] D. del Castillo-Negrete. "Non-diffusive transport modeling: statistical basis and applications." *AIP Conference Proceedings*, **1013**(1):207–239, 2008.

[Cas09] D. del Castillo-Negrete. "Truncation effects in superdiffusive front propagation with Lévy flights." *Phys. Rev. E*, **79**:031120, Mar 2009.

[CC07] A. Cartea and D. del Castillo-Negrete. *Phys. Rev. E*, **76**(041105), 2007.

[CCL04] D. del Castillo-Negrete, B. A. Carreras, and V. E. Lynch. "Fractional diffusion in plasma turbulence." *Phys. Plasmas*, **11**(8):3854–3864, 2004.

[CCL05] D. del Castillo-Negrete, B. A. Carreras, and V. E. Lynch. “Nondiffusive Transport in Plasma Turbulence: A Fractional Diffusion Approach.” *Phys. Rev. Lett.*, **94**:065003, 2005.

[CG00] A. V. Chechkin and V. Yu. Gonchar. “Linear relaxation processes governed by fractional symmetric kinetic equations.” *J. Eksp. Theor. Phys.*, **118**:730, 2000.

[CGC08] D. del Castillo-Negrete, V.Yu. Gonchar, and A.V. Chechkin. “Fluctuation-driven directed transport in the presence of Lvy flights.” *Physica A: Statistical Mechanics and its Applications*, **387**(27):6693 – 6704, 2008.

[CGK02] A. Chechkin, V. Gonchar, J. Klafter, R. Metzler, and L. Tanatarov. “Stationary states of non-linear oscillators driven by Lévy noise.” *Chemical Physics*, **284**(12):233 – 251, 2002.

[CGK05] A. V. Chechkin, V. Yu. Gonchar, J. Klafter, and R. Metzler. “Barrier crossing of a Lévy flight.” *EPL (Europhysics Letters)*, **72**(3):348, 2005.

[CLZ01] B. A. Carreras, V. E. Lynch, and G. M. Zaslavsky. “Anomalous diffusion and exit time distribution of particle tracers in plasma turbulence model.” *Phys. Plasmas*, **8**(12):5096–5103, 2001.

[CMN08] D. del Castillo-Negrete, P. Mantica, V. Naulin, and J.J. Rasmussen. “Fractional diffusion models of non-local perturbative transport: numerical results and application to JET experiments.” *Nucl. Fusion*, **48**(7):075009, 2008.

[DGH07] B. Dybiec, E. Gudowska-Nowak, and P. Hänggi. “Escape driven by α-stable white noises.” *Phys. Rev. E*, **75**:021109, Feb 2007.

[DGS08] B. Dybiec, E. Gudowska-Nowak, and I. M. Sokolov. “Transport in a Lévy ratchet: Group velocity and distribution spread.” *Phys. Rev. E*, **78**:011117, Jul 2008.

[Dit99] P. D. Ditlevsen. “Anomalous jumping in a double-well potential.” *Phys. Rev. E*, **60**:172–179, Jul 1999.

[DL98] B. Dubrulle and J.-P. Laval. “Truncated Lévy laws and 2D turbulence.” *The European Physical Journal B - Condensed Matter and Complex Systems*, **4**(2):143–146, 1998.

[DPW12] J. C. DeBoo, C.C. Petty, A.E. White, K.H. Burrell, E.J. Doyle, J.C. Hillesheim, C. Holland, G.R. McKee, T.L. Rhodes, L. Schmitz, S.P. Smith, G. Wang, and L. Zeng. “Electron profile stiffness and critical gradient studies.” *Phys. Plasmas*, **19**(082518), 2012.

[DS07] A. Dubkov and B. Spagnolo. "Langevin approach to Lévy flights in fixed potentials: exact results for stationary probability distributions." *Acta Phys. Pol. B*, **38**:1745, 2007.

[Dyb08] B. Dybiec. "Current inversion in the Lévy ratchet." *Phys. Rev. E*, **78**:061120, Dec 2008.

[GC06] L. Garcia and B. A. Carreras. "Mesoscale transport properties induced by near critical resistive pressure-gradient-driven turbulence in toroidal geometry." *Phys. Plasmas*, **13**(2):022310, 2006.

[Gen95] K. W. Gentle et al. "An experimental counter-example to the local transport paradigm." *Phys. Plasmas*, **2**(6):2292–2298, 1995.

[Gon03] V.Yu. Gonchar et al. "Stable Lévy distributions of the density and potential fluctuations in the edge plasma of the U-3M torsatron." *Plasma Phys. Rep.*, **29**:380–390, 2003.

[Gor08] Claude Gormezano, editor. *Special Issue on Joint European Torus (JET).* Fusion Science and Technology, 2008. Vol. 53, No. 4.

[GR80] I. S. Gradshteyn and I. M. Ryzhik. *Table of integrals, series, and products.* Academic Press, 4 edition, 1980.

[HCB98] G.M.D. Hogeweij, N.J. Lopes Cardozo, M.R. De Baar, and A.M.R. Schilham. "A model for electron transport barriers in tokamaks, tested against experimental data from RTP." *Nuclear Fusion*, **38**(12):1881, 1998.

[HDP13] J. C. Hillesheim, J. C. DeBoo, W. A. Peebles, T. A. Carter, G. Wang, T. L. Rhodes, L. Schmitz, G. R. McKee, Z. Yan, G. M. Staebler, K. H. Burrell, E. J. Doyle, C. Holland, C. C. Petty, S. P. Smith, A. E. White, and L. Zeng. "Observation of a Critical Gradient Threshold for Electron Temperature Fluctuations in the DIII-D Tokamak." *Phys. Rev. Lett.*, **110**:045003, Jan 2013.

[HS12] J. A. Huwaldt and S. Steinhorst. "Plot Digitizer." http://plotdigitizer.sourceforge.net, December 2012. Version 2.6.2.

[IP06] Peter Imkeller and Ilya Pavlyukevich. "Lévy flights: transitions and meta-stability." *Journal of Physics A: Mathematical and General*, **39**(15):L237, 2006.

[IRG01] F Imbeaux, F Ryter, and X Garbet. "Modelling of ECH modulation experiments in ASDEX Upgrade with an empirical critical temperature gradient length transport model." *Plasma Physics and Controlled Fusion*, **43**(11):1503, 2001.

[Jac99] John David Jackson. *Classical Electrodynamics.* Wiley, third edition, 1999.

[JKK03] R. Jha, P. K. Kaw, D. R. Kulkarni, and J. C. Parikh. “Evidence of Lévy stable process in tokamak edge turbulence.” *Phys. Plasmas*, **10**(3):699–704, 2003.

[JMF99] Sune Jespersen, Ralf Metzler, and Hans C. Fogedby. “Lévy flights in external force fields: Langevin and fractional Fokker-Planck equations and their solutions.” *Phys. Rev. E*, **59**:2736–2745, Mar 1999.

[KBD99] Dimitri Kusnezov, Aurel Bulgac, and Giu Do Dang. “Quantum Lévy Processes and Fractional Kinetics.” *Phys. Rev. Lett.*, **82**:1136–1139, 1999.

[Kop95] Ismo Koponen. “Analytic approach to the problem of convergence of truncated Lévy flights towards the Gaussian stochastic process.” *Phys. Rev. E*, **52**:1197–1199, Jul 1995.

[MCD04] T. K. March, S. C. Chapman, R. O. Dendy, and J. A. Merrifield. “Off-axis electron cyclotron heating and the sandpile paradigm for transport in tokamak plasmas.” *Physics of Plasmas*, **11**(2):659–665, 2004.

[MCG08] P. Mantica, G. Corrigan, X. Garbet, F. Imbeaux, J. Lonnroth, V. Parail, T. Tala, A. Taroni, M. Valisa, and H. Weisen. “Core Transport Studies in JET.” *Fusion Science and Technology*, **53**(4):1152–1216, 2008.

[MK00] Ralf Metzler and Joseph Klafter. “The random walk’s guide to anomalous diffusion: a fractional dynamics approach.” *Phys Rep.*, **339**(1):1 – 77, 2000.

[MK04] Ralf Metzler and Joseph Klafter. “The restaurant at the end of the random walk: recent developments in the description of anomalous transport by fractional dynamics.” *J. Phys. A: Math. Gen.*, **37**:R161 – R208, 2004.

[MR06] Paola Mantica and Franois Ryter. “Perturbative studies of turbulent transport in fusion plasmas.” *C. R. Physique*, **7**(6):634 – 649, 2006.

[MS94] Rosario N. Mantegna and H. Eugene Stanley. “Stochastic Process with Ultraslow Convergence to a Gaussian: The Truncated Lévy Flight.” *Phys. Rev. Lett.*, **73**:2946–2949, Nov 1994.

[MS95] R. N. Mantegna and H. E. Stanley. “Scaling behaviour in the dynamics of an economic index.” *Nature*, **376**:46–49, 1995.

[OS74] K. B. Oldham and J. Spanier. *The Fractional Calculus.* Academic Press, 1974.

[Pes87] Frank E. Peseckis. “Statistical dynamics of stable processes.” *Phys. Rev. A.*, **36**:892–902, 1987.

[Pod99] I. Podlubny. *Fractional Differential Equations.* Academic Press, 1999.

[PS08] Grigorios A. Pavliotis and Andrew M. Stuart. *Multiscale Methods: Averaging and Homogenization*, volume 53 of *Texts in Applied Mathematics.* New York, Springer, 2008.

[PSM08] D. C. Pace, M. Shi, J. E. Maggs, G. J. Morales, and T. A. Carter. “Exponential frequency spectrum and Lorentzian pulses in magnetized plasmas.” *Phys. Plasmas*, **15**(12):122304, 2008.

[Rei02] Peter Reimann. “Brownian motors: noisy transport far from equilibrium.” *Physics Reports*, **361**(24):57 – 265, 2002.

[Ros07] Jan Rosiński. “Tempering stable processes.” *Stochastic Processes and their Applications*, **117**(6):677 – 707, 2007.

[SG03] G. Samorodnitsky and M. Grigoriu. “Tails of solutions of certain nonlinear stochastic differential equations driven by heavy tailed Lévy motions.” *Stochastic Processes and their Applications*, **105**(1):69 – 97, 2003.

[SKM93] S. G. Samko, A. A. Klibas, and O. I. Marichev. *Fractional integrals and derivatives.* Gordon and Breach, 1993.

[SM94] Jun Shen and Andreas Mandelis. “Thermal-wave resonator cavity.” *Rev. Sci. Instrum.*, **66**:4999–5005, 1994.

[SNL08] R. Sánchez, D. E. Newman, J.-N. Leboeuf, V. K. Decyk, and B. A. Carreras. “Nature of Transport across Sheared Zonal Flows in Electrostatic Ion-Temperature-Gradient Gyrokinetic Plasma Turbulence.” *Phys. Rev. Lett.*, **101**:205002, 2008.

[SZK93] M. F. Shlesinger, G. M. Zaslavsky, and J. Klafter. *Nature*, **363**:31–37, 1993.

[Tar89] L. Tartar. “Nonlocal effects induced by homogenization.” In F. Culumbini et al., editors, *PDE and calculus of variations.* Boston, Birkhauser, 1989.

[Ula57] S. Ulam. “Marian Smoluchowski and the Theory of Probabilities in Physics.” *American Journal of Physics*, **25**:475, 1957.

[VSB06] M. Vlad, F. Spineanu, and S. Benkadda. "Impurity Pinch from a Ratchet Process." *Phys. Rev. Lett.*, **96**:085001, Feb 2006.

[YCS00] V.V. Yanovsky, A.V. Chechkin, D. Schertzer, and A.V. Tur. "Lévy anomalous diffusion and fractional FokkerPlanck equation." *Physica A: Statistical Mechanics and its Applications*, **282**(12):13 – 34, 2000.

[Zas94] G. M. Zaslavsky. "Renormalization group theory of anomalous transport in systems with Hamiltonian chaos." *Chaos: An Interdisciplinary Journal of Nonlinear Science*, **4**:25, 1994.

[ZEN97] G. M. Zaslavsky, M. Edelman, and B. A. Niyazov. "Self-similarity, renormalization, and phase space nonuniformity of Hamiltonian chaotic dynamics." *Chaos: An Interdisciplinary Journal of Nonlinear Science*, **7**:159, 1997.

[ZSK99] Tatiana Zavada, Norbert Südland, Rainer Kimmich, and T. F. Nonnenmacher. "Propagator representation of anomalous diffusion: The orientational structure factor formalism in NMR." *Phys. Rev. E*, **60**:1292–1298, 1999.